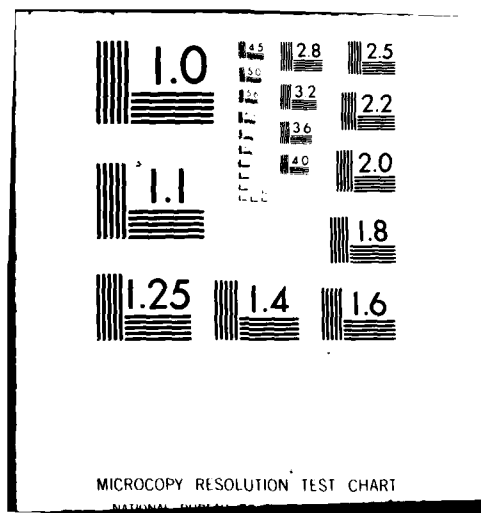


AD-A116 028 ARMY ELECTRONICS RESEARCH AND DEVELOPMENT COMMAND FO--ETC F/6 20/12
NUCLEAR TRACER MEASUREMENTS OF LOW TEMPERATURE WATER DIFFUSION --ETC(U)
JUN 82 R L PFEFFER

UNCLASSIFIED DELET-TR-82-4

NL

END
DATE FILMED
BY
DTIC





(12)

RESEARCH AND DEVELOPMENT TECHNICAL REPORT

DELET-TR-82-4

AD A116028

NUCLEAR TRACER MEASUREMENTS OF LOW TEMPERATURE
WATER DIFFUSION IN SILICON DIOXIDE (SiO_2) THIN
FILMS

ROBERT L. PFEFFER
ELECTRONICS TECHNOLOGY & DEVICES LABORATORY

JUNE 1982

DISTRIBUTION STATEMENT

Approved for public release;
distribution unlimited.

DTIC FILE COPY

ERADCOM

US ARMY ELECTRONICS RESEARCH & DEVELOPMENT COMMAND
FORT MONMOUTH, NEW JERSEY 07703

DTIC
REF ID: A62507
JUN 25 1982

D

A

82 06 25 022

NOTICES

Disclaimers

The citation of trade names and names of manufacturers in this report is not to be construed as official Government indorsement or approval of commercial products or services referenced herein.

Disposition

Destroy this report when it is no longer needed. Do not return it to the originator.

UNCLASSIFIED

SECURITY CLASSIFICATION OF THIS PAGE (When Data Entered)

REPORT DOCUMENTATION PAGE		READ INSTRUCTIONS BEFORE COMPLETING FORM
1. REPORT NUMBER DELET-TR-82-4	2. GOVT ACCESSION NO. AD-A476 028	3. RECIPIENT'S CATALOG NUMBER
4. TITLE (and Subtitle) NUCLEAR TRACER MEASUREMENTS OF LOW TEMPERATURE WATER DIFFUSION IN SILICON DIOXIDE (SiO ₂) THIN FILMS	5. TYPE OF REPORT & PERIOD COVERED	
7. AUTHOR(s) Robert L. Pfeffer	6. PERFORMING ORG. REPORT NUMBER	
9. PERFORMING ORGANIZATION NAME AND ADDRESS Electronic Materials Research Division US Army Electronics Technology & Devices Laboratory (ERADCOM), Fort Monmouth, NJ 07703 DELET-ER	10. PROGRAM ELEMENT, PROJECT, TASK AREA & WORK UNIT NUMBERS 61102A IL161102AH47 01 04	
11. CONTROLLING OFFICE NAME AND ADDRESS US Army Electronics Research & Development Command Fort Monmouth, NJ 07703 DELET-ER	12. REPORT DATE June 1982	
14. MONITORING AGENCY NAME & ADDRESS (if different from Controlling Office)	13. NUMBER OF PAGES 88	
	15. SECURITY CLASS. (of this report) Unclassified	
	15a. DECLASSIFICATION/DOWNGRADING SCHEDULE	
16. DISTRIBUTION STATEMENT (of this Report) Approved for public release; distribution unlimited.		
17. DISTRIBUTION STATEMENT (of the abstract entered in Block 20, if different from Report)		
18. SUPPLEMENTARY NOTES A condensed report of the research described herein has been published in J. Appl. Phys. 52 (2), 777 (Feb 81).		
19. KEY WORDS (Continue on reverse side if necessary and identify by block number) Oxidation Diffusion in Solids		
20. ABSTRACT (Continue on reverse side if necessary and identify by block number) As part of an investigation of the physical basis underlying aspects of MOS processing technology, we have studied the transport mechanism by which water diffuses through thin SiO ₂ films. This process is responsible for the formation of oxide layers on silicon wafers by means of thermal steam oxidation, which is frequently employed in the manufacture of integrated circuit devices. We have performed tracer diffusion measurements involving network 186, demonstrating the importance of oxygen exchange between the SiO ₂ network and molecularly dissolved (cont'd on reverse side)		

UNCLASSIFIED

SECURITY CLASSIFICATION OF THIS PAGE(When Data Entered)

10. Abstract (Cont'd)

water. We have found, that in the presence of water, bound network oxygen diffuses through SiO₂ as a constituent of molecularly dissolved water. Employing methods common to state-of-the-art semiconductor technology, the central region within a thermal oxide layer grown on silicon was enriched with immobile ¹⁸O by ion implantation. After heating in atmospheres with different water contents, the extent of ¹⁸O diffusion was determined by observing changes in the concentration profile (i.e. the chemical concentration as a function of depth) of implanted ¹⁸O by means of nuclear resonance profiling. In this technique, high-energy protons from a Van De Graaff accelerator lose energy in their passage through the oxide until their energy falls to a resonant energy of the ¹⁸O(p, α)¹⁵N reaction. High-energy alpha particles, emitted in this inelastic reaction from the ¹⁸O which is located at that depth, are detected after escaping from the surface. The observed thermal broadening of ion-implant distributions permitted bulk diffusivity to be measured conveniently at temperatures or gas-phase concentrations much lower than previously possible. Diffusions conducted in steam at 1 atm (at temperatures as low as 250C) showed an activation energy of about 17 kcal/mol, which is close to that originally measured for water permeation in SiO₂. Diffusions in both air and dry nitrogen showed a similar activation energy, with respective pre-exponential factors two and three orders of magnitude below the steam value. Diffusions in low pressure water vapor showed a clearly linear dependence on gas phase water concentration down to 80 ppm, in contrast to thermal oxidation results reported by others. The results of this study are consistent with a recently proposed model of water diffusion in SiO₂, in which the diffusion mechanism is the interstitial transport of dissolved molecular water accompanied by a reversible reaction with silicon-oxygen bonds in the network.



UNCLASSIFIED

CONTENTS

	<u>Page</u>
INTRODUCTION	1
Background	1
Molecular Structure of SiO₂	2
Ion Implantation and Its Effect on SiO₂	5
Transport of O₂ and H₂O in SiO₂	8
Nuclear Profiling Techniques	20
EXPERIMENTAL PROCEDURE	25
Materials Preparation	25
Thermal Treatments	25
Nuclear Resonance Profiling	31
RESULTS	40
DATA ANALYSIS	46
Method of Determining Tracer Diffusivity	46
Temperature and Pressure Dependence of Tracer Diffusivity	52
DISCUSSION	
Absence of Ion Bombardment Induced Damage in SiO₂ Network	57
¹⁸O Tracer Diffusion	58
Water Permeation Kinetics	60
CONCLUSIONS	65
ACKNOWLEDGMENTS	66
APPENDICES	
A. Evolution of ¹⁸O Distribution	67
B. Evolution of Alpha Particle Yield	70
C. Proton Energy Straggling Distribution	77
D. Nonequilibrium Permeation Kinetics	81
Bibliography	84
TABLES	
1. ACCELERATOR ENERGY CALIBRATION REACTIONS	37
2. SUMMARY OF THERMAL TREATMENTS AND RESULTS	41 & 42
3. COMPARISON OF METHODS FOR OBTAINING TRACER DIFFUSIVITY	56
FIGURES	
1. Schematic diagram of a two-dimensional structure of SiO ₂ .	4

1. (KEY TO FIGURE, p 12) Temperature Dependence of $D_{eff:H_2O}$ and D_{O_2} in SiO_2 : previous permeation results.	13
3. (KEY TO FIGURE, p 18) Previous measurements of parabolic rate constants for thermal oxidation of Si in O_2 and steam.	19
4. Principle of nuclear resonance profiling.	21
5. Analysis of residual gas in ion implantation apparatus	26
6. Apparatus for thermal treatments in steam.	29
7. Apparatus for thermal treatments at low pressure.	30
8. (KEY TO FIGURE, p 32) Van de Graaff accelerator: experimental area.	33
9. (KEY TO FIGURE, p 32) Van de Graaff accelerator: operating console.	34
10. Nuclear scattering chamber.	36
11. $^{27}Al(p,\gamma)^{28}Si$ gamma ray yield curve near 991 keV resonance for thick target.	39
12a, b, c. (KEY TO FIGURES, p 40)	
a. Observed alpha particle yield curves for selected samples.	43
b. Observed alpha particle yield curves for annealed samples.	44
c. Observed alpha particle yield curves for low D^*t samples.	45
13. Theoretical ^{18}O concentration profiles in SiO_2 layer after thermal treatments.	48
14. Theoretical alpha particle yield curves (labels indicate n).	49
15. Time behavior of theoretically derived peak alpha yield.	50
16. Observed temperature dependence of ^{18}O tracer diffusivity at 1 atm.	53 & 54
17. Pressure dependence of tracer diffusivity at 820 C. Labels indicate P in fractions of 1 atm.	55
18. Increment in the parabolic rate constant upon addition of H_2O to oxygen atmosphere, as percent of BH_2O in pure water vapor.	63

NUCLEAR TRACER MEASUREMENTS
OF LOW TEMPERATURE WATER DIFFUSION
IN SiO_2 THIN FILMS

INTRODUCTION

Background

The formation of thin insulating films on the surface of semiconductor materials is an important part of modern integrated circuit technology, which has assumed a central role in the production of Army control, communications, radar and data processing systems. The thin film can serve in integrated circuits as a dopant mask, surface protector, primary passivation coating, component isolator, and as gate insulator in MOS structures (1). Other applications of current interest include solar cells and power transistors. Because of their military and commercial importance, various means of film growth have been intensively studied, especially for high-quality gate insulators on silicon surfaces. For that application a more or less standard practice of thermal oxidation in dry oxygen or steam atmospheres has evolved. A properly made thermal oxide film must have a high dielectric strength and immunity to electrical breakdown, contain an acceptably low amount of trapped charge (particularly at the oxide-silicon interface), be uniform in thickness, bond intimately to the semiconductor substrate, and resist chemical or mechanical degradation. These requirements are well satisfied by present thermal oxidation methods. However, as integrated circuit devices become more complex and operate at higher speeds, they require smaller and more closely packed component structures. The scale of sizes being contemplated has now reached a point where basic changes will soon be required in manufacturing methods. For example, the need is foreseen to hold temperatures in all steps of a processing sequence low enough to prevent significant migration of dopants. This has spurred work on low-temperature, high-pressure thermal oxidation (2,3).

As might be expected, these low-temperature processing techniques may offer enough advantages over present high-temperature processing to supplant it in the manufacturing technology of future integrated circuit devices. These techniques may well produce devices having electrical characteristics, lifetimes and reliabilities surpassing any previously attainable. The ubiquity of SiO_2 films on semiconductor materials has been accompanied by a vast research effort - a recent bibliography (4) lists 560 references. Included are many studies of film formation, particularly thermal oxidation.

1. A. S. Grove, Physics and Technology of Semiconductor Devices (Wiley, 1967)
2. R. J. Zeto, C. G. Thornton, E. Hryckowian and C. D. Bosco, J Electrochem Soc 122, 1411 (1975)
3. L. E. Katz and B. F. Bowells, J Electrochem Soc 126, 1822 (1979)
4. H. Agopian, Sol St Tech 19, 36 (1977)

Virtually all of this work has been device-oriented. Physical models of the oxidation process have received little attention; only now are models being tested with sufficient care to generate a consensus of acceptance. Throughout the device-oriented literature, one encounters a virtually unanimous lack of appreciation of both the nature and the consequences of the water-SiO₂ reaction. The lack of reproducibility in thermal growth kinetics data caused by the presence of water, even in trace amounts, has lately been corrected through careful control of conditions (5). For the future, a greater understanding of the mechanism responsible for oxidation in the presence of water is imperative, especially in the new low-temperature regime, where it now appears that processing of the coming generation of devices will take place.

The purpose of this investigation was threefold:

To clarify the mechanism of SiO₂ film growth in atmospheres containing water, this work provides the first direct experimental demonstration of the validity of a recently proposed model of the oxidation process. According to this model, growth proceeds by inward interstitial diffusion of adsorbed molecular water, which simultaneously reacts with the SiO₂ network to form immobile reaction products.

To apply the technique of ion implantation to measure tracer oxygen diffusion in SiO₂. The observation of tracer distribution broadening both eliminates surface effects and enhances the sensitivity of diffusion measurements so that tracer diffusion measurements can be carried out at considerably reduced temperatures.

To provide a framework for resolving several long-standing discrepancies between measurements involving water and oxygen diffusion in SiO₂. These are wide differences in oxygen diffusivities observed in permeation experiments, as well as in measurements involving the pressure dependence of the growth kinetics of thermal silicon oxidation. This work demonstrates that these can be resolved through a proper understanding of water diffusion in the oxides.

Molecular Structure of SiO₂

The basic building block of vitreous silica, the amorphous form of SiO₂, is a tetrahedron of oxygen ions around a central silicon ion. According to the generally accepted model originated by Zachariasen (6), each tetrahedron is joined to four others by silicon-oxygen bonds at its corners in a continuous three-dimensional random network lacking any symmetry or periodicity.

5. S. Mayo and W.H. Evans, "Development of Hydrogen and Hydroxyl Contamination in Thin Silicon Dioxide Films" NBSIR 78-1558 (NBS, March 1979)
6. W. H. Zachariasen, J Am Chem Soc 54 3841 (1932)

as illustrated in Figure 1. The Si-O interatomic distance is 1.62 Å; the O-O distance is 2.65 Å. The distribution of Si-O-Si bond angles ranges from 120° to 180°; it is skewed toward the smaller angles and has a single maximum located at 144° (7). It is narrow compared to a fully random distribution, so that the structure is quite uniform over several tetrahedra (although not beyond that). There is a good deal of experimental evidence supporting this model which is quoted by Doremus, pp. 24-28 (8), including X-ray diffraction studies in terms of pair distribution functions, transmission electron microscopy and atomic vibrational spectroscopy via infrared absorption, Raman emission and inelastic neutron scattering. Beside this work are studies involving X-ray diffraction (9, 10), inelastic neutron scattering (11), and electron diffraction and infrared absorption (12).

Several recent experiments (13, 14, 15) support closely related but competing models based on a collection of distorted microcrystallites such as crystobalite, each containing only a few tetrahedra. All viable models, however, share the essential picture of vitreous silica as a loosely packed material in which cavities or interstices are surrounded by walls of more or less intact SiO_4 tetrahedra. Shackelford and Masaryk (15) give the mean diameter of the interstices as 1.96 Å.

There is much evidence that dry thermal oxide layers formed on silicon surfaces have the same structure as vitreous silica. X-ray diffraction experiments showed the oxide layers to be amorphous (16). The density of the layers is close to that of fused silica (17), as are the changes in density induced by ionizing radiation (18). The optical properties are essentially identical (19), as are the Si-O-Si bond angles obtained from electron diffraction and IR absorption experiments (12).

7. R. L. Mozzi and B. E. Warren, *J Appl Cryst* 2, 164 (1969)
8. R. H. Doremus, *Glass Science* (Wiley, 1973)
9. J. H. Konnert and J. Karle, *Acta Cryst A* 29, 702 (1973)
10. A. H. Narten, *J Chem Phys* 56, 1905 (1972)
11. A. L. Leadbetter and M. W. Stringfellow, "Neutron Inelastic Scattering," *Proc Grenoble Conf* (IAEA, Vienna, 1972) p. 501
12. N. Nagasima, *Japan J Appl Phys* 9, 879 (1970)
13. G. Brauer, G. Boden, A. Balogh and A. Andreeff, *Appl Phys* 16, 231 (1978)
14. P. H. Gaskell, D. W. Johnson, *J Noncryst Sol* 20, 171 (1976)
15. J. F. Shackelford and J. S. Masaryk, *J Noncryst Sol* 30, 127 (1978)
16. M. B. Brodsky, D. Cubicciotti, *J Am Chem Soc* 73, 3497 (1951)
17. R. H. Doremus, *J Phys Chem* 80, 1773 (1976)
18. E. P. Eernisse, *J Appl Phys* 45, 167 (1974)
19. A. N. Knopp and R. Stickler, *Electrochem Technology* 5, 37 (1967)

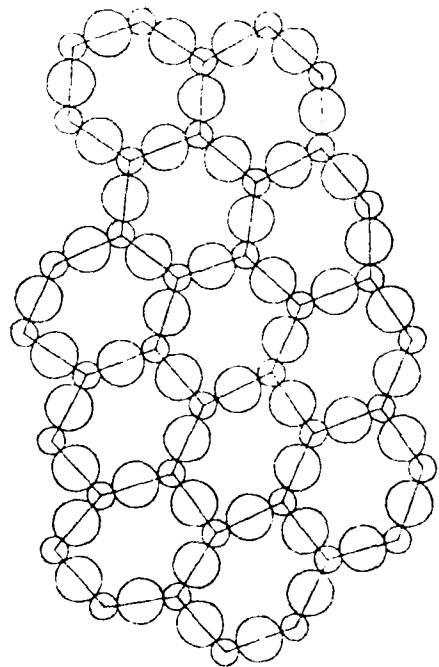


Figure 1. Schematic diagram of a two-dimensional structure of SiO_2 (from Doremus (8)). The oxygen atoms (larger circles) act as bridges between tetrahedra. Note the large size of the interstices.

8. R. H. Doremus, Glass Science, p 27 (Wiley, 1973)

Ion Implantation and its Effects on SiO₂

The implantation of heavy ions in the tens to hundreds of keV range is by now a routine aspect of semiconductor processing (20). The implantation of dopant elements directly into desired regions in the interior of semiconductor materials has eliminated the need for high-temperature diffusions to induce their migration from the surface, allowing much greater control over material properties. In regular lattice structures, the ions produce heavy damage, and a significant fraction of them remain interstitial. When appropriate annealing procedures are employed, the damage is healed virtually completely and the dopant ions assume desired substitutional sites (21).

There have been many studies of ionizing radiation effects on SiO₂ as well. One motivation for these is nuclear vulnerability assessment for military applications; another comes from the frequent practice of implantation into silicon through previously grown SiO₂ layers. Many different effects have been observed, including radiation compaction (22, 23, 24, 25, 18), enhancement of HF etch rate (26, 27), accumulation of thermal energy (28), changes in Raman and IR spectra (29, 30), change in refractive index

20. J. W. Mayer, L. Eriksson and J. A. Davies, Ion Implantation in Semiconductors (Academic, 1970)
21. J. R. Gibbons, Proc IEEE 60, 1062 (1972)
22. W. Primak, J Appl Phys 43, 2745 (1972)
23. J. E. Shelby, J Appl Phys 50, 3702 (1979)
24. C. B. Norris and E. P. Eernisse, J Appl Phys 45, 3876 (1974)
25. E. P. Eernisse and C. B. Norris, J Appl Phys 45, 5196 (1974)
26. W. Kratschmer, "Effects of Heavy Ion Radiation on Quartz Glass," Proc. Int. Conf. on Nucl. Photography and Track Detectors (Bucharest 1972) quoted in Antonini (1978)
27. A. Monfret and J. Bernard, "Chemical and Electrical Behavior of Ion Implanted SiO₂ Films" in Proc. 2nd Int. Conf. Ion Implantation in Semiconductors, I. Ruge and J. Graul, eds. (Springer-Verlag, 1971).
28. V. Antonini, A. Manara and P. Lensi, "Ion Irradiation and Stored Energy in Vitreous Silica, in Pantelides (1978), p. 316
29. J. R. Bates, R. W. Hendricks and L. B. Shaffer, J Chem Phys 61, 4163 (1974)
30. C. R. Fritzene and W. Rothermund, J Electrochem Soc 119, 1243 (1972)

(ibid), thermoluminescence (31), and generation of deep electron traps (32, 33, 34) and color centers (35, 36, 37).

The mechanisms responsible for these effects fall into three rough categories, which are separable to some extent by choice of appropriate projectile and by studying the annealing behavior of the defects created. The first is bond breaking resulting from ionization reactions, exemplified by dangling bonds and oxygen vacancies. These are produced by X- and gamma radiation and electrons, and are largely annealed out by heating to 400 C; some remain until 700 C (25). The second is formation of new bonds between implanted heavy ions and the network. These do not anneal out but remain as features of an altered network (34). The third, structural alterations caused by atomic displacement, is associated with heavy ion bombardment. These may be produced by direct nuclear knock-on reactions causing displacement of recoils, as well as through absorption of sufficient vibrational energy to reconfigure strained bond structures. Their importance increases with increasing ion mass and decreasing velocity, being especially significant near the end of the ion paths; most displacement damage is confined to that region (38, 39). An additional effect peculiar to the presence of hydrogen has recently been identified by Shelby (23) as dilatation or swelling of the network, possibly caused by a radiation-induced increase in the number of binding sites for SiOH and SiH. Irene and Ghez (40) have speculated that this dilatation may contribute to the pronounced effect of small amounts of water in the network.

As in the case of silicon, inert-atmosphere heating has been observed to anneal out the various radiation-induced alterations to the SiO_2 network.

32. J. E. Shelby, J Appl Phys 50, 3702 (1979)
33. E. P. Eernisse and C. B. Norris, J Appl Phys 45, 5196 (1974)
34. G. W. Arnold, "Thermoluminescence in Ion-Implanted SiO_2 ," in Chernow et al (1977)
35. R. P. Denovan and M. Simons, J Appl Phys 43, 2897 (1972)
36. N. M. Johnson, W. C. Johnson and M. A. Lampert, J Appl Phys 46, 1216 (1975)
37. D. J. DiMaria, D. R. Young, W. R. Hunter and C. M. Serrano, IBM J Res Develop., 22, 289 (1978)
38. J. W. Arnold, IEEE Trans Nucl Sci NS-20, 220 (1973)
J. W. Arnold, "Vibrational and Electronic Spectroscopy of Ion-Implantation-Induced Defects in Fused Silica and Crystalline Quartz," in Ion-Implanted Dielectrics, p. 178 (1978)
39. G. H. Sigel, Jr., B. D. Evans, R. J. Ginther, E. J. Friebele, D. L. Griscom and J. Babiskin, NRL Memo Rpt No. 2934 (NRL, 1974)
40. D. K. Brice, Radiation Eff (GB) 6, 77 (1970)
41. K. B. Winterbon, Ion Implantation Range and Energy Depositions, Vol 2 (Plenum, 1975)
42. E. A. Irene and R. Ghez, J Electrochem Soc 124, 1757 (1977)

Antonini et al (28) observed that the thermal energy accumulated during bombardment with 1 MeV alpha particles was released upon heating to about 470 C, while that accumulated during bombardment with 46.5 MeV Ni⁺₆ ions was released in two stages: partly at 450 C and the rest at about 610 C. Monfret and Bernard (27) reported that radiation enhancement of the HF etch rate largely disappeared after a 20 min anneal at 600 C (totally after 1000 C). Wang et al (41) reported the changes (induced by 50 keV Al ion implantation) in UV absorption in the 7.5 eV band to be 75% gone with a 500 C anneal (totally after 900 C), and that the amplitude of a similarly induced ESR resonance (with g = 2.0037) decreased with increasing temperature, disappearing by 500 C. Eernisse and Norris (25) in their thorough study of compaction annealing, reported a relatively sharp return to initial density as temperatures increased beyond 650 C after bombardment by either 7.27 keV electrons or 250 keV protons, and a gradual return between 300 C and 900 C after 500 keV Ar⁺⁺ bombardment. In sum, and as indicated by Sigel (42), all studies of radiation damage in SiO₂ indicate that a 900 C anneal is sufficient to completely restore the network to its pre-irradiation state.

The behavior of the implanted ions at the end of their range in the network can be inferred using a model of ion-network interactions propounded by Primak 1972 (22) and Primak 1975, p. 111-119 (43). This is a refinement of the thermal spike model originally proposed by Seitz (44), in which heavy ions transfer energy to the network via atomic collisions, causing a large amount of vibrational excitation. Subsequent rapid refreezing leads to reformation of bonds with the implanted ions in substitutional sites. Evidence from this comes from SIMS measurements by H. Hughes (quoted in Johnson et al (33)), who found that 30-min. anneals in N₂ at 900 C failed to alter the concentration profiles of Al implanted in SiO₂; a similar result was obtained by DiMaria et al (34) at 1050 C.

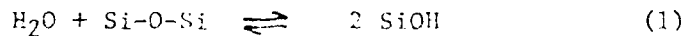
- 22. W. Primak, J Appl Phys 43, 2745 (1972)
- 23. E. P. Eernisse and C. B. Norris, J Appl Phys 45, 5196 (1974)
- 27. A. Monfret and J. Bernard, "Chemical and Electrical Behavior of Ion Implanted SiO₂ Films" in Proc. 2nd Int. Conf. Ion Implantation in Semiconductors, I. Ruge and J. Graul, eds. (Springer-Verlag, 1971)
- 28. V. Antonini, A. Manara and P. Lensi, "Ion Irradiation and Stored Energy in Vitreous Silica," in Pantelides, p 316 (1978)
- 33. N. M. Johnson, W. C. Johnson and M. A. Lampert, J Appl Phys 46, 1216 (1975)
- 34. D. J. DiMaria, D. R. Young, W. R. Hunter and C. M. Serrano, IBM J Res Devel, 22, 289 (1978)
- 41. S. Wang, T. Russell and B. S. H. Royce "Annealing Studies of Al+ Implanted SiO₂ Thin Films," PSSL 300874 (Princeton U., 1974)
- 42. G. H. Sigel, private communication (1979)
- 43. W. Primak, Compacted States of Vitreous Silica (Gordon and Breach, 1975)
- 44. F. Seitz, Disc Faraday Soc. 5, 271 (1949)

Transport of O₂ and H₂O in SiO₂

Definitions of Solubility

The solubility generally found in the literature is the saturation concentration of gas dissolved in the solid $\rho_{\text{dissolved(sat)}}$ (in units of molecules/cm³) at standard temperature and pressure. A related quantity, the solubility ratio, also frequently appears in the literature. This quantity is defined as the steady state ratio $\rho_{\text{dissolved(sat)}}/\rho_{\text{gas phase}}$ at a given temperature and pressure. This is a dimensionless quantity. It is independent of ambient gas-phase pressure provided the same substance is being observed both outside and inside the oxide (i.e., in the absence of dissociation). Its temperature dependence - generally very weak - arises from a possible temperature dependence in the activation energy of molecular motion (45).

As will be discussed shortly, the dissolution of water in SiO₂ involves a reaction with the network, in which the molecularly dissolved water dissociates to form two OH units with the additional O ion being provided by the network (46, 45). This reversible reaction



leads to equilibrium concentrations of reaction products which are large relative to that of molecularly dissolved water. The equilibrium concentrations are related by the law of detailed balance

$$K^2 = \frac{\rho_{\text{OH}}^2}{\rho_{\text{H}_2\text{O}}} \cdot \quad (2)$$

The value of K² (including any temperature dependence) is gotten from the probabilities of molecular and "reacted" water (i.e. SiOH groups). It must be remembered that the dissociation of H₂O leads to a reacted water molecule which is dependent on the concentration of vapor phase water.

45. J. F. Shackelford and J. S. Masaryk, *J Noncryst Sol* **21**, 55 (1976)
46. R. H. Doremus, in Reactivity of Solids, Mitchell, de Vries, Roberts and Cannon, Eds., (Wiley, 1969) p. 667

Definitions of Diffusivity

There are three different diffusion coefficients which are involved in the transport of tracer ^{18}O . The first of these, D_{eff} , is that quantity normally measured in permeation experiments. The basic method of determining this effective diffusivity is by observing the steady-state flux J of gas passing through a membrane of thickness X_0 whose two surfaces are maintained at different pressures. From the basic equation $J = -D_{\text{eff}} \frac{\Delta P}{X_0}$ we have

$$D_{\text{eff}} = - \frac{X_0}{\Delta P_{\text{dissolved}}} J_{\text{steady-state}} \quad (3)$$

where $\Delta P_{\text{dissolved}}$, the difference in concentrations at the two surfaces, is known through independent measurement of the solubility. The temperature dependence of D_{eff} is generally expressed via the Arrhenius equation

$$D_{\text{eff}} = D_0 \exp\left(-\frac{Q}{RT}\right) = D_0 \exp\left(-\frac{E_a}{kT}\right) \quad (4)$$

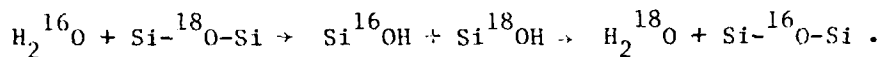
where R and k are the universal gas constant (in units of kcal/mol/K and eV/Å respectively) and Q and E_a are the activation energy of diffusion (in units of kcal/mol and eV respectively). D_{eff} can also be measured dynamically by observing the evolution of ambient gas pressures in the early stages of either permeation or desorption in membranes, filaments or powders in an enclosed volume (see, for example, Doremus, pp. 128-130 (8)). It should be noted that D_{eff} will be independent of ambient gas-phase concentration only if the fluxes of both the emerging particles and the dissolved species have the same pressure dependence. Such is not the case for water diffusion, where D_{eff} is the apparent diffusivity of reacted water.

The transport of the actual mobile species is described by the microscopic diffusivity D . It is influenced only by the interactions of individual diffusing molecules with the network. For a dilute gas (i.e. one without significant interaction between diffusing molecules) in a spatially uniform network, D is independent of ambient gas phase concentration, spatial location and dissolved gas concentration - it depends only on temperature. For oxygen diffusion in SiO_2 , which proceeds without any appreciable dissociation or reaction with the network, D_{eff} and D have the same value. However, for water diffusion, they are related by the equation

$$D_{\text{eff}} = D \frac{2\rho_{\text{H}_2\text{O}}}{2\rho_{\text{H}_2\text{O}} + \rho_{\text{OH}}} \cdot \quad (5)$$

The fraction represents the fraction of time that any particular OH group finds itself moving as part of a diffusing water molecule. The factor of 2 appears because each water molecule removes two OH groups from the network.

The third diffusion coefficient, D^* , describes the apparent diffusion of tracer ^{18}O . As will be discussed shortly, the mechanism responsible for the migration of network ^{18}O observed in this study is the exchange between diffusing water and network oxygen. The reaction between dissolved molecular water and the SiO_2 network described by equation (1) acts to remove ^{18}O from its network site and to convert it instead to a constituent of diffusing molecular water:



In the presence of free exchange, the tracer diffusivity D^* is related to the diffusivity of molecularly dissolved water by the equation

$$D^* = D \frac{\rho_{\text{H}_2\text{O}}}{2\rho_{\text{SiO}_2} + \rho_{\text{H}_2\text{O}} + \rho_{\text{OH}}} . \quad (6)$$

... fraction is the fraction of time that an ^{18}O finds itself being carried by a diffusing water molecule. The factor of 2 accounts for the two oxygen atoms per SiO_2 molecule.

Mechanisms of O_2 and H_2O Diffusion

Based on the observations to be discussed shortly, the mechanism of either oxygen or water diffusion has been taken to be the interstitial transport of dissolved molecular oxygen or water respectively. In neither case does the diffusion process involve direct bonding between the diffusing species and the SiO_2 network. Rather it involves the transport of nonreacting molecules through the interstices or cavities in the network. This interstitial model was first proposed by Anderson and Stuart (47); they calculated activation energy for diffusion as the elastic energy required to deform the network by enlarging the circular doorways between interstices enough for the diffusing species to pass. An essential feature of this model is a lack of chemical binding between the diffusing species and the network (Milberg, 48). Although the model is simplistic, the functional dependence of activation energy upon molecular diameter agrees well with activation energies measured for molecular diffusion of various gases in fused silica (Doremus, 49). It is also consistent with the linear dependence of diffusivity upon pressure observed by Norton (49) for oxygen, whose diffusion is accompanied by any significant reactions with the SiO_2 network.

- 47. W. Doremus, Glass Science (Wiley, 1973)
- 48. O. L. Anderson and D. A. Stuart, J Am Ceram Soc 37, 573 (1964)
- 48. M. E. Milberg, "Diffusion in Glass," in Fast Ion Transport in Solids, W. Van Gool ed. (North Holland 1973) p. 378
- 49. F. J. Norton, Nature 191, 701 (1961)

This was demonstrated recently in a tracer experiment conducted by Rosencher et al (50) in which thermal oxide films which were first grown in natural oxygen were further grown in ^{18}O -enriched gas. Almost all additional ^{18}O was observed to collect in a layer at the Si-SiO₂ interface, while less than 0.3% remained in the previously grown region. Great care was taken to eliminate any water in this experiment.

The mechanism for water diffusion through SiO₂ is similarly thought to involve the interstitial transport of dissolved molecular water (Doremus (46)). The transport of the diffusing species, dissolved molecular water, is again postulated to involve no direct reaction with the network. However, as indicated in equation (1), a strong reaction occurs with silicon-oxygen bonds in the network, accounting for its high solubility as well as the square root dependence of the reacted water concentration on ambient water vapor pressure. The reaction products (i.e. SiOH groups) are postulated to be immobile, while the molecularly dissolved water diffuses with a diffusivity D, as discussed above.

O₂ Solubility, Diffusivity: Previous Permeation Measurements

Previous experimental values for oxygen diffusivity in SiO₂ were determined using variants of the basic technique mentioned above. By mass spectrometry, Norton (49) measured the evolution of $(^{16}\text{O})_2$ gas inside evacuated silica bulbs which were subjected for a time to a known oxygen pressure outside. Haul and Dumbgen (51) and Sucov (52) introduced measured quantities of ^{18}O gas into chambers containing silica fibers, then observed the decrease in $^{18}\text{O}:\text{^{16}O}$ mole fractions with a mass spectrometer; Williams (53) did the same for both bulbs and fibers. Their results (as they appear in the works cited) have here been compiled as an Arrhenius plot in Figure 2, and are considered at length in the Discussion; it may be remarked here that the three sets of very low oxygen diffusivities were all measured by means of tracer ^{18}O (to be discussed later) while the other was measured with natural O₂. Norton (49) also determined the O₂ solubility ratio to be $1.9(10)^{-3}$ (at 1078 C) and $2.3(10)^{-3}$ (at 950 C) and observed that the rate of permeation was proportional to the first power of the ambient oxygen pressure. None of the other works presents an explicit value of the O₂ solubility ratio.

46. R. H. Doremus, in Reactivity of Solids, Mitchell, de Vries, Roberts and Cannon, Eds. (Wiley, 1969) p. 667
49. F. J. Norton, Nature 191, 701 (1961)
50. E. Rosencher, A. Straboni, S. Rigo and G. Amsel, Appl Phys Lett 34, 254 (1979)
51. R. Haul and G. Dumbgen, Z Electrochem 66, 636 (1962)
52. E. W. Sucov, J Am Ceram Soc 46, 14 (1963)
53. E. L. Williams, J Am Ceram Soc 48, 190 (1965)

Figure 2. (Following Page) Temperature dependence of $D_{eff:H_2O}$ and D_{O_2} in SiO_2 : previous permeation results.

KEY TO FIGURE

SYMBOL	SOURCE	D_0 (cm^2/s)	Q (kcal/mol)
●	Norton (49)	$2.9(10)^{-4}$	27.0
— —	Haul and Dumbgen (51) as quoted in Terai and Hayami (92)	$1.2(10)^{-5}$	56.0
□	Sucov (52)	$1.5(10)^{-2}$	71.2
○ △	Williams (53)	$2.0(10)^{-9}$	29.0
×	Moulson and Roberts (54)	$1.0(10)^{-6}$	18.3

- 49. J. Norton, Nature 191, 701 (1961)
- 50. H. Haul and G. Dumbgen, Z. Electrochem 66, 636 (1962)
- 51. J. W. Sucov, J Am Ceram Soc 46, 14 (1963)
- 53. E. L. Williams, J Am Ceram Soc 48, 190 (1965)
- 54. J. Moulson and J. P. Roberts, Trans Faraday Soc 57, 1208 (1961)
- 92. R. C. Weast, Handbook of Chemistry and Physics, 55th ed (CRC Press, 1974)

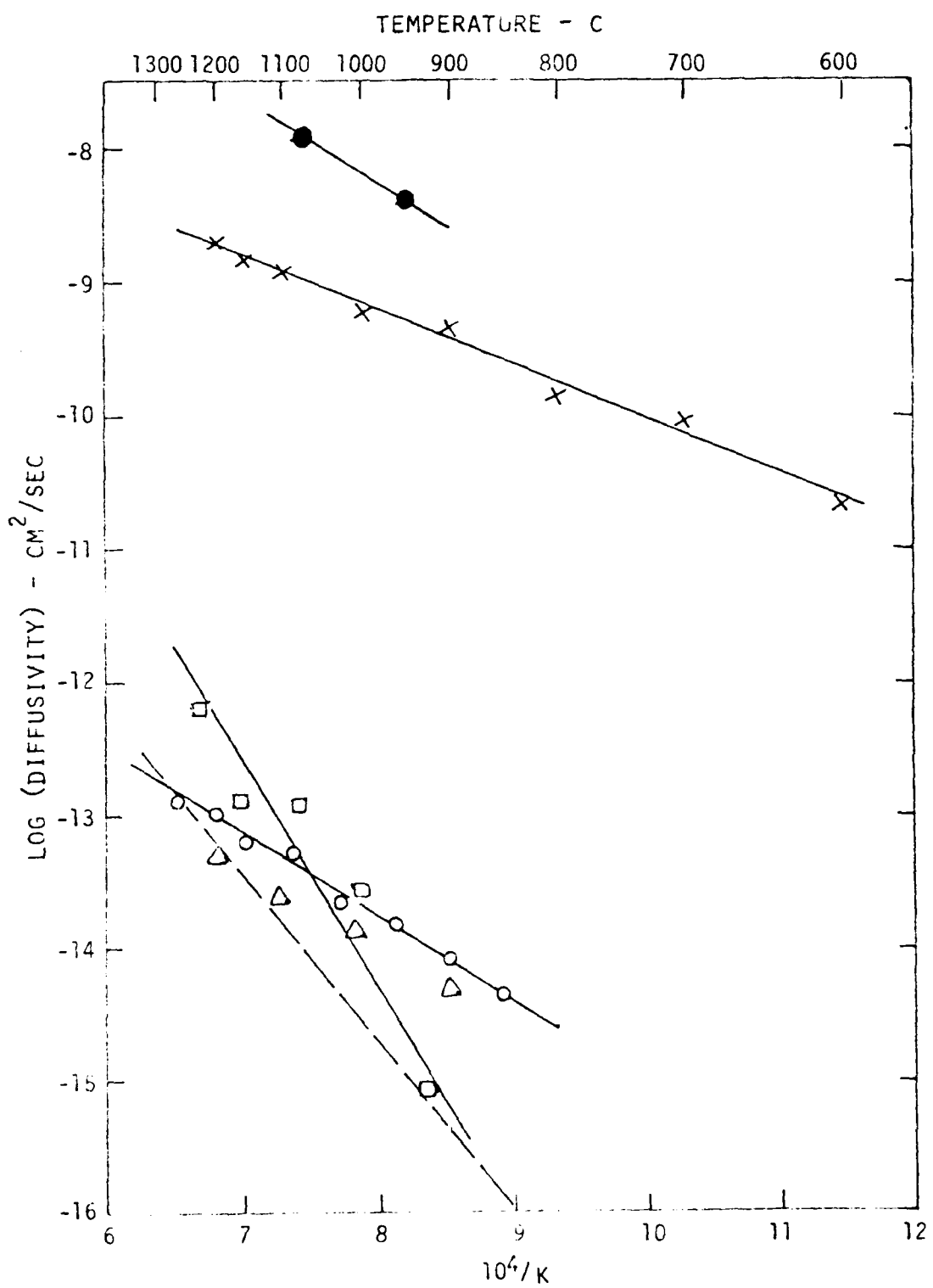


Figure 2. Temperature dependence of $D_{\text{eff}} : \text{H}_2\text{O}$ and D_{O_2} in SiO_2 : previous permeation results.

H_2O Solubility, Diffusivity: Previous Permeation Measurements

In the case of water, Moulson and Roberts (54) measured the effective bulk diffusivity in vitreous silica slabs by observing permeation-induced changes in optical density of the OH infrared absorption peak at 2.7 μm . By this technique they also determined the number of hydroxyl groups per SiO_2 molecule to range from 6×10^{-3} (@600 C) to 3×10^{-3} (@1200 C) at 1 atmosphere and observed it to vary as the square root of the ambient water vapor pressure. Their solubility results were confirmed by Shackelford et al (55) using a similar technique. Shackelford and Masaryk (45) later analyzed this using a slightly temperature-dependent activation energy for OH-group diffusion. The observed pressure dependence of $\rho_{OH(Sat)}$, as well as its large variation, is caused by the strong reaction of water with SiO_2 , as noted.

The concentration of dissolved molecular water is inaccessible to direct measurement since it is so much smaller than $\rho_{OH(Sat)}$; rather it must be inferred from consideration of known solubility ratios of nonreactive gases relative to its molecular size. Doremus (17), taking the molecular diameter of water to be 3.3 \AA (Doremus, P. 133 (8), concluded that the solubility ratio of molecular water is 0.01. Using Grove's

$$\rho_{SiO_2} = 2.25(10)^{22} \text{ cm}^{-3} \quad (7)$$

Note that the results of Moulson and Roberts (54), and Doremus (17)

$$\frac{\rho_{H_2O(Sat)}}{\rho_{OH(Sat)}} = \sqrt{P(atm)} \times \begin{cases} \frac{1}{894} & (@ 600 C) \\ \frac{1}{581} & (@ 1200 C) \end{cases} \quad (8)$$

8. L. R. Doremus, Glass Science (Wiley, 1973)
17. L. R. Doremus, J Phys Chem 80, 1773 (1976)
45. J. F. Shackelford and J. S. Masaryk, J Noncryst Sol 21, 55 (1976)
54. J. Moulson and J. P. Roberts, Trans Faraday Soc 57, 1208 (1961)
55. J. F. Shackelford, R. L. Stude and R. M. Fulrath, J Appl Phys 43, 1619 (1972)

The values of D_{eff} which were measured for H_2O diffusion in SiO_2 by Moulson and Roberts (54) appear in Figure 2. If these are taken in conjunction with their measured values for $\rho_{OH}(Sat)$, values for the diffusivity of molecular water can be calculated by use of equations (5) and (8), namely

$$D = \begin{cases} 8.9(10)^{-9} & (@ 600 C) \\ 5.2(10)^{-7} & (@ 1200 C) \end{cases} \text{ cm}^2/\text{s}. \quad (9)$$

Finally, the tracer diffusivity may be calculated on the basis of free exchange. Using equation (6) and the inequalities $\rho_{SiO_2} \gg \rho_{OH} \gg \rho_{H_2O}$ we find that D^* is related to D_{eff} by

$$\left\{ \frac{D^*}{D_{eff}} \right\}_{\text{free exchange}} \approx \frac{\rho_{OH}(\text{Sat})}{4\rho_{SiO_2}} = \begin{cases} 15(10)^{-4} & @ 600 C \\ 7.5(10)^{-4} & @ 1200 C \end{cases} \quad (10)$$

The value of ρ_{OH}/ρ_{SiO_2} has been taken from the solubility measurements of Moulson and Roberts.

O_2 and H_2O Diffusion through SiO_2 Films: Thermal Oxidation Kinetics

The diffusion of O_2 and H_2O through SiO_2 is intimately involved in the thermal oxidation of silicon. When silicon is maintained at an elevated temperature in an oxidizing atmosphere such as oxygen or steam, a layer of SiO_x is formed on the surface, which grows continually in the presence of the oxidant. Various tracer experiments cited in Deal and Grove (56) have established that oxidation proceeds by the inward transport of oxygen through the layer as a constituent of molecularly dissolved oxygen or water. The silicon substrate is converted to new oxide by the incorporation of atomic oxygen at the oxide-silicon interface after molecular dissociation. The layer thickens by formation of new oxide underneath the existing layer.

As discussed previously, the dissociation products also react strongly with the SiO_2 network only in the case of H_2O oxidation (46); for oxygen, the atomic oxygen reacts significantly only with the silicon at the interface (50). In that case, as was pointed out by Blanc (57), an equilibrium exists at the interface; atomic oxygen can either form new SiO_2 or recombine into molecular oxygen. Blanc was able to deduce equilibrium constants for these reactions so as to produce a very impressive match to a large body of data on thermal growth kinetics, and disprove the existence of a hypothetical space-charge layer which Deal and Grove (56) introduced to reconcile the data to their linear-parabolic model (discussed later).

- 46. R. H. Doremus, in Reactivity of Solids, Mitchell, de Vries, Roberts and Cannon, Eds. (Wiley, 1969) p. 667
- 50. E. Rosenthaler, A. Straboni, S. Rigo and G. Amsel, Appl Phys Lett 34, 254 (1979)
- 54. J. Moulson and J. P. Roberts, Trans Faraday Soc 57, 1208 (1961)
- 56. B. E. Deal and A. S. Grove, J Appl Phys 36, 3770 (1965)
- 57. J. Blanc, Appl Phys Lett 33, 424 (1978)

It may be mentioned that other competing models for the thermal oxidation process also exist, including transport of charged interstitial oxygen and holes (58), transport of O^- , $O^=$ and $O_2^=$ ions through a nonstoichiometric interphase region beneath the oxide layer (59), and transport of excess oxygen and silicon centers (60). None of these provides an acceptable fit to the experimental data. A model of interfacial dissociation/recombination similar to Blanc's was proposed by Ghez and Van der Meulen (61); this involved the incorporation of both atomic and molecular oxygen.

The growth kinetics of thermal oxide films provide an independent method of measuring oxygen and water diffusion in SiO_2 . By equating the steady-state fluxes of oxidant entering the oxide layer, diffusing through it, and forming new oxide at the interface, Deal and Grove (56) were able to show that the thickness of the growing oxide layer obeys a linear-parabolic equation of the form

$$x_o^2 + Ax_o = B(t + \tau) \quad (11)$$

where x_o is the thickness of the layer at time t . Their equation (12b) relating the parabolic rate constant B with the effective diffusivity of the oxidizing species appears in our notation as

$$B_{H_2O} = D_{eff} \rho_{OH}^{(Sat)} / \rho_{SiO_2} \quad (12)$$

$$B_{O_2} = 2D_{O_2} \rho_{O_2}^{(Sat)} / \rho_{SiO_2}. \quad (13)$$

Deal and Grove measured the parabolic rate constant B to have activation energies of 28.3 and 16.3 kcal/mol for O_2 and H_2O oxidation; by combining their measurements of B with the values for D_{eff} found by Norton and Moulson (49) and Roberts (54) respectively, they found that $\rho_{OH}^{(Sat)}$ and $\rho_{O_2}^{(Sat)}$ agreed with the permeation values to within about 10%. They found B to be linearly proportional to ambient gas pressure in both cases. This is to be expected from the observed square-root dependence of both D_{eff} and $\rho_{OH}^{(Sat)}$ on pressure for water and their linear dependence for oxygen, as was pointed out by Doremus (17).

17. R. H. Doremus, J Phys Chem 80, 1773 (1976)
18. W. J. Norton, Nature 191, 701 (1961)
54. J. Moulson and J. P. Roberts, Trans Faraday Soc 57, 1208 (1961)
56. R. E. Deal and A. S. Grove, J Appl Phys 36, 3770 (1965)
58. E. M. Fowkes and F. H. Hielscher, Electrochem Soc Abstract #182, Spring Meeting, Seattle (21 May 1978)
59. A. Lora-Tamayo, E. Dominguez, E. Lora-Tamayo and J. Llabres, Appl Phys 17, 79 (1978)
60. R. J. Maier, "A Study of SiO_2 Growth Mechanism," AFWL-TR-76-228 (US Air Force, Kirtland AFB, NM, 1977)
61. R. Ghez and Y. J. Van der Meulen, J Electrochem Soc 119, 1100 (1972)

Since the work of Deal and Grove, a large number of other experiments on the growth kinetics of thermal oxides have been conducted. Among these are measurements in oxygen at 1 atm (62, 63, 64, 65, 40, 66, 67, 68) and steam (69, 70); the activation energies reported by all these investigators are in good agreement with Deal and Grove. Some of this data is displayed in Figure 3, where it may be compared to the permeation measurements shown in Figure 2.

In addition to these, a number of studies have been made of the dependence of B on the partial pressure of ambient water. Ota and Butler (71) found a linear dependence at 1230 C for H₂O partial pressures between 0.1 and 1 atm, using water vapor either alone or in mixtures with H₂ and Ar. Deal and Grove also found this dependence between 0.02 and 0.2 atm at 1100 C with O₂, and Ehara et al (68) between 0.02 and 1 atm at 1100 C with O₂. Katz and Howells (3) found B to be twice that expected at 20 atm at 725 C using pure H₂O. Irene, however, (64, 40) has found that B increases sharply with the first traces of H₂O in O₂ up to 125 ppm followed by a smaller rate of increase for H₂O concentrations from 0.001 to 0.02 atm. The measurements performed in this study contradict those of Irene - they imply a purely linear pressure dependence down to 80 ppm. A likely explanation for the discrepancy and suggestions for its resolution are put forth at length in the Discussion section.

3. L. E. Katz and B. F. Howells, J Electrochem Soc 126, 1822 (1979)
40. E. A. Irene and R. Ghez, J Electrochem Soc 124, 1757 (1977)
62. A. G. Revesz and R. J. Evans, J Phys Chem Solids, 30, 551 (1969)
63. M. A. Hopper, R. A. Clarke and L. Young, J Electrochem Soc 122, 1216 (1975)
64. E. A. Irene, J Electrochem Soc 121, 1613 (1974)
65. E. A. Irene and Y. J. Van der Meulen, J Electrochem Soc 123, 1384 (1976)
66. B. E. Deal, J Electrochem Soc 125, 576 (1978)
67. B. E. Deal, D. W. Hess, J. D. Plummer and C. P. Ho, J Electrochem Soc 125, 339 (1978)
68. E. Ehara, K. Sakuma and K. Ohwada, J Electrochem Soc 126, 2249 (1979)
69. T. Nakayama and F. C. Collins, J Electrochem Soc 113, 706 (1966)
70. W. A. Pliskin, IBM J Res Dev 10, 198 (1966)
71. Y. Ota and S. R. Butler, J Electrochem Soc 121, 1107 (1974)

Figure 3. (Next page) Previous measurements of parabolic rate constants for thermal oxidation of Si in O₂ and steam. The values are those given by authors for oxidation at 1 atm. Where necessary, the quoted values were adjusted to 1 atm by assuming that B was linearly proportional to gas pressure.

KEY TO FIGURE 3

SYMBOL	SOURCE
●	B. E. Deal & A. S. Grove, J Appl Phys 36, 3770 (1965)
+	E. Rosencher, A. Straboni, S. Rigo & G. Amsel, Appl Phys Lett 34, 257 (1979)
▲	E. A. Irene, J Electrochem Soc 121, 1613 (1974)
△	E. A. Irene & G. Ghez, J Electrochem Soc 124, 1757 (1977)
✗	E. Ehara, K. Sakuma & K. Ohwada, J Electrochem Soc 126, 2249 (1979)
□	M. A. Hopper, R. A. Clarke & L. Young, J Electrochem Soc 122, 1216 (1975)
↑	Y. Ota & S. R. Butler, J Electrochem Soc 121, 1107 (1974)
○	B. E. Deal, D. W. Hess, J. D. Plummer & C. P. Ho, J Electrochem Soc 125, 339 (1978)
■	A. G. Revesz & R. J. Evans, J Phys Chem Solids, 30, 551 (1969)

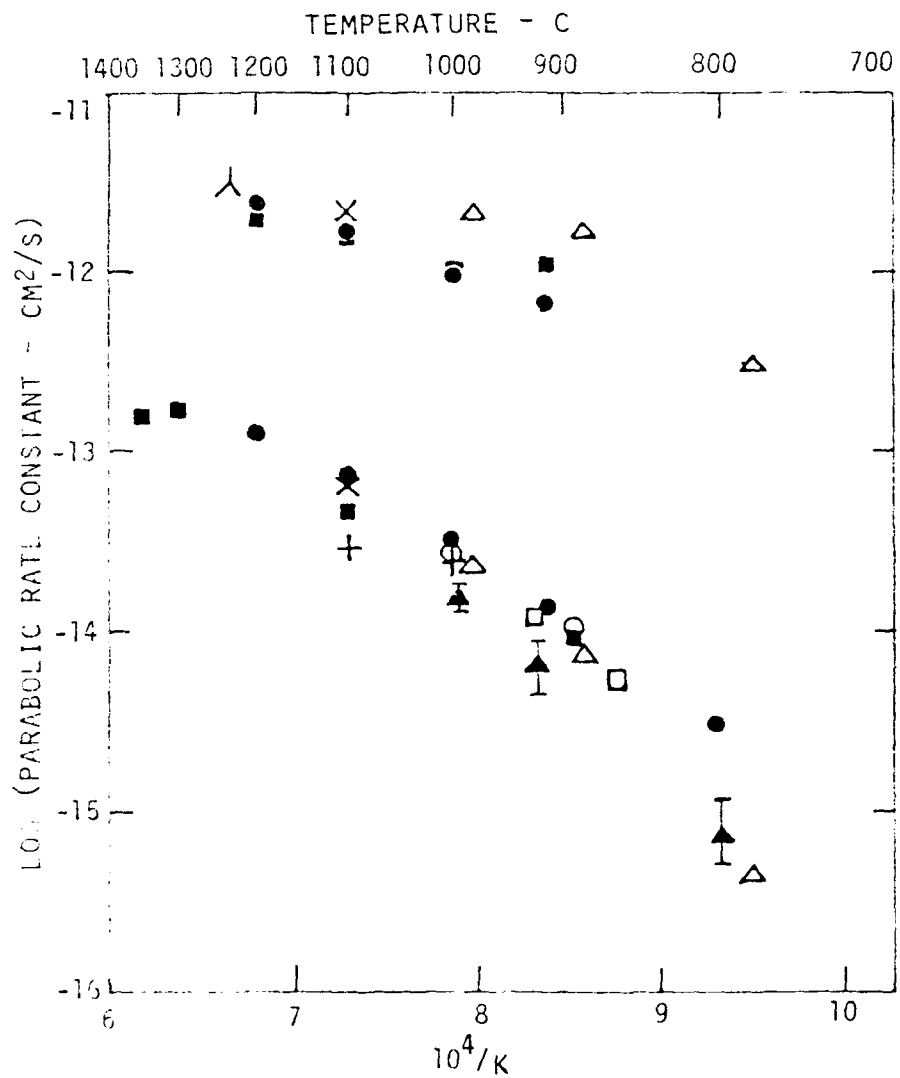
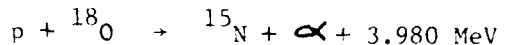


Figure 3. Previous measurements of parabolic rate constants for thermal oxidation of Si in O_2 and steam. Upper group all involve water vapor; lower ones oxygen. Note similarity of activation energy to permeation values.

Surface Profiling Techniques

Near-surface chemical analysis using ion beams is by now a common practice in materials research; see, for example, Thomas and Cachard (72), Mayer and Sauer (73) and Meyer et al (74). The technique most often employed is Rutherford Backscattering Spectrometry (RBS) (75), in which low-Z ions (at a fixed energy somewhere below 10 MeV) are directed at a sample. After scattering, the ions undergo large-angle nuclear (Rutherford) scattering at some depth within the sample, the ions themselves are detected by a detector capable of analyzing their energy. Since the ions lose energy throughout their path in the sample, the energy which remains upon their emergence (at a given scattering angle) serves to indicate the depth at which the scattering occurred. The energy spectrum of backscattered ions indicates the distribution of elements. It should be noted that since the elastic scattering cross section is a slowly varying function of energy, the probability of scattering is a function of depth (for near-surface events). RBS finds a significant limitation in determining distributions of high-Z impurities in low-Z matrices. The large difference in scattered ion energy following high-Z and low-Z scattering events makes the two types of scattering readily distinguishable while the Z^2 dependence of the Rutherford cross section suppresses the contribution of the low-Z matrix.

In determination of oxygen distributions, however, the analysis technique employed in this study was that of nuclear resonance profiling (76, 77). This technique, as applied to 180 O profiling, is illustrated in Figure 4. A collimated beam of protons from a Van de Graaf electrostatic accelerator bombards the oxide layer after being energy analyzed. The cross section for the nuclear reaction $^{180}(\text{p}, \alpha)^{15}\text{N}$ between the protons and the 180 O, namely



induced narrow resonance at a proton energy of 629 keV (Mayer and Sauer, 1973). Protons enter at a higher energy than that, and lose

- i. N. Thomas and A. Cachard, Material Characterization Using Ion Beams (Academic, 1978)
- ii. J. Sauer and E. Rimini, Eds., Ion Beam Handbook for Materials Analysis (Academic, 1977)
- iii. J. Sauer, G. Linker and F. Kappeler, Ion Beam Surface Layer Analysis (Academic, 1976)
- iv. W. K. Chu, J. W. Mayer, and M. A. Nicolet, Backscattering Spectrometry (Academic, 1978)
- v. K. L. Dunning & H. L. Hughes, IEEE Trans Nucl Sci. NS-19, 6, 243 (1972)
- vi. G. Amself, J. P. Nadai, E. D'Artemaire, D. David, E. Girard and J. Moulin, Nucl. Inst Meth 92, 481 (1971)

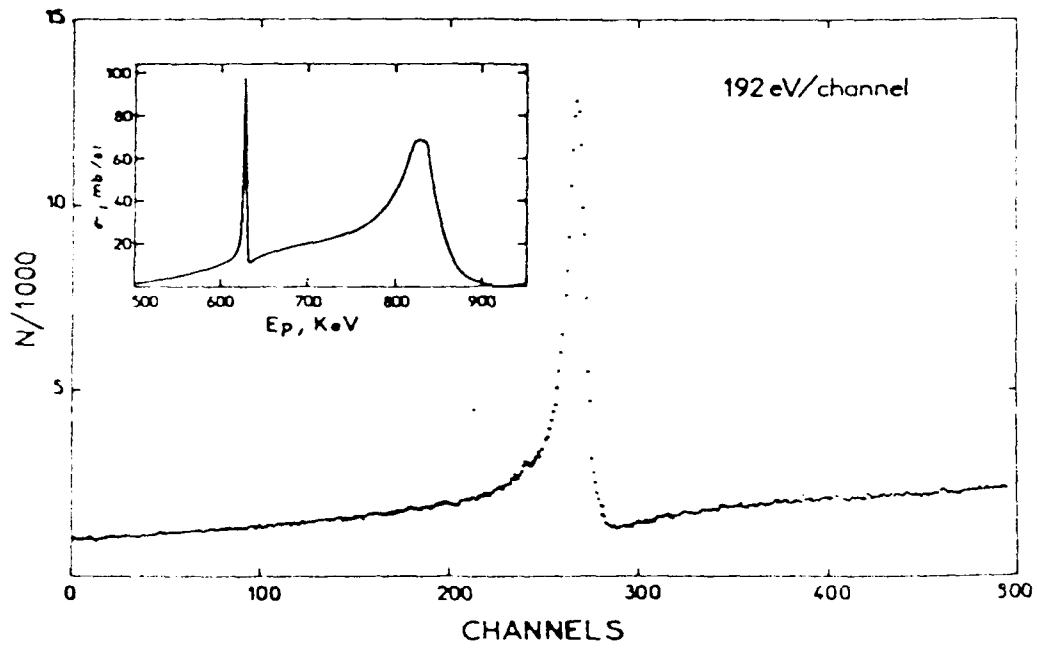
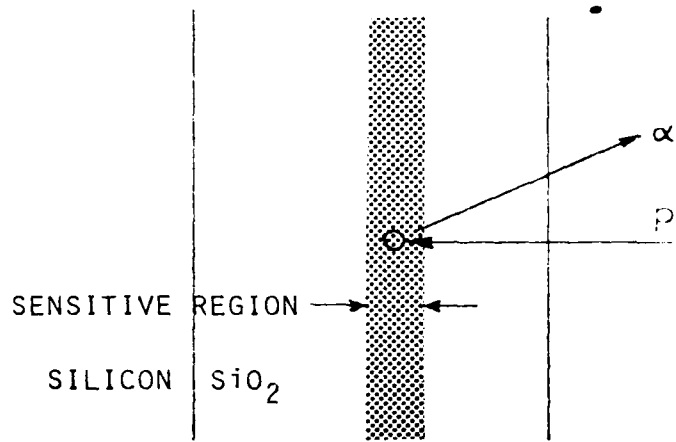


Figure 4. Principle of nuclear resonance profiling. The graph shows the cross section vs incident proton energy at $\theta_{\text{lab}} = 150^\circ$ for $^{18}\text{O}(\text{p},\alpha)^{15}\text{N}$ reaction. The peak energy is at 629 keV; protons enter with slightly higher energy. The sensitive region is located at the depth where the proton energy has fallen to that value. Alpha particles, emitted with an energy of 3.4 MeV, easily escape. (From Mayer and Rimini, p 163 (73))

energy continuously along their path in the layer until they reach the resonance energy, at which depth the reaction occurs. (The reaction can, of course, occur at any other depth, but with much less likelihood.) Alpha particles produced via the reaction escape from the surface and are detected; their yield (relative to the proton fluence) indicates the ^{18}O concentration at that depth. By systematically varying the energy of the proton beam and observing the alpha particle yield, the ^{18}O concentration profile can be determined.

In order to determine an unknown ^{18}O concentration profile by the technique of nuclear resonance profiling, one observes the yield of alpha particles (per steradian per incident proton) from the reaction of protons with ^{18}O distributed within the oxide layer. A general expression for the alpha particle yield (vs. proton beam energy) is

$$Y(E_b) = \int_0^{x_0} dx \rho(x) \int_0^{\infty} dE_i g(E_b, E_i) \int_0^{E_i} dE \frac{d\sigma}{d\Omega}(E) f(E, E_i, x) \quad (14)$$

where

E_b is the mean energy of the incident proton beam,

E is the energy of the reacting protons,

E_i is the actual energy of protons incident on the surface of the layer,

x_0 is the thickness of the oxide layer,

x is the depth at which the reaction occurs,

$\rho(x)$ is the ^{18}O concentration profile (i.e. atoms per unit volume at depth x),

$\frac{d\sigma}{d\Omega}$ is the differential cross section of the $^{18}\text{O}(\text{p}, \alpha)^{15}\text{N}$ reaction,

$g(E_b, E_i)dE_i$ is the fraction of protons in the beam which have an incident energy between E_i and $E_i + dE_i$,

$f(E, E_i, x)dE$ is the probability that a proton which has started with energy E_i and arrived at depth x will have an energy between E and $E + dE$.

If the functions $g(E_b, E_i)$, $f(E, E_i, x)$ and $\frac{d\sigma}{d\Omega}(E)$ are all previously known and the yield $Y(E_b)$ is observed, then the function $\rho(x)$ can in principle be determined by inversion of the integral equation.

An enlightening discussion of this matter appears in Dunning et al (78), in which a similar calculation (involving the $^{27}\text{Al}(\text{p}, \gamma)^{28}\text{Si}$ reaction) appears.

It should be noted that the energy of the emerging alpha particles is (a) considerably greater than that of the incident protons, and (b) almost equal to the Q-value of this inelastic reaction. They lose at most about 40 keV (having been emitted with 2.4 MeV) in traversing the 2000 Å thick SiO_2 layers in this study (Mayer and Rimini, p. 16 (73)).

Applications of nuclear resonance profiling of ^{18}O have included oxygen diffusion in ZrO_2 (79), silicon (80), GaP (81), TiO_2 (82), TiO_2 and Cr_2O_3 (83), and water diffusion in Ta oxide (84).

Nuclear resonance profiling contrasts with RBS in several important respects. First, since the depth at which the reaction occurs is determined solely by the incident particles' energy, the detection system need not provide energy analysis for the reaction product (except to screen out products of competing reactions). Second, the specificity of the reaction allows the detection of minute quantities of an isotope in the presence of any other material (subject to the non-interference of other reactions). This makes it especially valuable for detection of low-Z materials, whose resonant reactions tend to be readily distinguishable. Third, and most important, narrow resonances provide high resolution in depth - the 2.1 keV width of the 629 keV ^{18}O resonance corresponds to a depth spread of 350 Å (as is discussed in greater detail later).

73. J. W. Mayer and E. Rimini, Eds, Ion Beam Handbook for Materials Analysis (Academic, 1977)
78. K. L. Dunning, G. K. Hubler, J. Comas, W. H. Lucke and H. L. Hughes, Thin Solid Films 19, 145 (1973)
79. G. Amsel, G. Beranger, B. deGelas and P. Lacombe, J Appl Phys 39, 2246 (1968)
80. J. E. Gass, H. H. Muller, H. Schmied, L. Jorissen and G. Ziffermayer, Nucl Inst Meth 106, 109 (1973)
81. J. L. Whitton, I. V. Mitchell and K. B. Winterbon, Can J Phys 49, 1225 (1971)
82. J. M. Calvert, D. J. Derry and D. G. Lees, J Phys D: Appl Phys 7, 940 (1974)
83. D. J. Neild, P. J. Wise and D. G. Barnes, J Phys D: Appl Phys 5, 2292 (1972)
84. S. Rigo, B. Maurel, and G. Amsel, Electrochem Soc Abstract #182, Spring Meeting, Seattle (21 May 1978)

It is important to distinguish nuclear resonance profiling from the other principal profiling technique based on direct observation of nuclear reactions (85, 86). That technique, pioneered by Amsel (1963), uses reactions in an energy domain where the reaction cross section is a slowly varying function of energy. As in RBE, the energies of the emerging reaction products are analyzed; the depth distribution of reacting material is provided by the resulting energy spectrum. This technique has been employed in a number of studies involving oxygen, including 160 diffusion in Alpha-zirconium (87, 88), 170 diffusion in zirconium oxide (89), 180 diffusion in quartz (90), and determination of 160 concentration profiles in SiO_2 films (91).

85. E. Ligeon and A. Bontemps, J. Radioanal Chem 12, 335 (1972)
86. G. Amsel and D. Samuel, Anal Chem 39, 1689 (1967)
87. D. David, G. Amsel, P. Boisot and G. Beranger, J Electrochem Soc 122, 388 (1975)
88. G. Amsel, G. Beranger, B. deGelas and P. Lacombe, J Appl Phys 39, 2246 (1968)
89. R. W. Ollerhead, El Almqvist and J. Kuehner, J Appl Phys 37, 2440 (1966)
90. A. Choudhury, D. W. Palmer, G. Amsel, H. Curien and P. Baruch, Sol St Comm, 3, 119 (1965)
91. A. Turos, L. Wielunski, A. Barcz and J. Olenski, J Radioanal Chem 16, 627 (1973)

EXPERIMENTAL PROCEDURE

Materials Preparation

Single-crystal silicon wafers (2" diam) were obtained from Monsanto Corp. They were of (100) orientation, with one face polished; their resistivity was 4 ohm-cm (n-type). They were first degreased in boiling trichloroethylene, cleaned in both H₂SO₄ (at 90 C) and HF, and rinsed in deionized water. They were then oxidized to 2000 Å in flowing dry oxygen at 1 atm at 1200 C in a commercial 3-zone tubular furnace (Thermco) which was lined with a quartz diffusion tube. Both the sample preparation and oxidation procedures are standard in the semiconductor processing industry.

Following the oxidation, ¹⁸O was implanted into the SiO₂ films. The ¹⁸O was in the form of isotopically enriched gas (70 atom %, obtained from ProChem Isotopes), a lecture cylinder of which was mounted in a commercial ion accelerator (at RCA Laboratories, Princeton, N. J.). This device ionized the gas, then electrostatically accelerated the ions to the desired energy through a mass analyzer which accepted only ions of the desired atomic weight. The implantation was accomplished by raster-scanning the ion beam across the polished faces of the wafers to provide a uniform fluence of $3(10)^{15}$ ions/cm². To avoid H₂¹⁶O contamination, the mass analyzer was set at 36 AMU rather than 18 AMU, so that the projectile ions were actually (¹⁸O-¹⁸O)⁺. To reach the desired depth, the molecular energy was set at 80 keV per nucleus). A mass analysis of the residual gas within the ion implantation apparatus, which appears as Figure 5, showed the major contaminants to be (¹⁶O-¹⁸O), ¹⁵N₂ and ⁴⁰Ar, in quantities insufficient to affect the fluence measurement significantly. The wafers received no immediate post-implant treatment.

Finally, samples were prepared by cleaving the oxidized and implanted wafers into 5mm x 10mm sections which had been individually labeled to indicate their original locations on the wafers.

Thermal Treatments

The general procedure involved heating samples in atmospheres containing various water vapor concentrations. In each atmosphere, samples were heated at a number of temperatures in order to determine the activation energy of diffusion in equation (3). Comparison of the pre-exponential factors D₀* obtained in different atmospheres at a single temperature provided the means of determining the pressure dependence of D*. The extent of ¹⁸O diffusion as a function of heating time at a fixed temperature and atmosphere was observed in order to determine reaction rates involved in water permeation.

Temperature Dependence

The first set of thermal treatments was carried out in room air. The room was maintained at a temperature of 21 C and a relative humidity of approximately 50%. Samples were placed in a horizontal 3-zone tubular alloying furnace, (Pacesetter II, Thermco Products Corp.) lined with a 6.4 cm ID X 91 cm long fused quartz diffusion tube, open at one end. The furnace was equipped with a proportional temperature controller (Ana-Lock Series 321, Thermco Products Corp.) for each of its three integral Type K (Ni-Cr/Ni-Al) thermocouples. Sample temperatures were monitored by means of a separate type R (Pt/Pt-13%Rh) thermocouple which was inserted in the diffusion tube.

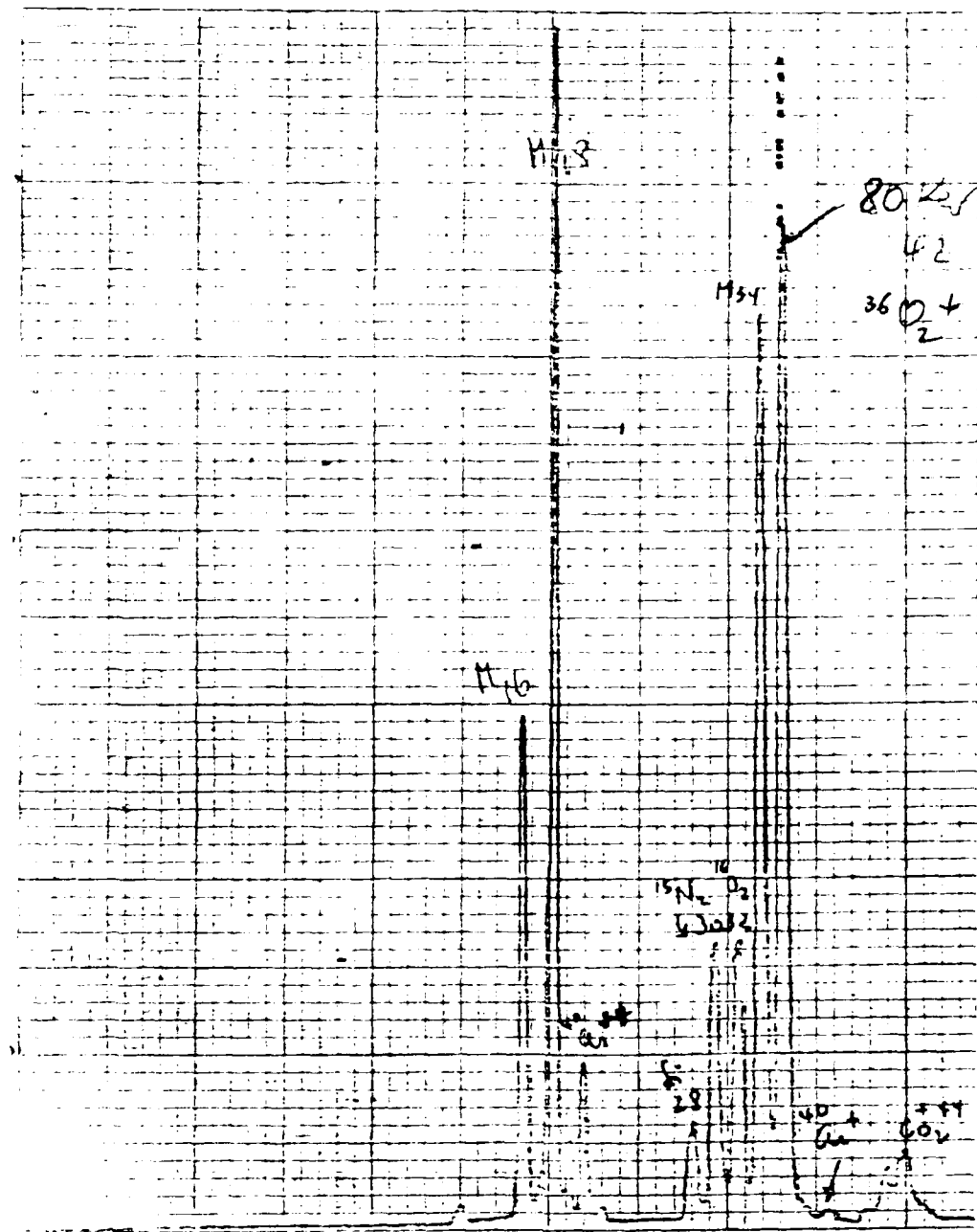


Figure 5. Analysis of residual gas in ion implantation apparatus. The horizontal scale indicates molecular weight of detected species; the vertical scale their relative abundance. $^{36}\text{O}_2^+$, the accelerated ion, is off scale vertically.

The thermocouple wires were fixed within a 91 cm long X 0.6 cm OD quartz tube; the hot junction was located near its closed end. The thermocouple indicator (Model DS-350, Doric Scientific Corp.) had been factory-calibrated for a type R thermocouple; it had a digital display with a resolution of 0.1 C. The furnace controls were adjusted while monitoring the temperature at various points so that an 8 cm long "flat-zone" was obtained near the center. Diffusions were carried out by loading a batch of samples on a 4.1 cm X 15 cm plate-type slotted carrier made of fused quartz (obtained from Quartz International Corp.) which had been preheated for at least 45 minutes at the center of the furnace. The carrier was pulled out to the mouth of the diffusion tube using a hooked quartz rod, the samples were loaded quickly and the carrier returned to a position such that the samples were within the flat zone; the thermocouple was then inserted adjacent to the samples. Sample placement and/or removal involved withdrawing the carrier from the furnace for no more than half a minute per operation. Samples were transferred to a room-temperature pyrex surface where they cooled rapidly. Samples were always placed with the implanted face up. Timing was done with a quartz-crystal digital wrist watch.

The next set of thermal treatments was carried out in dry nitrogen at 1 atm. The same furnace controller, thermocouple and diffusion tube were used. A fused quartz diffusion-type end cap was placed on the gas supply end of the diffusion tube; the other end was left open. Gas was obtained via boiloff of liquid nitrogen; flow was maintained using a tube flowmeter (Sho-Rate, Brooks Instrument Company) at 500 cc/min (equivalent at 70° F, 1 atm).

A similar procedure was followed for thermal treatments in steam at 1 atm. In this case, however, the furnace at first was a horizontal single-zone tubular resistance furnace (Model 54233, Lindberg/General Signal), lined with a 5.1 cm ID x 91 cm long fused quartz diffusion tube. The furnace was equipped with an integral proportional temperature controller (Model 59544, Lindberg/General Signal) for the furnace's integral thermocouple. After a time, the furnace and controller were replaced with a horizontal single-zone tubular resistance furnace (Model 1127, Marshall Furnace Co.) lined with a 3.8 cm ID x 117 cm long fused quartz diffusion tube. Furnace temperature was controlled using a proportional controller (Eurotherm Model 901-2075, Marshall Furnace Co.) and a type K thermocouple whose junction was located at the center of a small tube bored parallel to the furnace tube. Sample temperatures were monitored by means of a separate type K thermocouple whose hot junction was located near the closed end of a 91 cm long x 0.95 cm OD quartz tube, which was inserted in the diffusion tube. The thermocouple EMF was read out on the 200 mV scale of a 3-1/2 digit multimeter (Model 8020A, John Fluke Corp.), and converted to temperature with the aid of appropriate tables (Omega, 1979). The readings were compensated for cold junction temperature by means of an electronic cold-junction compensator (Model MCJ-K, Omega Engineering Corp.). The type K and R thermocouples were cross-checked by putting both into the furnace at various temperatures between 550 C and 600 C.

The type K thermocouple was calibrated by separating the two wire ends and bridging them with a small horizontal strip of silver foil whose surfaces had been cleaned by abrasion. The ends of the silver strip were crimped onto

the wires, which were then heated under high vacuum. The last DMM reading before the strip melted corresponded to a temperature of 958 C, which is within 4 C of the melting point of silver (1). This discrepancy was judged to be within the error of reading on the digital multimeter, especially since the temperature was still increasing at the time of the last reading, so that the meter readings were taken as indicating the true temperature.

The steam was generated by boiling deionized water in a stoppered 2-liter boiling flask, as shown in Figure 6. The boiling rate was governed by a variable autotransformer supplying power to a hemispherical heating mantle around the flask. Steam was conducted to the diffusion tube through a horizontal pyrex tube emerging from the neck of the flask; this was joined to the narrowed end of the diffusion tube via a tapered ground joint. The entire length of horizontal tubing and the neck of the flask were wrapped in fiberglass heat-shield tape and maintained at a temperature of 120 C to avoid condensation there. Temperature was monitored with a Type T (copper-constantan) thermocouple. An anti-backstreaming plug, formed by a wad of fiberglass tape, was inserted into the thermocouple tube. When inserted into the diffusion tube, it provided a slight positive pressure to be maintained in the furnace. Sample insertion, a procedure which took approximately 15 seconds, was delayed until the air had been replaced by steam and the furnace temperature had stabilized. The samples rested on a 2 cm x 6.5cm quartz boat which was inserted to the center of the furnace with a hooked steel rod.

Pressure Dependence

Finally, a set of thermal treatments was carried out in pure water vapor at reduced pressures. These were performed within the 46 cm diameter x 79 cm high bell jar of a vacuum evaporation station (Model VS-400, Veeco Corp.), as shown in Figure 7. The samples were placed inside a 17.6 cm long section of 1.9D quartz tubing. A double-hole ceramic rod with a type K thermocouple probe at one end was also inserted in the tubing so that the junction was near the sample location. The tubing was then inserted into a 1.35 cm ID x 10.5 cm long tubular resistance furnace so as to put the sample at its center. The furnace mount, a small pedestal, rested on the 61 cm diam stainless steel baseplate of the evaporation station. Electric power for the furnace was supplied by a variable autotransformer through feedthroughs in the baseplate; about 80W was required to maintain a sample temperature of 800 C. The thermocouple wires were likewise connected to electrical feedthrough in the baseplate. Water vapor was supplied by deionized water in a stoppered vacuum flask resting on a thermostatic hotplate to maintain a constant water temperature. The vapor was conducted through a length of copper tubing to a variable flow valve (micrometer type), and entered the vacuum chamber through the variable resistance valve. A continuous flow was maintained by exhausting the chamber through a choked-down roughing valve to a mechanical forepump (Model 140, Sargent-Welch Scientific Co.). Chamber pressure was monitored by a capacitive manometer (Baratron Pressure Meter Type 220-2A3-10, MKS Instruments, Inc.) whose sensing tube entered the chamber through a port in the baseplate. Signals from both the manometer and the thermocouple were read via digital multimeters and recorded on strip chart recorders (Model 680, Hewlett-Packard Corp.).

1. R. C. Weast, Handbook of Chemistry and Physics, 55th ed (CRC Press, 1974)

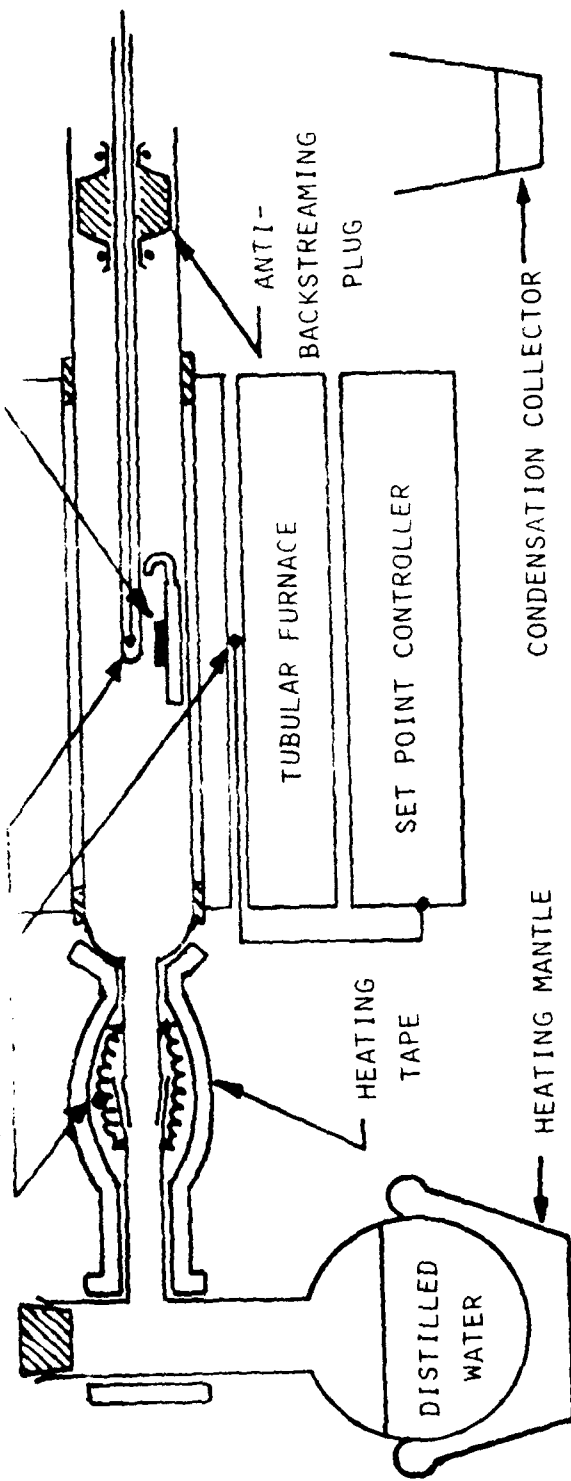


Figure 6. Apparatus for thermal treatments in steam.

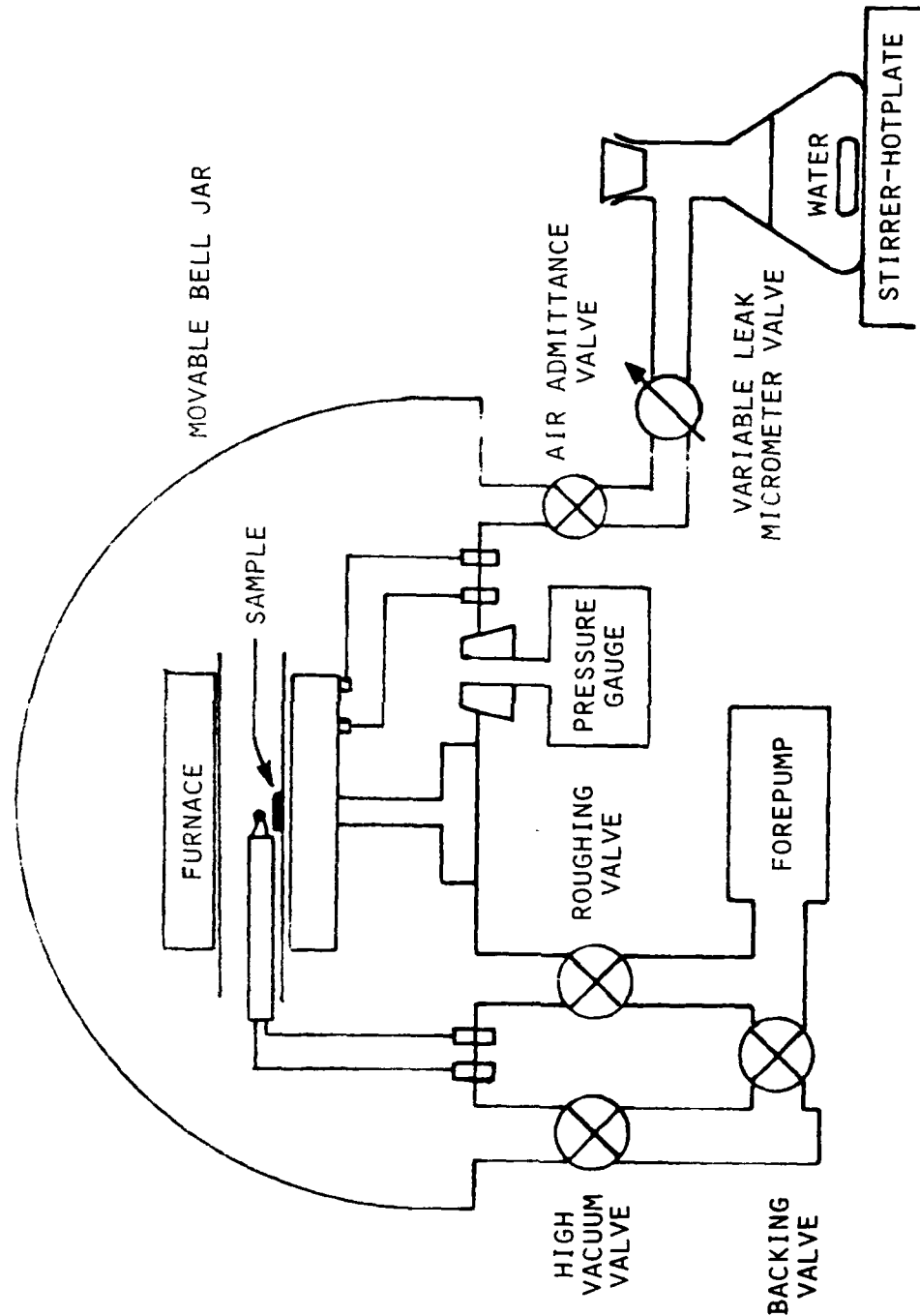


Figure 7. Apparatus for thermal treatments at low pressure.

The thermal treatments were carried out by first loading the samples and thermocouple in the furnace. The bell jar was then lowered and the system evacuated by the forepump through the diffusion pump backing line. For this operation, the high-vacuum valve, the backing valve and the air admittance valve were all fully open, while the roughing valve, the mechanical pump venting valve and the variable leak valve were all shut. The latter was then opened to evacuate the air from the water supply flask and tube and to degas the water, then shut to re-evacuate the system. Next, water vapor was admitted by adjusting the variable leak valve until the observed rate of pressure increase was such that the pressure reached its desired value in 5 min. At that point the roughing valve was "cracked" open to maintain that value stably. The system was again evacuated, this time through the backing valve, and the furnace was brought up to temperature. No difficulty was encountered in keeping the temperature constant to within about $\pm 3^\circ\text{C}$ by manually adjusting the autotransformer voltage. The pressure was then brought up to its present level through shutoff of the backing valve. On short runs, pressure excursions were prevented through manual adjustment of the variable leak valve; on longer runs they amounted to something like $\pm 20\%$ of the average value.

Alpha Spectra - Rotilling

In order to determine the extent of ^{18}O diffusion induced by the thermal treatments, alpha particle yield curves were taken using the method of nuclear magnetic resonance as previously described in the Introduction. A proton beam was produced at 630 keV Van deGraaff electrostatic accelerator (Model A, High Voltage Engineering Corp.). A portion of the accelerator, as well as the ancillary apparatus, is shown in Figures 8 and 9; prominent features are indicated in the preceding key.

The proton energy was controlled by adjusting the field strength of a 90°-deflection rotilling magnet. The current to the magnet coils was supplied from a high-current, regulated power supply. The magnetic field strength was measured in terms of an NMR gaussmeter (Model M2, Nuclear Magnetics Corp./General Electrics) whose probe element was fixed between the flat faces of the magnet. The gaussmeter modulated the local magnetic field at the Larmor frequency via a pair of small Helmholtz coils. The RF oscillator was set to a frequency corresponding to the desired beam energy, and the beam energy was adjusted by varying the magnet current until the NMR signal dip centered at the zero of the modulation current. An oscillator frequency of 12.050 MHz was used (as read on a Hewlett-Packard Model 5243L digital frequency counter) corresponding to a beam energy of 630 keV. Excursions in the magnetic field were kept small enough to limit beam energy variations to under ± 40 eV during a typical 1.5-2 min duration alpha particle count.

KEY TO PHOTOGRAPHS OF NUCLEAR PROFILING APPARATUS (pp 33, 34)

- A. VAN DE GRAAFF VERTICAL DRIFT TUBE: Protons travel downward.
- B. FRAME OF ANALYZING MAGNET (Coils are in dark area below): Protons undergo 90° deflection with 38 cm radius of curvature, then emerge toward right.
- C. SCATTERING CHAMBER: D-shaped, multiport. On its rear plate is a horizontally translatable stage upon whose rotatable center is mounted the sample holder. Protons enter a front port, housing collimator, which is attached to the horizontal beam tube.
The ports hold vacuum gauge, electrical feedthroughs, vacuum system and viewing window.) Extending through the top of the chamber is a rotatable feedthrough for changing detector angle from the outside. Beyond it stands a switchable microammeter, connected to the collimator sectors for beam alignment.
- D. CHARGE SENSITIVE PREAMP: Mounted on rotatable feedthrough holding detector.
- E. CINTILLATION DETECTOR. NaI(Tl) crystal/photomultiplier tube assembly and plug-in preamp, shielded with lead bricks, for gamma ray calibration of beam energy. It should be noted that the letter "E" in the upper right corner is a wall plaque denoting "East" rather than a label for this diagram.
- F. NIM BIN: Spectroscopy and DDL amplifiers. Below this is the -V power supply for the photomultiplier.
- G. OSCILLATOR UNIT: For NMR gaussmeter, connected by a short cable to probe mounted in magnet gap on far side. Immediately to its right is a digital counter to facilitate setting frequency; to its right is an RF amplifier for oscillator signal.
- H. OSCILLOSCOPE: Used to display NMR signal. To its left (not shown) is magnet current controller, NMR power supply (modified to include varactor for remote trimming of oscillator frequency) and digital frequency counter.
- I. OSCILLATOR'S CONSOLE FOR VAN DE GRAAFF ACCELERATOR.
- J. 16 CHANNEL PULSE HEIGHT ANALYZER.
- K. TARGET CURRENT INTEGRATOR.

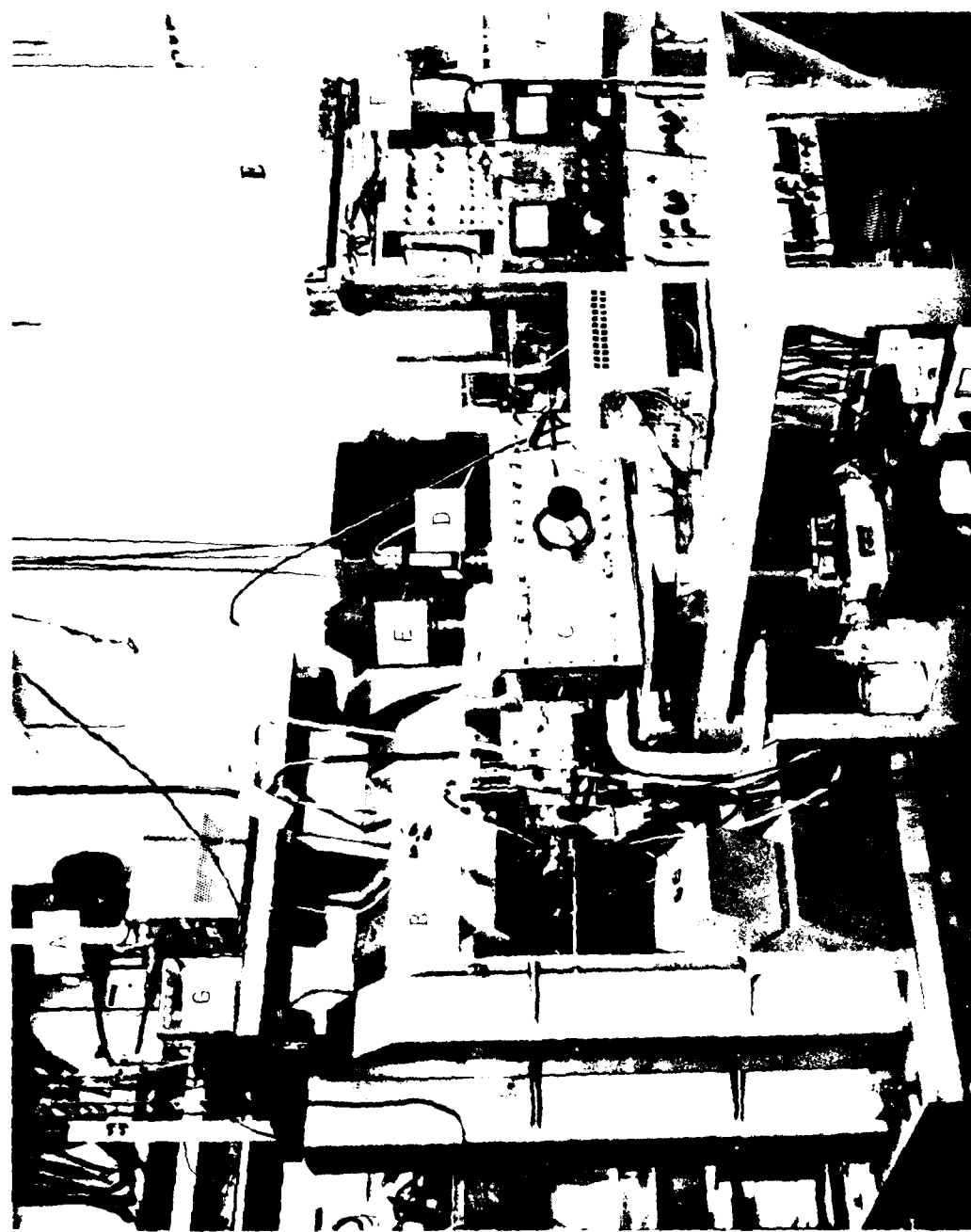


Figure 8. Van de Graaff accelerator: experimental area.

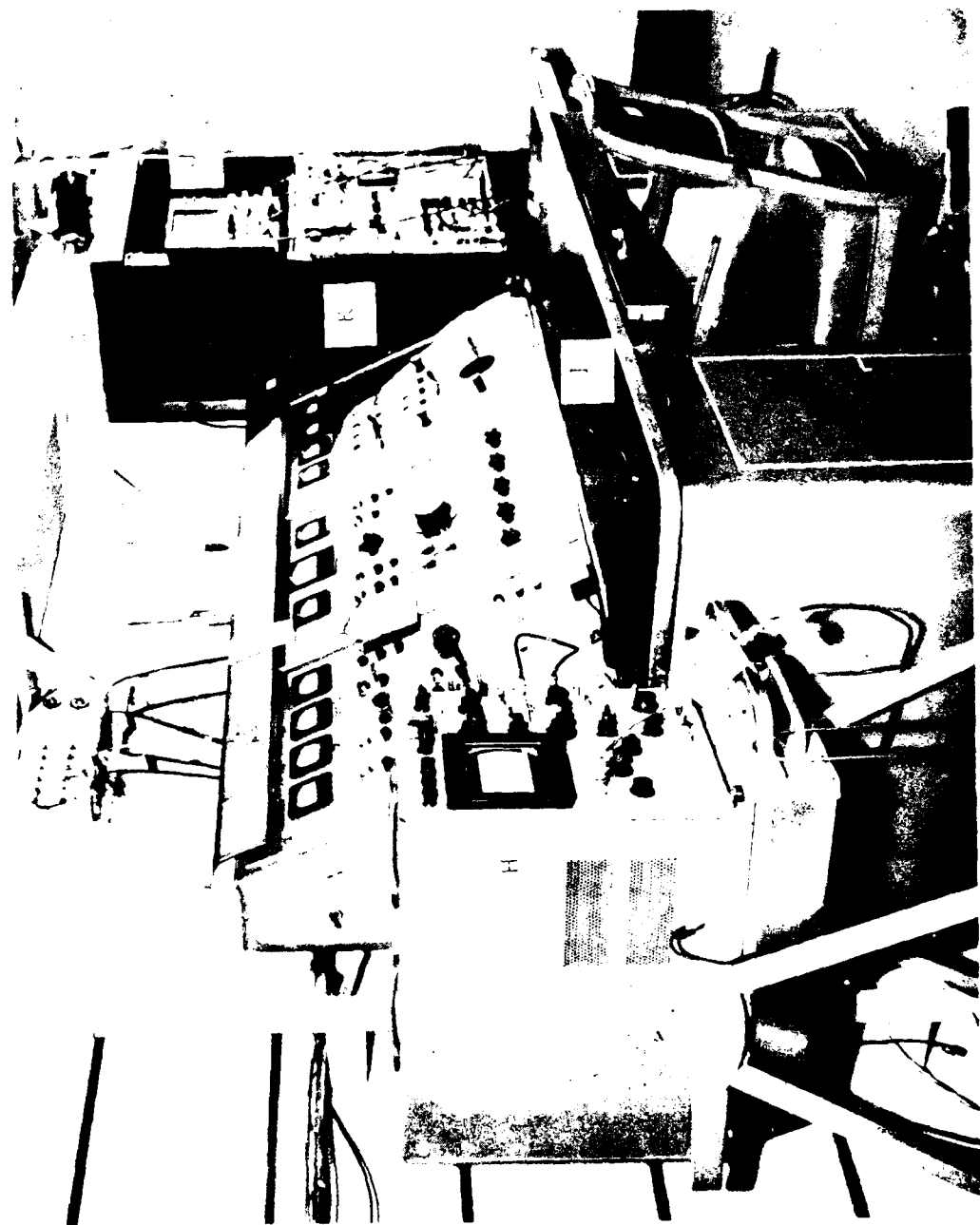


Figure 9. Van de Graaff accelerator: operating console.

Immediately beyond the analyzing magnet was a pair of control slits. These served to allow passage of only those protons with the set energy, as well as to provide a feedback signal for closed-loop fine control of beam energy. Beyond these lay the horizontal beam tube, at the end of which was a stainless steel multiport scattering chamber, shown schematically in Figure 10. This housed a sample holder and a particle detector. The sample holder was a 4.9 cm diameter stainless steel disc with a shallow groove milled across its face; batches of samples stood side by side in the groove and were held in place by small clips extending over its edges. Each batch included a reference sample that had been ^{18}O -implanted but not thermally treated. The sample holder was mounted with its face normal to the proton beam and biased at ± 45 V to collect secondary electrons; it was movable from outside the chamber, as was the detector mount. The detector was a silicon surface barrier device (25 mm^2 area, $100 \mu\text{m}$ depletion depth, Ortec) located 17 mm from the sample at an angle of 150° to the beam direction. It was shielded by a polyester film whose thickness of $1.3 \text{ mg}\cdot\text{cm}^{-2}$ was sufficient to prevent any backscattered protons from reaching it while allowing penetration of the 3.4 MeV alpha particles. The detector pulses, after being amplified (by a Model 6760 Charge-Sensitive Preamplifier and Model 1417 Spectroscopy Amplifier, both Canberra Corp.), were displayed on a 2048-channel pulse height analyzer (Model 1765, Tracor-Northern Corp.), which performed a "region-of-interest" function: it displayed a running total of pulses accumulated in the alpha-particle peak. This was frozen by a signal from a current integrator (Model 1430, Tracor Corp.) indicating that the proton fluence on the sample had reached a pre-set value (typically 50 μC). The "region of interest" was an energy band straddling the alpha particle energy; it was set on the PHA so as to include all the alpha particles registered in the narrow, well-defined 3.4 MeV peak. Background counts were negligible. Alpha particle counts ranged from 1000 to 5000 per $50 \mu\text{C}$ run; beam current was held to $0.5 \mu\text{A}$ to avoid heating the samples (see Discussion for clarification of this point). At each beam energy setting, the sample holder was translated to place each of the samples consecutively in the 1 mm-diameter beam. The range of beam energy settings spanned typically 13 keV on either side of the energy at which the alpha yield was maximum. This corresponded to a projected range of $\pm 17 \mu\text{m}$ on either side of the location of the distribution peak - enough to raster scanning of the entire 2000 Å thickness of the oxide layer.

Before any alpha yield curves were taken, a calibration was performed on the de Graaf accelerator in order to functionally relate the proton beam energy to the observed NMR oscillator frequency. This was done also by means of nuclear resonance profiling, but with (p,γ) rather than (p,α) reactions. (This reflects the reactions used.) A thick target containing a uniform concentration of appropriate nuclide was placed in the proton beam, whose energy was systematically varied. The yield of gamma rays was plotted as a function of NMR frequency. As the NMR frequency (and thus the proton energy) was systematically increased, the yield increased relatively slowly as long as the proton energy remained below the relevant resonant energy. (These gamma rays came from a multitude of small resonances in the (p,γ) cross section.) However, as soon as the proton energy reached the main resonant energy, the yield increased suddenly, reflecting the increased number of interactions at that energy. As the proton energy was further increased, the yield resumed its slow rise, reflecting the slow variation in the reaction cross section. An example of a thick-target gamma-ray yield curve is shown in Figure 11.

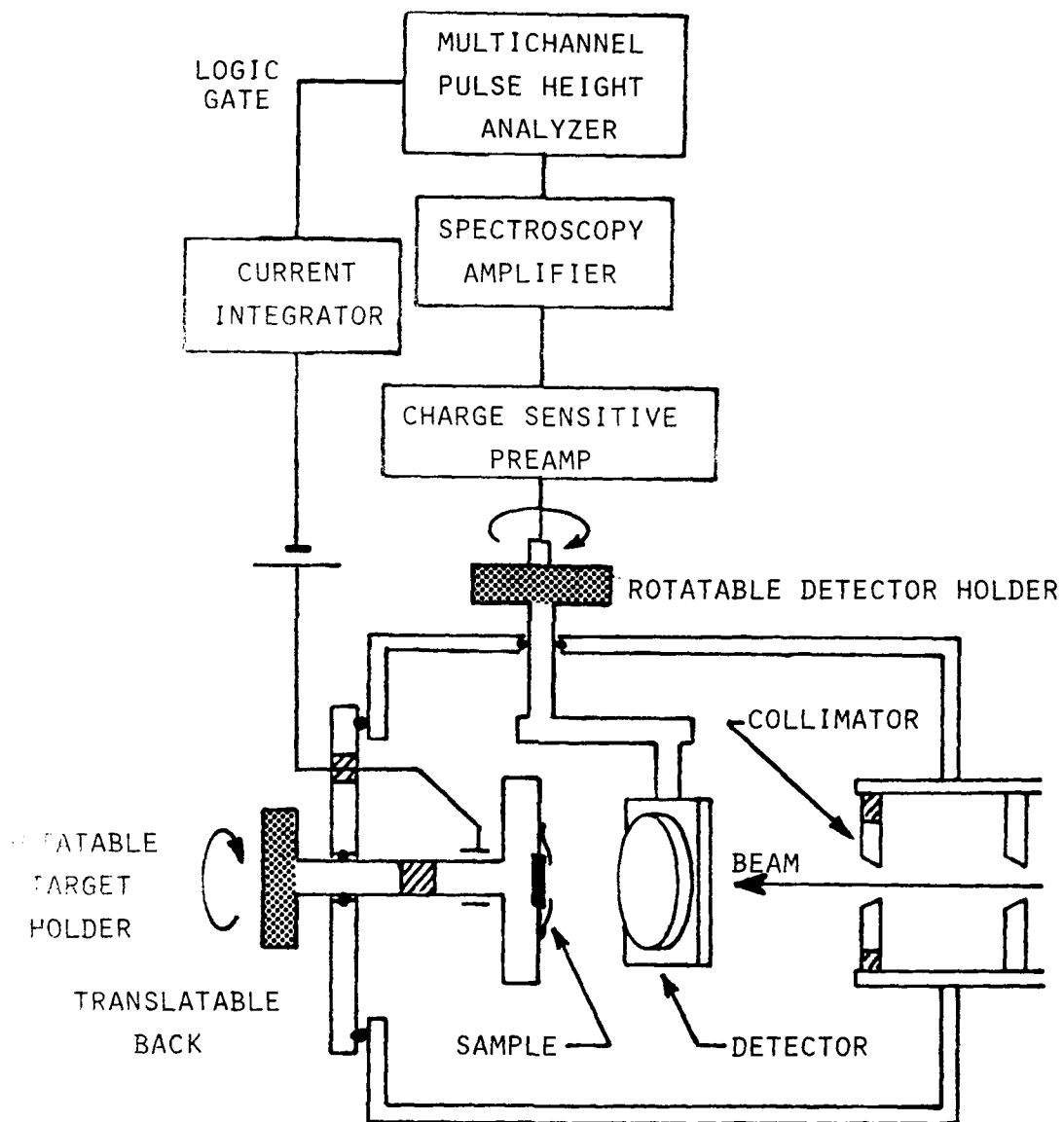


Figure 10. Nuclear scattering chamber. Successive samples are irradiated by horizontally translating the back. Target current is collected by a slip ring to allow rotation. See KEY TO PHOTOGRAPHS for more description.

TABLE 1. ACCELERATOR ENERGY CALIBRATION REACTIONS

<u>Reaction</u>	<u>E_p (keV)</u>	<u>Γ (keV)</u>	<u>E_γ (MeV)</u>	<u>σ (mb)</u>	<u>Observed ν_{nmr} (MHz)</u>
$^{19}\text{F}(p, \alpha \gamma)^{16}\text{O}$	340.5	2.4	6.13	160	8.930
$^7\text{Li}(p, \gamma)^8\text{Be}$	441.4	12.2	17.64	6	10.230
$^{19}\text{F}(p, \alpha \gamma)^{16}\text{O}$	872.1	4.7	6.13, 6.92	540	14.200
$^{27}\text{Al}(p, \gamma)^{28}\text{Si}$	991.9	0.10	12.54	-	15.086

Reference: Mayer and Rimini (2)

2. J. W. Mayer and E. Rimini, Eds., Ion Beam Handbook for Materials Analysis (Academic, 1977), pp 207, 281

The calibration proceeded as follows: A target thick compared to a 1 MeV proton range was prepared. In the case of Al this was a small block of 1/8" stock; in the cases of Li and F it was a layer of LiF formed by fusing LiF crystals on a copper disk. The target was placed on the sample holder and a scintillation detector (a 5"x5" NaI(Tl) crystal attached to a 5" photomultiplier tube) was placed on the scattering chamber nearby. Lead bricks were positioned upstream to shield the crystal from gamma rays coming from various beam stops. As before, an NMR frequency was selected, and detector pulses were displayed on a multichannel pulse height analyzer, where those in an appropriate energy range were accumulated until a preset target charge had been reached. The appropriate gamma ray energy range was selected on the basis of a detector-analyzer system calibration (using ^{60}Co and ^{137}Cs standard reference sources) to include the principal gamma rays emitted in the reactions listed in Table I. The resulting thick-target gamma ray yield was plotted, and the accelerator energy was calibrated by identification of the NMR frequency at which the step in the yield curve occurred (i.e., the last entry in Table I) as the proton energy corresponding to the resonance.

Since NMR frequency is proportional to the analyzing magnet's field strength and the magnetic force is equal to the centrifugal force on the electrons, the proton energy is proportional to the square of the NMR frequency. It was found to be approximately

$$E_b \text{ (keV)} = 4.36 v^2 \text{ (MHz)}.$$

The main cause of inaccuracy is the nonuniformity of the field over the dimensions of the iron pole pieces: the probe, being of necessity located near the fringe, could not accurately reflect conditions along the beam path. It should be stressed, however, that this experiment is self-calibrating - the narrow width of the $^{18}\text{O}(\text{p},\alpha)^{15}\text{N}$ reaction allows the reference sample (immediately but unheated) to provide an energy calibration for every other sample in the chamber.

The beam was not purely monoenergetic: due to differences in trajectories there was a distribution of incident proton energies. This was determined from the gamma ray yield calibration curve for the $^{27}\text{Al}(\text{p},\gamma)^{28}\text{Si}$ reaction shown in Figure 11. Noticeably, the step is not sharp, but has a finite width (here on the order of 1 keV). Since the reaction width is less than 0.1 keV, this deviation is almost entirely attributable to the energy spread of the beam.

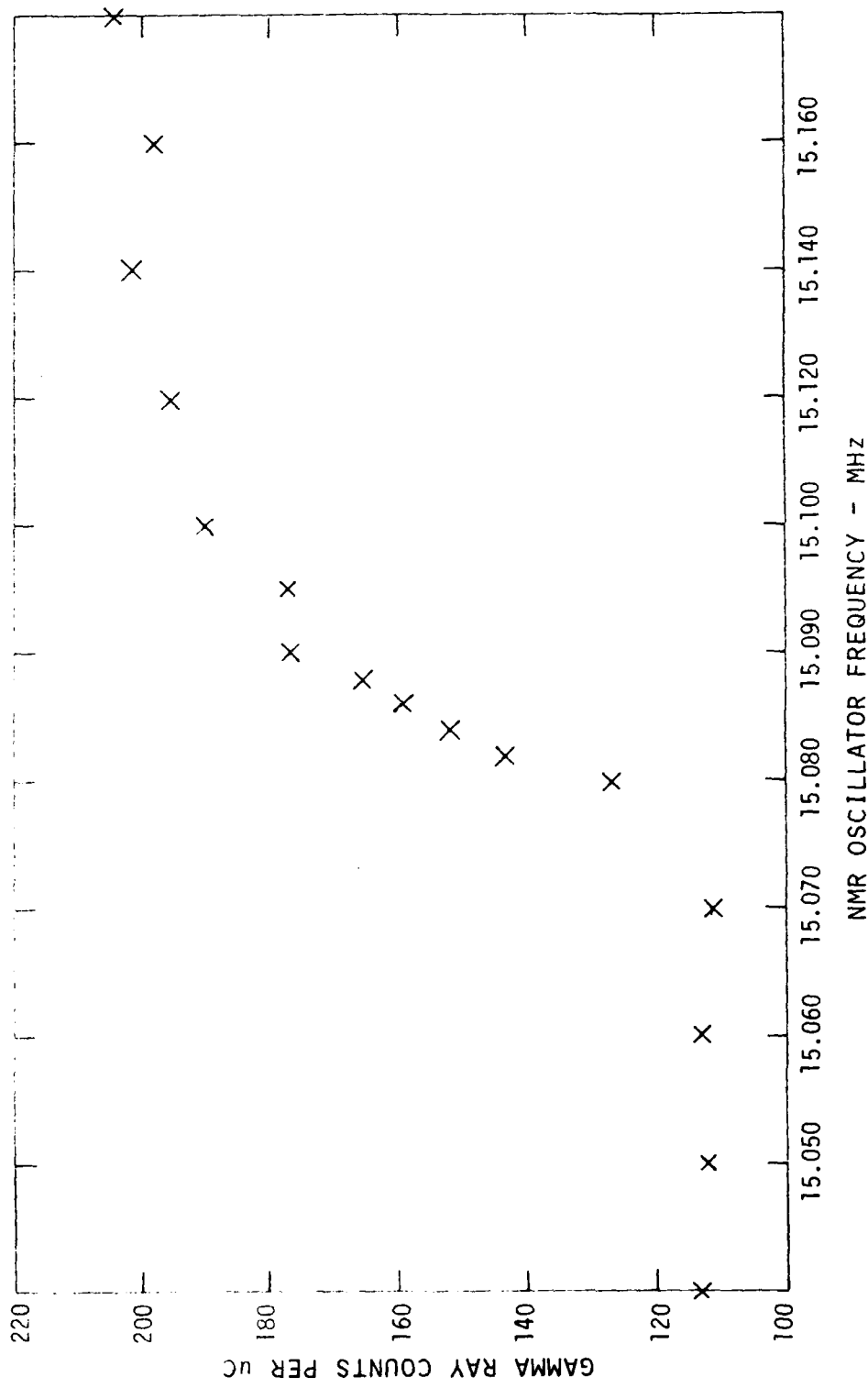


Figure 11. $^{27}\text{Al}(\text{p},\gamma)^{28}\text{Si}$ gamma ray yield curve near 991 keV resonance for thick target.

RESULTS

The thermal treatments given to all the processed samples, and the nuclear resonance profiling data reflecting the resultant changes in the ^{18}O distributions, are summarized in Table II and Figures 12a - 12c. Table II lists the thermal treatments; for each sample it shows the temperature, duration and type of atmosphere employed. It also shows some nuclear profiling results - the yield of alpha particles (per 50 μC of incident protons) recorded at the proton beam energy for which this was maximum. (The significance of this quantity, as well as that of other information in the table, is discussed in the following section.) In addition, a representative set of complete experimental alpha particle yield curves is shown in Figures 12a - 12c. It should be noted that the yield curves are all plotted on a semilogarithmic scale; this was done to facilitate visual cross-comparison as well as to emphasize the importance of the lower-lying points on the wings. Superimposed on the experimental points are theoretical yield curves which were calculated according to a procedure described in the following section.

KEY TO FIGURES 12a, b, c (pp 43, 44, 45)

Observed alpha particle yield curves. All points shown are recorded data for the samples which are identified at left. (Different symbols are used for ease of distinguishing nearby curves.) However, for the lower curves (Samples 606, 827, A824 and 802) the counting time was doubled to obtain sufficient statistical accuracy. The points plotted for those curves are half the recorded counts. The statistical errors (not shown) are the square roots of the observed counts; for the lower curves they should be reduced accordingly. Also shown with each observed curve is a theoretically derived curve (the continuous curve between the data points); these were selected on the basis of best fit, as described in the text.

TABLE 2. SUMMARY OF THERMAL TREATMENTS AND RESULTS

Sample #	THERMAL TREATMENT			PROFILING RESULT		ANALYSIS	
	Temp (°C)	Duration (s)	Atmosphere	Peak Count	Fraction of Ref.	n (by peak frac)	D* (cm²/s)
304	413	71640	air	3800	0.970	1.105	1.23(10) ⁻¹⁷
308	627	22500	air	13674	0.863	1.49	2.1 ⁻¹⁶
309	627	230805	air	6491	0.410	4.85	3.90 ⁻¹⁶
311	788	68521	air	2992	0.473	3.88	8.20(10) ⁻¹⁶
313	789	12600	air	5068	0.801	1.73	6.27(10) ⁻¹⁶
316	706	30630	air	5144	0.665	2.32	5.72(10) ⁻¹⁶
318	707	3540	air	7304	0.965	1.120	2.87(10) ⁻¹⁶
401	563	1799210	N ₂	4882	0.822	1.65	3.79(10) ⁻¹⁸
402	548	619400	N ₂	5155	0.834	1.58	9.66(10) ⁻¹⁸
404	543	244900	N ₂	5634	0.917	1.295	1.11(10) ⁻¹⁷
606	609	8520	steam	3005	0.250	8.10	3.03(10) ⁻¹⁴
612	609	3111	steam	3111	0.541	3.12	1.88(10) ⁻¹⁴
627	1160	11400	N ₂	4346	0.785	1.79	7.73(10) ⁻¹⁶
631	690	230700	HV	10909	1	1	0
631	1150	10980	N ₂	4353	0.812	1.68	6.64(10) ⁻¹⁶
632	815	582240	HV	5087	1	1	0
707	805	7200 (8.9 torr)	H ₂ O	3473	0.721	2.07	1.82(10) ⁻¹⁵
716	828	253800 (0.24 torr)	H ₂ O	10805	0.719	2.08	5.27(10) ⁻¹⁷
717	740	75900 (0.80 torr)	H ₂ O	12781	0.851	1.54	7.22(10) ⁻¹⁷
718	818	16800 (2.65 torr)	H ₂ O	8244	0.865	1.49	2.87(10) ⁻¹⁶

TABLE 2. SUMMARY OF THERMAL TREATMENTS AND RESULTS (contd.)

Sample #	Temp (°C)	Duration (s)	Atmosphere	THERMAL TREATMENT		PROFILING RESULT		ANALYSIS	
				Peak Count	Fraction of Ref.	n (by peak frac)	D* (cm²/s)		
722	842	609000	H ₂ O (0.062 torr)	7621	0.800	1.73	1.30(10) ⁻¹⁷		
726	514	2700	steam	7593	0.812	1.68	2.70(10) ⁻¹⁵		
728	423	5280	steam	7498	0.786	1.79	1.67(10) ⁻¹⁵		
731	331	23640	steam	17589	0.940	1.213	7.80(10) ⁻¹⁷		
734	263	85440	steam	7573	0.794	1.75	9.66(10) ⁻¹⁷		
802	476	22380	steam	5828	0.410	4.80	3.94(10) ⁻¹⁵		
806	476	2775	steam	8899	0.817	1.66	2.53(10) ⁻¹⁵		
807	476	7420	steam	9858	0.706	2.14	1.92(10) ⁻¹⁵		
812	345	25200	steam	11860	0.850	1.61	2.53(10) ⁻¹⁶		
A815	473	7620	steam	12175	0.901	1.35	4.36(10) ⁻¹⁶		
816	473	7620	steam	9108	0.674	2.28	2.20(10) ⁻¹⁵		
A820	475	22770	steam	4905	0.743	1.97	5.06(10) ⁻¹⁶		
823	619	1290	steam	7919	0.569	2.90	2.30(10) ⁻¹⁴		
824	616	16260	steam	5844	0.455	4.12	3.93(10) ⁻¹⁵		
A825	619	1290	steam	11246	0.817	1.66	5.44(10) ⁻¹⁵		
827	616	16260	steam	2419	0.188	11.80	3.40(10) ⁻¹⁴		

NOTE: Prefix "A" signifies prior high-vacuum (HV) anneal: 1 hr @ 900 C.

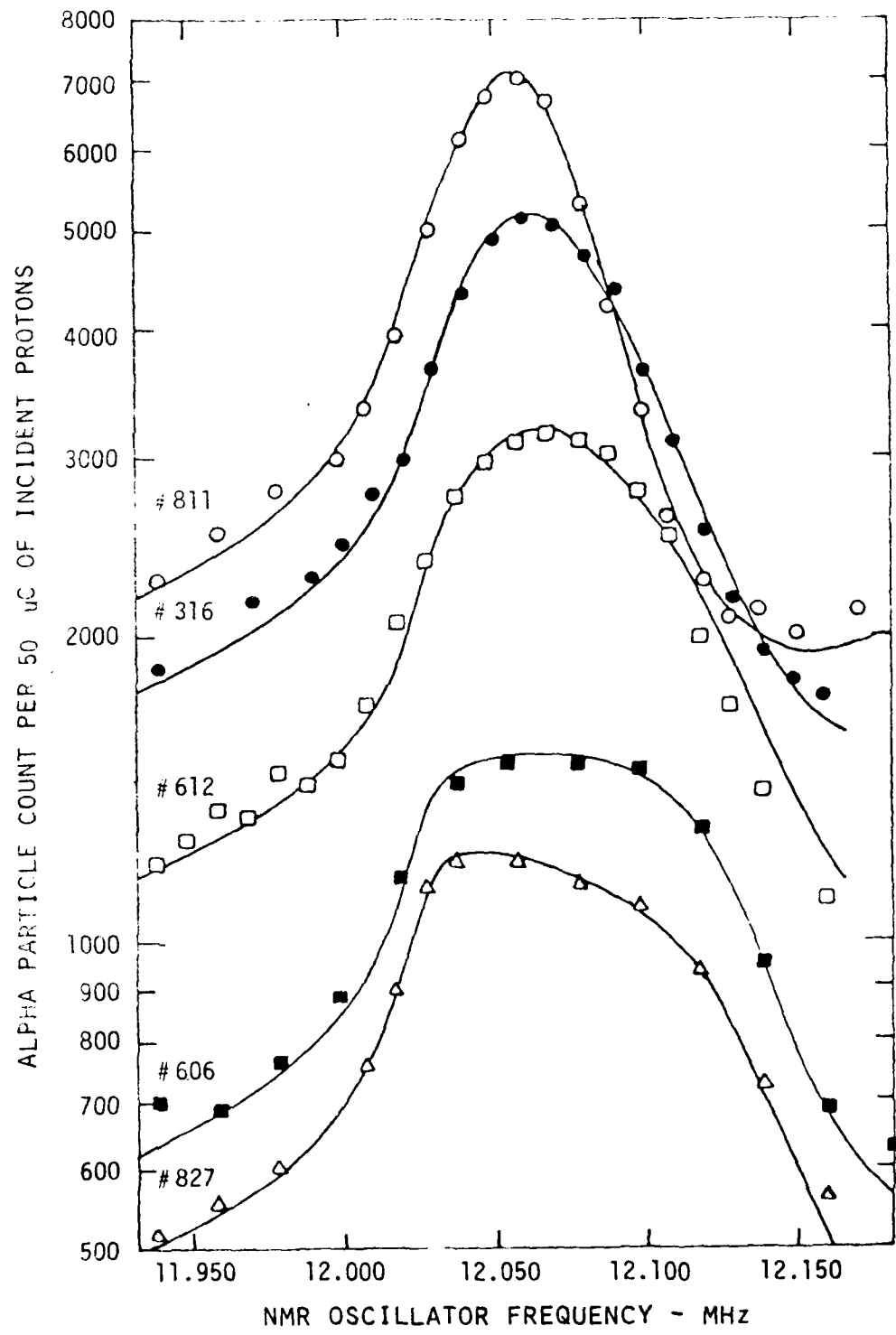


Figure 12a. Observed alpha particle yield curves for selected samples.

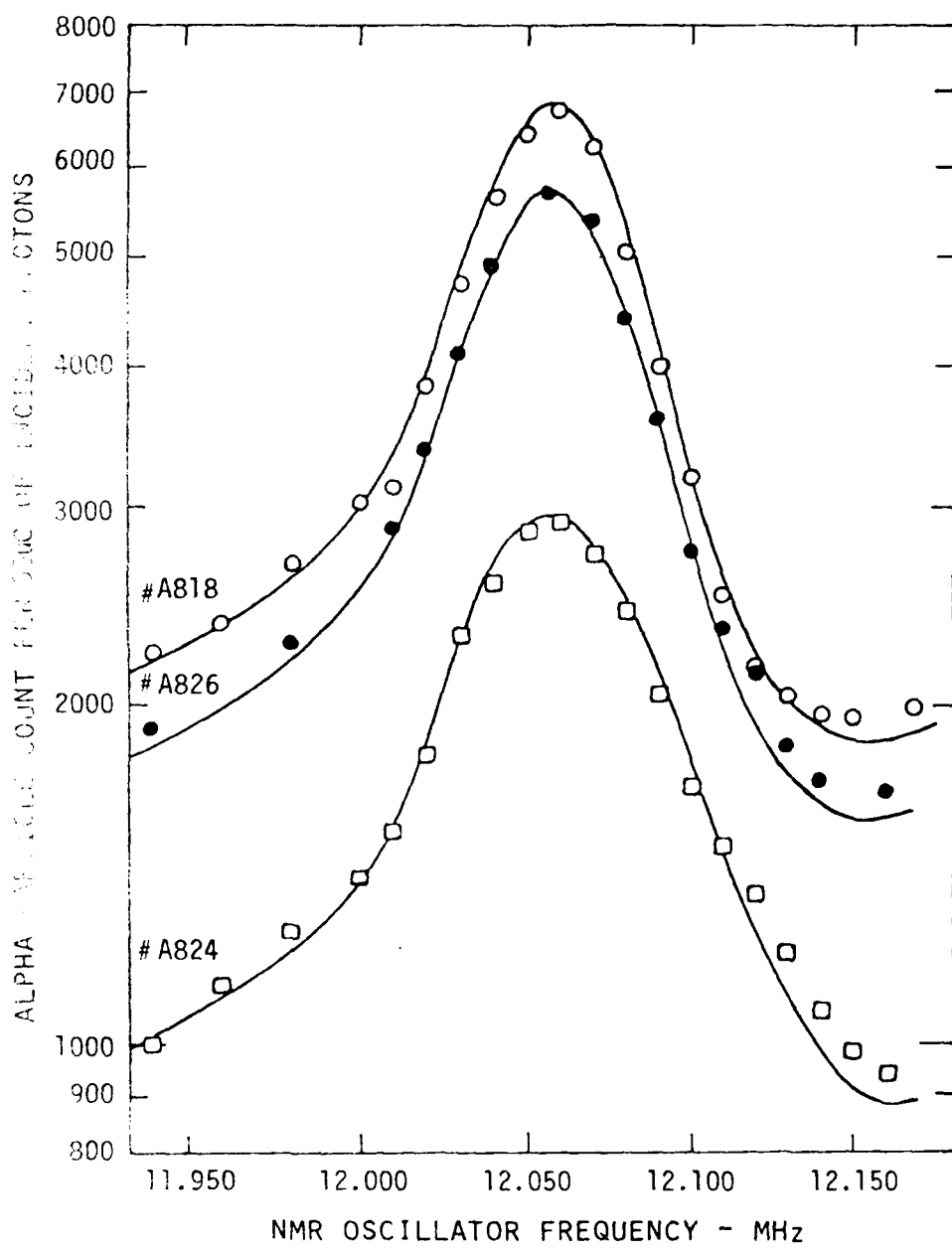


Figure 12b. Observed alpha particle yield curves for annealed samples.

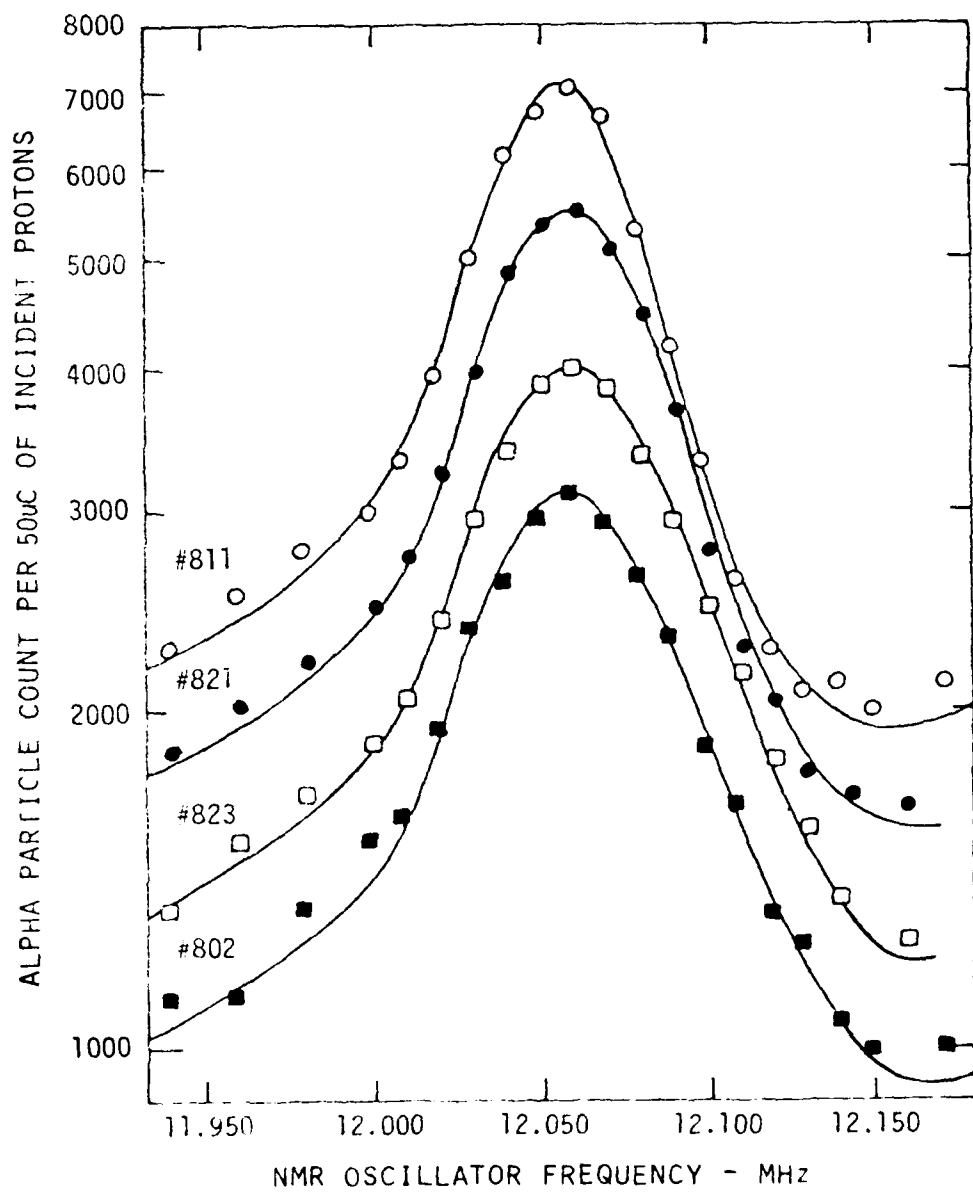


Figure 12c. Observed alpha particle yield curves for low D*t samples.

DATA ANALYSIS

Method of Determining Tracer Diffusivity

The tracer diffusivity D^* was extracted from the data in the context of the water diffusion model discussed in the Introduction. According to this model, the exchange of network oxygen with molecular water dissolved in the glass is solely responsible for any observed change in the distribution of implanted ^{18}O . The dependence of D^* on thermal treatment parameters is a diagnostic of the mechanism of water diffusion in SiO_2 layers and a test of the validity of this model. The extent of change in the distribution is in principle determinable by inversion of the integral equation (14) which gives the particle yield observed by nuclear resonance profiling. In practice, however, this is a complicated procedure entailing large errors whose propagation is difficult to track.

However, once the initial ^{18}O distribution is determined, its subsequent evolution is predictable through macroscopic diffusion theory, provided the properties of the medium are correctly perceived and the appropriate boundary conditions are applied. A full mathematical treatment of the macroscopic diffusion process governing the evolution of an implanted ^{18}O distribution appears in Appendix A. It is shown there that when a sample is maintained for a long time at a fixed temperature, the resulting distribution $\rho(x,t)$ is a function of a single parameter - namely, the product D^*t . The characteristics of the diffusion process are embodied in this parameter. For example, its temperature and pressure dependence reflect the activation energy and identity of the transported species. Its position or time dependence indicate non-uniformities in the medium (see the Discussion). For the case of diffusion, therefore, the problem of determining $\rho(x,t)$ is really that of evaluating

analytically, rather than parametrizing the distribution with D^*t , which has dimension cm^2/sec , a dimensionless parameter was chosen for clarity of presentation. This parameter, denoted n , can be thought of as a natural time unit measuring the extent of diffusion in terms of the amount of broadening resulting from an initial Gaussian distribution. Its applicability to this situation comes from the very close similarity of the implanted ^{18}O concentration to a Gaussian distribution. It is well known that a Gaussian distribution having an initial variance σ_i^2 broadens with time in an infinite homogeneous medium according to the relation

$$2D^*t = \sigma^2(t) - \sigma_i^2$$

where $\sigma^2(t)$ is the variance of the distribution at time t . It can be defined as the ratio $\frac{\sigma^2(t)}{\sigma_i^2}$, i.e., the extent of profile broadening of a Gaussian distribution for the particular case of an infinite homogeneous medium. However, n can be used to index the broadening of a Gaussian implant for any other boundary conditions. The corresponding value of D^*t is then expressed in terms of n according to $2D^*t = (n^2 - 1) \sigma_i^2$ (15)

provided D^* is independent of x and t . For other boundary conditions n loses its meaning as the ratio of widths, but still serves as a single index for the product D^*t .

To determine the proper value of n to be associated with a particular thermal treatment, a set of possible discrete values for n was selected. For each member of this set, a distinct distribution $\rho(x,t)$ was calculated using the method described in Appendix A. Based on this distribution, a predicted alpha particle yield curve $Y(E_b)$ was calculated using the method described in Appendix B. The resulting family of yield curves, parametrized by n , was compared to the experimental yield curve resulting from that thermal treatment. The appropriate value of n was taken as that which indexed the calculated yield curve most closely matching the experimental yield curve. This procedure allowed the extraction of the relevant information on diffusion without resorting to inversion of the integral equation. A representative family of evolved 180 concentration profiles calculated in this manner is shown in Figure 13, while a family of calculated alpha particle yield curves corresponding to these distributions is illustrated in Figure 14.

It should be mentioned that a number of preliminary computations were involved in the calculation of the yield curves. These involved determining the correct values of the constants appearing in the formulas for the reaction cross section, the beam energy spread and the initial 180 distribution in Appendices A and B. Although approximate values of the constants were available from the sources cited there, the final values were determined by finding the best match of the calculated initial yield curve (topmost curve in Figure 14) to the observed yield curve of an implanted but otherwise untreated sample. The goodness of fit can be judged by inspection of the topmost curve in Figure 12a.

In actual practice, the procedure for determining the value of n corresponding to a given thermal treatment consisted of taking an experimental yield curve, comparing it to the family of precalculated yield curves, then running the program with n adjusted to obtain as good a match as possible. Although it was not difficult to determine n with an accuracy sufficient for most thermal energy estimation, the procedure proved unwieldy when higher accuracies were desired, especially for small values of n , when the relative error in D^* arising from errors in n grew very large. As can be seen by differentiating equation (15), the relative error in D^* is

$$\frac{\Delta D^*}{D^*} = \frac{2n^2}{n^2 - 1} \frac{\Delta n}{n}. \quad (16)$$

For large values of n , the relative error in D^* is twice that in n . As n decreases, however, it becomes much larger; for $n < 1.4$ the ratio of relative errors is > 4 . In addition, the shape of the yield curves changed relatively little for small n , making the determination of n difficult.

To overcome these problems, an alternate procedure was adopted for routine measurements of D^* . This procedure, based on the rate of decay of the peak alpha particle yield, proved especially useful in the regime of small n . It can be seen from the family of yield curves in Figure 14 that the peak yield of alpha particles is a monotonically decreasing function of n . (This function is shown in Figure 15.) To determine the value of n using this

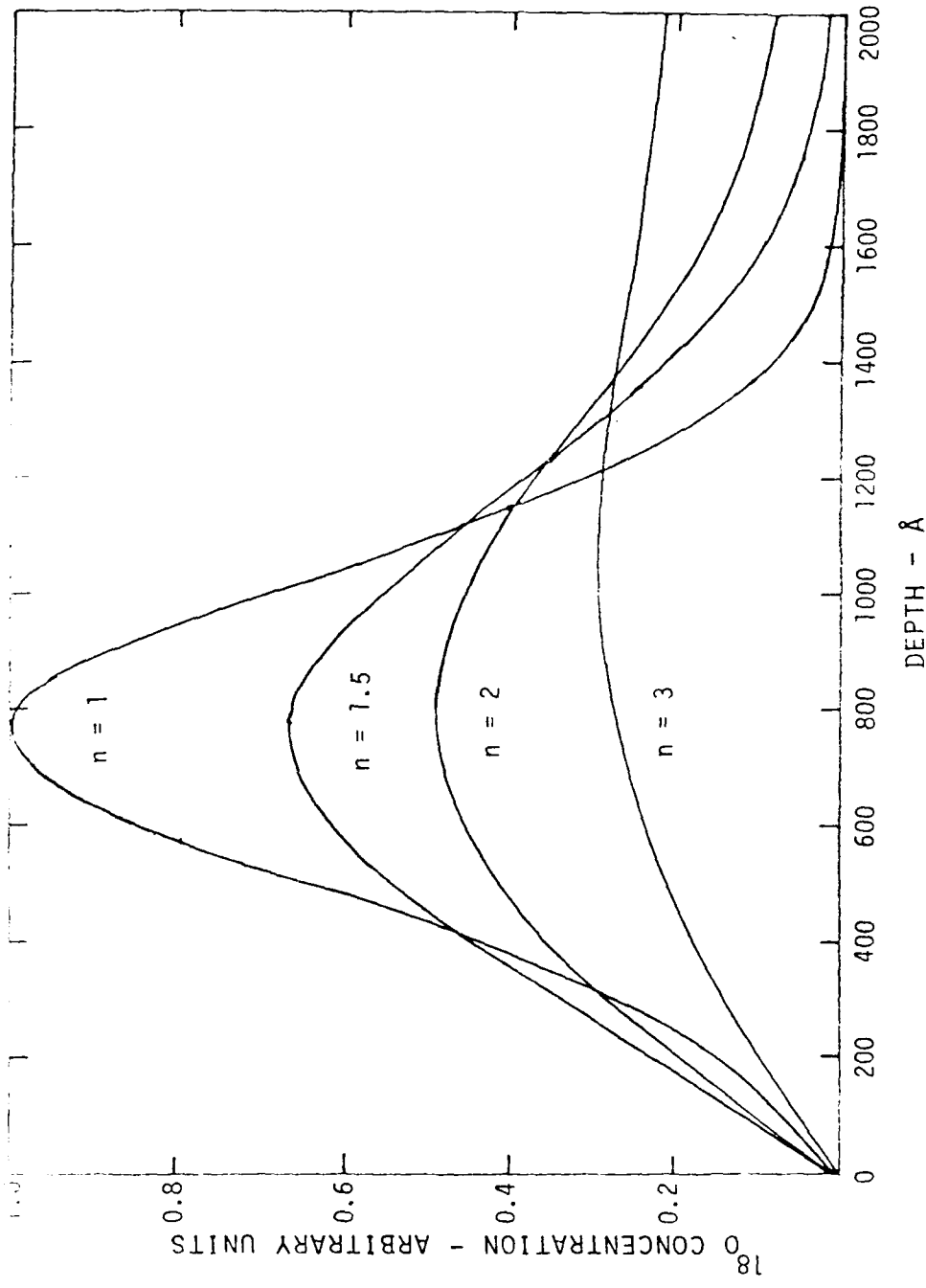


Figure 13. Theoretical ^{18}O concentration profiles in SiO_2 layer after thermal treatments. Value of n reflects extent of treatment. Note inward shift in peak concentration as well as loss of ^{18}O .

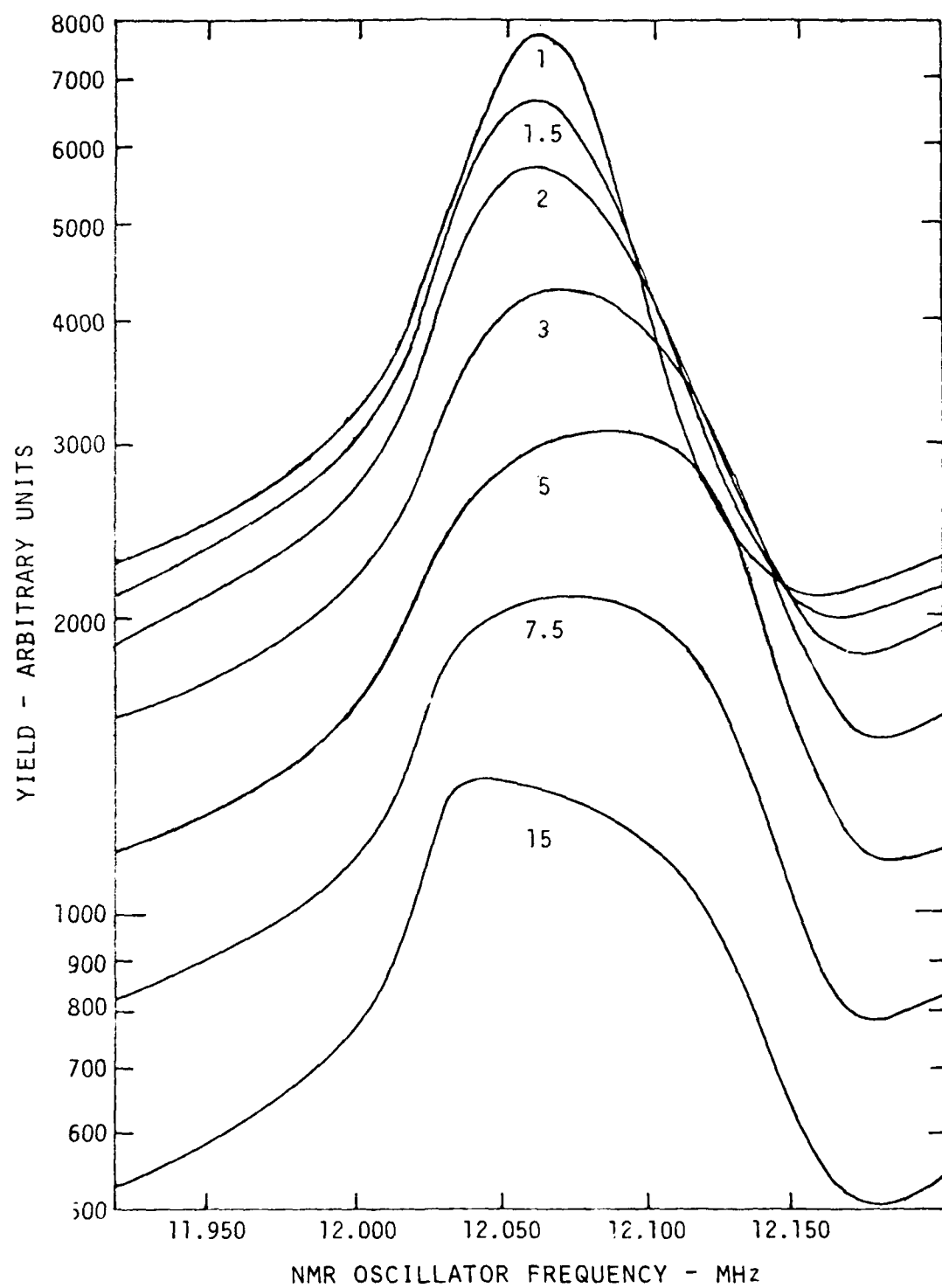


Figure 14. Theoretical alpha particle yield curves (labels indicate n).

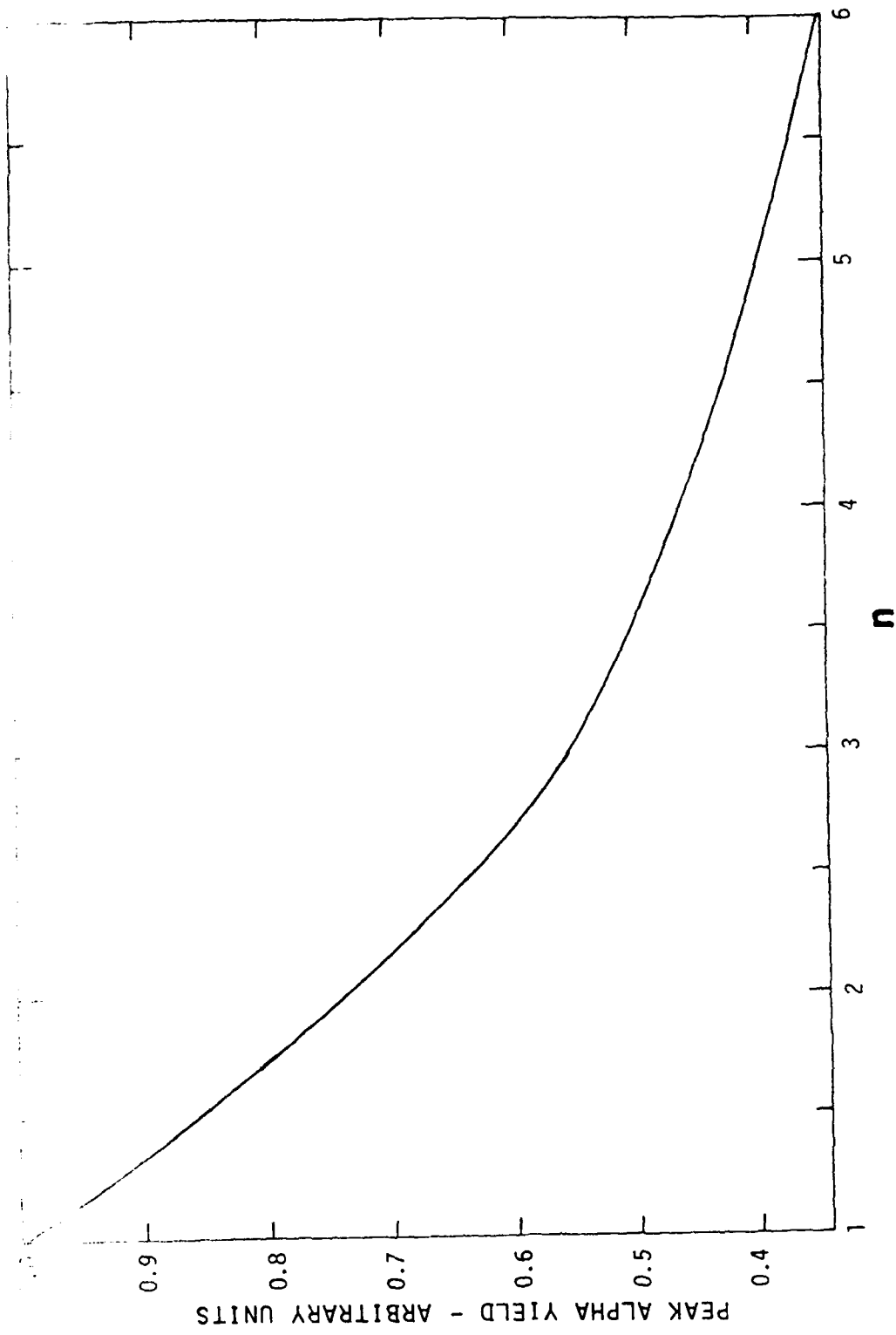


Figure 15. Time behavior of theoretically derived peak alpha yield. This function was calculated by calculating a large number of theoretical alpha particle yield curves. The peak value of each of those curves was tabulated along with the value of n associated with the curve. The figure was gotten by connecting those values with a smooth curve. The variation with time is here expressed as a variation with n , as per the discussion in the text.

function, it was necessary to measure an alpha particle yield curve for a sample only in the vicinity of its peak, so as to determine the peak yield. This quantity was then normalized to that of an implanted but untreated reference sample located nearby on the wafer. The appropriate value of n was then found simply by locating the resulting peak yield ratio on a graph of that function (Figure 15). This procedure had several advantages. First, it greatly shortened the time spent in nuclear profiling. Second, it allowed shorter thermal treatments. This can be seen from Figures 14 and 15. For relatively small n (i.e. short treatments), the shape of the yield curve is insensitive to changes in n , so that comparison of shapes is a poor means of determining n . However, the maximum slope of the peak yield ratio occurs in just that situation, so that its use is most advantageous there. Third, it allowed errors in D^* to be estimated directly.

To demonstrate this, consider the statistical error in D^* obtained by this means for the case of small n . Let the number of alpha particles counted be denoted N and N_0 for the treated and untreated samples, respectively. The peak yield ratio, denoted R , is then

$$R = \frac{N}{N_0}.$$

The statistical error in R is gotten from the statistical errors in N and N_0 taken in quadrature, namely

$$(\Delta R)^2 = \left(\frac{\partial R}{\partial N} \Delta N \right)^2 + \left(\frac{\partial R}{\partial N_0} \Delta N_0 \right)^2. \quad (17)$$

The errors in those quantities are just their square roots. If these are substituted in equation (17), we find that ΔR is given by

$$\Delta R = \sqrt{\frac{R}{N_0}} (1 + R). \quad (18)$$

According to Figure 15, the initial functional dependence of R upon n is approximately

$$R = 1 - \frac{n - 1}{4.1}.$$

This is now differentiated to get Δn in terms of ΔR , which in turn is given by equation (18). By substituting the resulting expression for Δn in equation (16), the relative error in D^* is found to be $\frac{\Delta D^*}{D^*} = \frac{8.2n}{n^2 - 1} \sqrt{\frac{R(1+R)}{N_0}}$. (19)

With $N_0 = 5000$, $\frac{\Delta D^*}{D^*}$ is about 20% for $n=1.5$, decreasing to 10% for $n=2.5$.

The calculation of error propagation can be easily extended to include other sources. For example, lateral nonuniformities in implanted ^{180}Ta dose can be represented by including another term in equation (17). (In this study, the practice of using nearby samples reduced the magnitude of this error to below the level of statistical uncertainty.) Errors in temperature measurement are represented by including (in quadrature) the additional term $E_a \frac{\Delta T}{T}$ in equation (19).

The errors in reading temperature were about 2 C. For the range of temperatures used (610 C to 263 C in steam) this represented a contribution ranging from 5% to 25%.

Temperature and Pressure Dependence of Tracer Diffusivity

The temperature dependence of D^* was determined as follows. First, D^* was calculated from the observed data using the method of peak yield decay described in the previous section. The results of these calculations all appear in the last column of Table II. For each of the three atmospheres (i.e. steam at 1 atm, room air and flowing dry nitrogen) the values of D^* were fit by an equation of the Arrhenius type

$$D^* = D_0^* e\left(\frac{-Q}{RT}\right)$$

with a temperature-independent pre-exponential factor D_0^* . The values of D^* were taken as measured: they were not adjusted for the temperature variation of gas phase concentration. The fit was carried out by the method of unweighted linear least squares using $\frac{1}{T}$ and $\log_{10} D^*$ as the independent and dependent variables, respectively. The results, which appear in Figure 16, along with the individual values of D^* , are

$$D^*_{\text{steam}} = 2.7 (10)^{-10 \pm .40} - \frac{(16.9 \pm 1.3 \text{ kcal/mol})}{RT \text{ cm}^2/\text{s}} \quad (20)$$

$$D^*_{\text{room air}} = 1.3 (10)^{-12 \pm .34} - \frac{(15.5 \pm 1.4 \text{ kcal/mol})}{RT \text{ cm}^2/\text{s}} \quad (21)$$

$$D^*_{\text{dry N}_2} = 1.8 (10)^{-13} - \frac{(15.7 \text{ kcal/mol})}{RT \text{ cm}^2/\text{s}} \quad (22)$$

The indicated errors are derived solely from the variances of the fitting parameters (1), and take no account of the sources of error mentioned in the previous section. The standard deviations in the fits for $\log D^*$ are 0.232 and 0.135 for steam and room air respectively, which imply relative errors of 171% and 136% for D^* . The dry nitrogen data points fell fortuitously close; their error was not calculated. The three fitted lines shown in Figure 16 are almost parallel; at 820°C that representing $D^*_{\text{room air}}$ lies a factor of 93 below D^*_{steam} , while $D^*_{\text{dry N}_2}$ lies a factor of 8.1 below that. Also shown in the figure are values of D^*_{steam} for a few samples that had been vacuum annealed prior to thermal treatment. These values (the square symbols in the figure) lie a factor of 5.0 below those for unannealed samples. The reasons for this will be discussed shortly.

The pressure dependence of D^* was determined by calculating D^* in a similar manner for the samples heated at low pressure (#707, 716, 717, 718 and 722). As these samples had been heated at slightly different temperatures, their values of D^* were converted to a common temperature (of 820°C) by assuming a temperature dependence similar to that seen for steam. The resulting values of D^* (per unit pressure) are displayed in Figure 17. Also shown is D^*_{steam} at 1 atm which was calculated using equation (20). The indicated errors are those arising from counting statistics. The sample (#632) was maintained at 815°C for 579600 s at a pressure of $(10)^{-6}$ torr;

1. W. Mendenhall and R. L Scheaffer, Mathematical Statistics and Applications (Duxbury 1973) pp. 391-393.

no difference could be discerned between the yield obtained from that sample and that from an untreated reference sample: at that pressure, D^* was below the limit of measurement. Another sample (#631) had its alpha particle yield measured twice. After being maintained at 690°C for 230400 s at $(10)^{-6}$ torr, the yield was compared to that of a reference sample: no difference could be detected. It was then maintained for 10980 s at 1150°C in flowing dry nitrogen at 1 atm and the yield was again compared to that of the reference sample. This time the results implied a value of D^* close to that of a sample (#627) which had undergone a similar treatment in dry nitrogen but had no prior vacuum treatment.

The alternate method of determining D^* , comparing the shapes of observed and calculated alpha particle yield curves, is illustrated in Figures 12a-c. Accompanying each observed yield curve in the figures is a calculated curve, a member of the family depicted in Figure 14. The basis for selection was visual judgment rather than numerical computation. A number of points concerning the observations and results must be mentioned. First, the alpha particle counts indicated in the figure are either the actual observations or (for #606, 827, A824 and 802) half the recorded counts. The corresponding statistical errors in the counts are between 1% and 2.5%; as they can be calculated directly, they did not seem worth indicating explicitly. Second, some variation in overall normalization was encountered. This was caused by lateral nonuniformities in implanted dose and by slightly different settings of detector angle on different runs. The maximum variation was on the order of 10%.

The values of n associated with each of the theoretical curves in Figures 12a-c, as well as the resulting estimates for D^* , are listed in Table III. The listed values of D^* for the samples shown in Figure 12a are comparable to those obtained by the method of peak yield decay listed in order of magnitude. The origin of this discrepancy is addressed in the Discussion section which follows.

Figure 16. (Next page) Observed temperature dependence of ^{180}tr tracer diffusivity at 1 atm. The solid lines represent linear least squares fits to the data shown; the resulting pre-exponential factors and activation energies are indicated below.

KEY TO FIGURE

SYMBOL	ATMOSPHERE	D_0^* (cm^2/s)	Q (kcal/mol)
\times	Steam	$2.7(10)^{-10}$	16.9
$+$	Room Air	$1.3(10)^{-12}$	15.5
\circ	Dry N_2	$1.8(10)^{-13}$	15.7

NOTE: \square represents steam measurements of samples that had previously undergone a high-vacuum anneal.

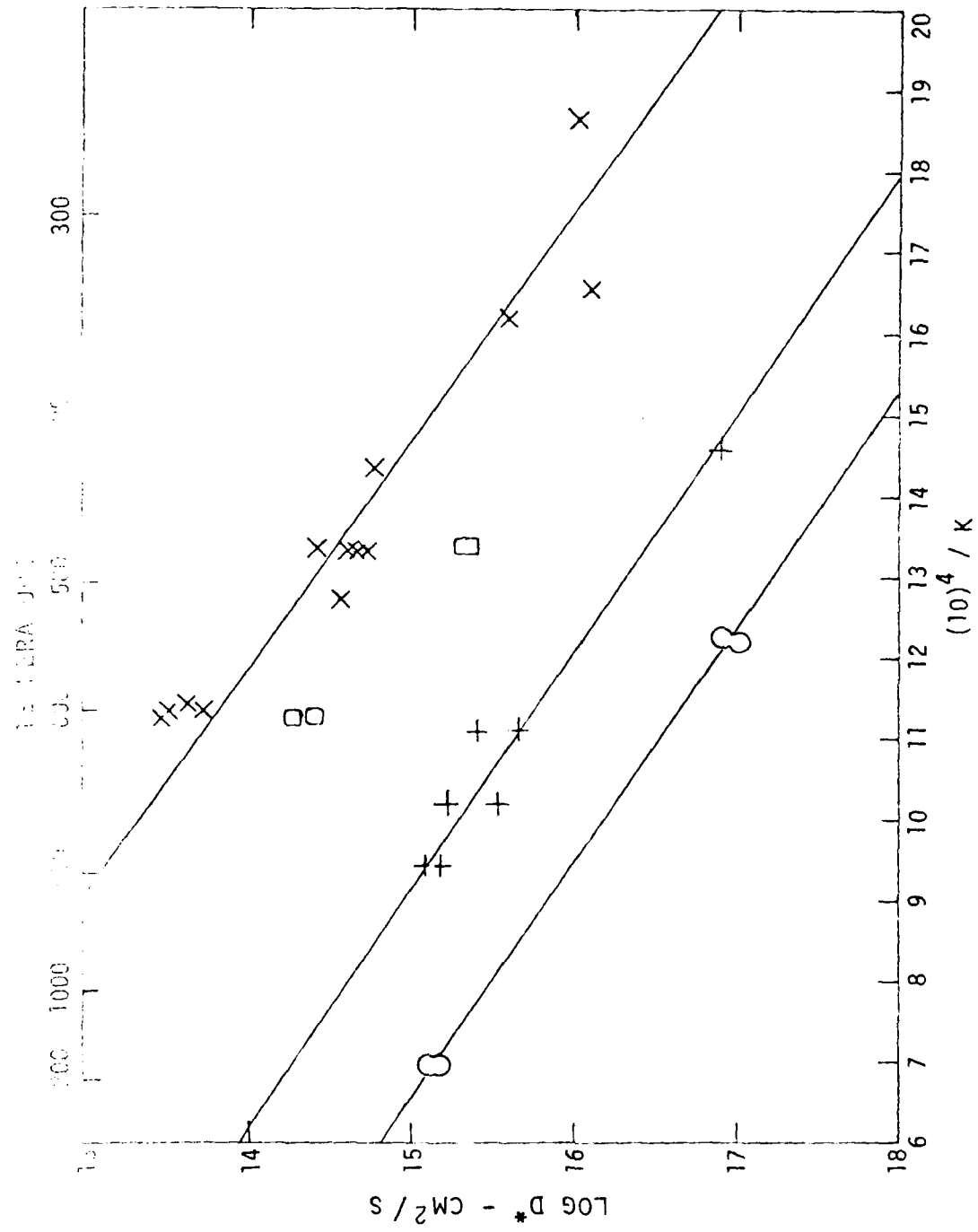


Figure 16. Observed temperature dependence of $^{18}_0$ tracer diffusivity at 1 atm.

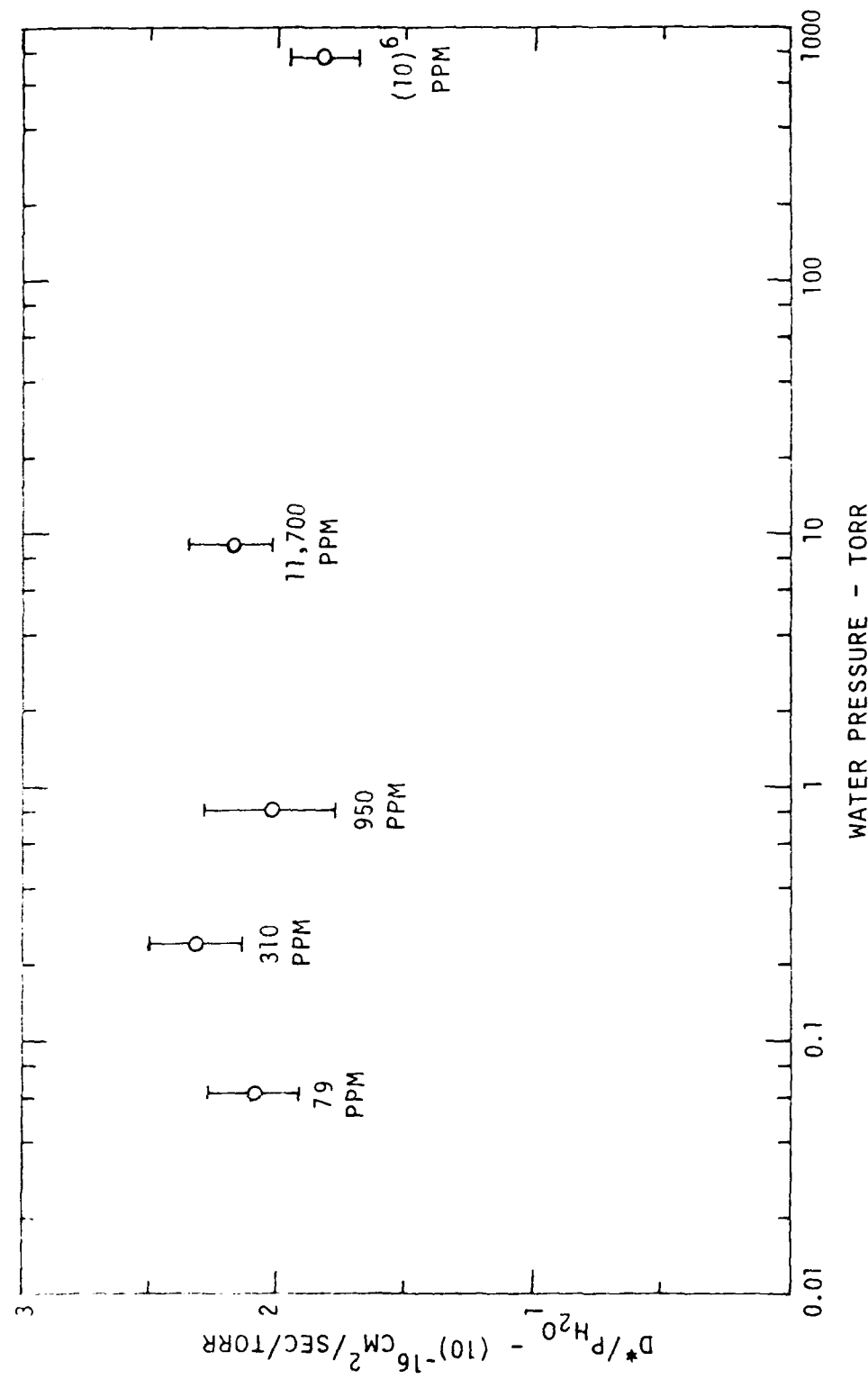


Figure 17. Pressure dependence of tracer diffusivity at 820°C. Labels indicate P in fractions of 1 atm.

TABLE 3. COMPARISON OF METHODS FOR OBTAINING TRACER DIFFUSIVITY

Figure	Sample	YIELD CURVE SHAPE		PEAK YIELD RATIO	
		n	D* (cm^2/s)	n	D* (cm^2/s)
12a	316	1.75	$2.7(10)^{-16}$	2.32	$5.7(10)^{-16}$
	612	2.5	$1.1(10)^{-14}$	3.12	$1.9(10)^{-14}$
	606	15	$5.5(10)^{-14}$	8.1	$3.0(10)^{-14}$
12b	A826	1.08	$5.2(10)^{-16}$	1.66	$5.4(10)^{-15}$
	A824	1.5	$3.1(10)^{-16}$	4.1	$3.9(10)^{-15}$
12c	821	1.2	$2.4(10)^{-16}$	1.69	$1.0(10)^{-15}$
	823	1.5	$3.9(10)^{-15}$	2.9	$2.3(10)^{-14}$
	802	1.5	$2.2(10)^{-16}$	4.8	$3.9(10)^{-15}$

DISCUSSION

Absence of Ion Bombardment Induced Damage in SiO₂ Network

The measurements of tracer diffusivity performed in this study can be compared to others made in SiO₂ films and membranes only if the properties of the material used here match those others. In view of the well-known tendency of ion implantation to induce lattice damage in crystals, it may be suspected that the ¹⁸⁰ implantation altered the structure or properties of the SiO₂ network. However, a good deal of evidence was collected during the course of this study which indicates that the implantation process does not produce enough network damage to appreciably alter the oxide's properties, at least as far as ¹⁸⁰ tracer diffusion is concerned.

First, the amount of ¹⁸⁰ implanted was small enough to avoid gross morphological changes brought about by its incorporation, such as blister or bubble formation. (None were seen.) The additional oxygen implanted in the network amounted to, at most, 1.9% of the normal concentration. This can be seen from equation (A4), which shows the peak concentration of implanted ¹⁸⁰ in the initial distribution to be

$$\rho_{\text{peak}} \approx \frac{1}{G_{\text{imp}}} \sqrt{\frac{1}{2\pi}} \Phi$$

where Φ is the fluence of implanted ¹⁸⁰O₂ ions. As this was $3(10)^{15}$ ions/cm² and G_{imp} was 0.0283 um, ρ_{peak} was $4.2(10)^{20}$ molecules/cm³. This was 1.9% of the concentration of O₂ in SiO₂, which is given in equation (7) as $2.25(10)^{22}$ molecules/cm³.

Second, the shape of every alpha particle yield curve could be well matched to one or another of the set of theoretical curves; these were calculated on the basis of a dilute homogeneous medium. There was, therefore, no indication ever observed of a region of anomalous diffusivity.

Third, similar thermal treatments were performed on two samples, one of which had previously undergone a high-vacuum anneal at 690 C for 230400 s. The ¹⁸⁰ tracer diffusivity was found to be unaffected by this anneal. These observations can be interpreted in the context of previous investigations of annealing of radiation damage in SiO₂ discussed in the Introduction. From these studies it may be concluded that whatever damage is produced in SiO₂ is entirely removed by a suitable high-temperature anneal. It is reasonable to conclude that the thermal treatments performed to induce ¹⁸⁰ diffusion themselves served to anneal out any damage induced by the implantation.

Next, there is the question of whether the proton bombardment involved in the nuclear resonance profiling caused any alteration of the network or induced any diffusion of ¹⁸⁰. To answer this, alpha particle yield curves were collected in implanted but otherwise untreated reference samples both before and after lengthy proton bombardments (about 2000 uC, at a current of 0.5 uA). No difference could be detected.

Finally, to determine whether the implanted ^{18}O actually replaced existing oxygen in the network, or remained interstitial and free to migrate, an alpha particle yield curve was taken for an untreated reference sample after a high-vacuum anneal at 815 °C for 579600 s. If an appreciable amount of implanted ^{18}O had remained mobile, then it would have diffused during that period with a diffusivity which was characteristic of dissolved molecular oxygen at that temperature, namely $(10)^{-9} \text{ cm}^2/\text{s}$ (see Figure 2). The value of the diffusion parameter n corresponding to those values of D^* and t can be calculated using equation (15) to be 3890, implying the escape of virtually all mobile ^{18}O through the oxide surface. However, the observed yield curve was indistinguishable from that of an untreated unannealed reference sample, indicating no shift in the initial ^{18}O concentration profile. Both curves closely matched the theoretically predicted curve for such an implant. This demonstrates that the initial distribution of ^{18}O formed by the implantation is the same as bound network oxygen; an insignificant fraction of it is mobile. This conclusion is in accord with the studies of M. A. Lampert et al. on ^{18}O tracer diffusivity in SiO_2 by Hughes (Johnson et al. 33)) and DiMaria et al. (34) discussed in the introduction. It is also in accord with Primak's (35) theory of bond cleavage by heavy ion energy loss, which predicts bond cleavage by atomic collision involving peak temperatures of 1150 °C affecting a different number of oxygen atoms per ion, on a time scale of $(10)^{-12} \text{ s}$. In the present investigation, the maximum concentration of implanted ^{18}O is less than one percent of oxygen concentration. The subsequent rapid reversion to the state of most complete incorporation of implanted ^{18}O as a constituent of the lattice.

Water Diffusion

As discussed in the previous section, the implantation caused ^{18}O to replace existing oxygen as a constituent of the SiO_2 network. In the absence of water, it was found to be totally immobile at temperatures exceeding 800°C; however, in the presence of water it was observed to move in a manner consistent with its exchange with dissolved molecular water and its subsequent diffusion as a constituent of that species. There are four pieces of evidence to support this conclusion:

(1) The observed linear dependence of the ^{18}O tracer diffusivity upon water vapor phase concentration is identical to that expected for dissolved molecular water. This linear dependence was seen to hold over 4 orders of magnitude (see Figure 17), from 1 atm to 79 ppm (of 1 atm). These measurements were made in pure water vapor - no carrier gases were employed. When room air was used as a carrier gas, the observed tracer diffusivity conformed to this linear dependence, but depended upon the partial pressure of atmospheric water vapor. This can be seen from Figure 16 where the measured ratio

$$\frac{D^*_{\text{steam}}}{D^*_{\text{room air}}} = 93$$

33. N. M. Johnson, W. C. Johnson and M. A. Lampert, *J Appl Phys* 46, 1216 (1975).
34. D. J. DiMaria, D. R. Young, W. R. Hunter and C. M. Serrano, *IBM J Res Devel*, 22, 289 (1978)
35. W. Primak, *J. Appl Phys* 43, 2745 (1972)

is close to the ratio of water vapor partial pressures for these atmospheres, namely 87 (92) assuming room air at 20°C and 50% rel hum. And when the samples were treated in high vacuum, no ^{18}O diffusion could be detected even after 6.7 days at 815°C.

(2) The temperature dependence of D^* _{steam} showed an activation energy of 16.9 ± 1.3 kcal/mol, which is indistinguishable from those observed for water diffusion by all previous investigators (see figures 2, 3, and 16). Previously determined activation energies range from 16 to 18 kcal/mol. This value is clearly inconsistent with those previously observed for oxygen diffusion, the most reliable of which are about 28 kcal/mol.

(3) The magnitude of D^* is close to that expected for free exchange between network oxygen and dissolved water. In the presence of free exchange, D^* is related to D_{eff} , the experimentally measured diffusivity of water, according to equation (10) by

$$\left(\frac{D^*}{D_{\text{eff}}}\right)_{\text{free exchange}} = \begin{cases} 15(16)^{-4} & 600^\circ\text{C} \\ 7.5(10)^{-4} & 1200^\circ\text{C} \end{cases} .$$

This ratio, whose value is derived from the water solubility measurements of Moulson and Roberts (54), can also be evaluated by using the results of D^* _{steam} obtained in this study (see Figure 1b). This is

$$\frac{D^*_{\text{steam}} (\text{this work})}{D_{\text{eff}} (\text{Moulson-Roberts})} = \begin{cases} 6.0(10)^{-4} & 600^\circ\text{C} \\ 4.4(19)^{-4} & 1200^\circ\text{C} \end{cases} .$$

The magnitude of D^* _{steam} is thus seen to be consistent with free exchange at both temperatures measured by Moulson and Roberts to within a factor of 2-3, which is within the limits of accuracy obtained for the D^* measurements in this study.

(4) In the presence of atmospheric oxygen, the activation energy for D^* _{room air} remained that of water (roughly 16 kcal/mol, as indicated in equation 21), rather than reverting to that of oxygen (28 kcal/mol). This was true even at 800°C, where D_{O_2} exceeds $(D_{\text{eff}})\text{H}_2\text{O}$ by an order of magnitude, and even though the concentration of atmospheric oxygen was 17 times that of water vapor (20% of 760 torr vs. 50% of 18 torr). This implied the absence of exchange between atmospheric and network oxygen, in agreement with similar recent findings by Rosencher et al. (50). As discussed in the Introduction, these authors observed the failure of diffusing $^{18}\text{O}_2$ to replace existing network ^{16}O during thermal growth of oxide films on silicon in dry ^{18}O atmospheres.

- 92. R. C. Weast, Handbook of Chemistry and Physics, 55th ed (CRC Press, 1974) p. D-159
- 54. J. Moulson and J. P. Roberts, Trans Faraday Soc 57, 1208 (1961)
- 50. E. Rosencher, A. Straboni, S. Rigo and G. Amsel, Appl Phys Lett 34, 254 (1979)

Water Permeation Kinetics

The values of D^* which appear in Figure 16, although conforming closely enough to an Arrhenius relation to support the conclusions reached in the previous section, nonetheless show a significant amount of scatter. This is evident from the large standard deviations to the fits of equations (20) and (21), which are 5 times larger than would be expected on the basis of the discussion of equation (19). The scatter in the D^* values appears to be systematic rather than random: the smallest values of D^* tend to be associated with the shortest thermal treatments (i.e. small values of η) as well as the performance of a high-vacuum anneal prior to thermal treatment (see Table 1). Further, the amount of yield curve broadening in these cases is anomalously small compared to the decay in peak yield (see Figures 11a-11c). These observations suggest that a previously unsuspected effect systematically altered the values of D^* . The explanation for the spread of D^* values is complicated by the uncontrolled quantity of reacted water initially present in the oxide.

When an initially dry oxide layer is placed in an atmosphere of ^{18}O , some ^{18}O water vapor, molecular water enters the oxide rapidly (see Figure 19), ($\sim 10^9$) and distributes itself within the layer so that its concentration rapidly attains its saturation value. At the outset of this study, it was believed that equilibrium between dissolved molecular water and reacted water in the network is also quickly established, so that the reacted water concentration so rapidly attains its saturation value. However, if the approach to equilibrium is not rapid and the oxide layer is initially dry, there will be a delay observed in ^{18}O diffusion until the reacted water which is necessary for its transport has reached a significant level. The anomalously small values observed here after short thermal treatments and vacuum desiccation, especially for the lower temperature steam treatments, suggest that these conditions occur.

In order to properly assess the effects of nonequilibrium permeation conditions on the evolution of ^{18}O distributions, a thorough theoretical and experimental study is needed. Although a complete study is beyond the scope of this work, an introductory development appears here in Appendix D, where the partial differential equations governing ^{18}O diffusion (a formidable set of five coupled nonlinear equations) are presented. They are solved here only for two special cases, both of which involve rapid saturation of the oxide with dissolved molecular water. One of them, involving rapid establishment of equilibrium, is the case which was thoroughly treated in the body of this study. For the other case, the content of reacted water remains uniform throughout the oxide but varies with time. For times on the order of a characteristic time τ it is far lower than its saturation value, causing the observed initial depression in D^* .

It is interesting that this same phenomenon seems to have been observed by both Williams(53) and Haul and Dumbgen(51) in their early studies of ^{18}O permeation in SiO_2 fibers and membranes. As discussed in the Introduction,

8. R. H. Doremus, Glass Science (Wiley, 1973) p. 128
53. E. L. Williams, J Am Ceram Soc 48, 190 (1965)
51. R. Haul and G. Dumbgen, Z Electrochem 66, 636 (1962)

these authors employed mass spectrometers to measure atmospheric oxygen isotopic ratios in containers with limited amounts of ^{18}O -enriched oxygen. Williams, observing that the values of diffusivity at short times were much lower than those evaluated at long times, particularly for low-temperature diffusions, invoked this effect to account for the very high activation energies found earlier by Haul and Dumbgen and by Sucov (52), whose observations all involved short times. By not carrying out long enough diffusions, they observed erroneously small D values at lower temperatures, leading to an overestimate of the activation energy. The activation energy he found (29 kcal/mol) was close to that measured by Norton (49) as well as to the thermal oxidation B values for dry oxygen. The magnitudes of the diffusivity measured in the early ^{18}O permeation experiments, however, were on the order of those measured in this study rather than those of Norton and the thermal oxidation experiments. This suggests that they were observing some sort of exchange of diffusing ^{18}O with network oxygen. Both Meek (94) and Schaeffer and Muehlenbachs (95) explained the six order of magnitude difference on the basis of a direct exchange. However, in view of the lack of exchange observed both by Rosenthaler et al (50) and in this study for ^{18}O diffusion in dry SiO_2 films, their explanations must be doubted. If any exchange occurs, it is more likely mediated by reacted water in the oxide. It is certainly the case that significant quantities of water were present in Williams' experiment, both in the oxides and in the atmosphere. He studied its influence on his ^{18}O diffusivity by vacuum desiccation of the SiO_2 , and found that this procedure both increased the initial delay and lowered the limiting value of the diffusivity. The influence of water was apparently not appreciated by the other early investigators, who seem not to have taken pains either to eliminate or control it. The actual mechanism of exchange (if it exists) between diffusing molecular oxygen and reacted water remains obscure; and the process has not been observed in thermal oxidation experiments which have involved oxygen atmospheres containing controlled fractions of water vapor. The parabolic coefficients measured both by Deal et al (67) and by Ota and Butler (71) are consistent with independent diffusion of water and oxygen over a range of atmospheric water concentrations from 2% to 100% by volume. This conflicts with the observation of Irene and Ghez (40), that atmospheric water concentrations as low as 25 ppm (in O_2) markedly increased the parabolic coefficient.

50. E. Rosenthaler, A. Straboni, S. Rigo and G. Amsel, *Appl Phys Lett* 32, 254 (1978)
52. E. W. Sucov, *J Am Ceram Soc* 46, 14 (1963)
49. F. J. Norton, *Nature* 191, 701 (1961)
94. R. L. Meek, *J Am Ceram Soc* 56, 342 (1973)
95. H. A. Schaeffer and K. Muehlenbachs, *J Matls Sci* 13, 1146 (1978)
67. B. E. Deal, D. W. Hess, J. P. Plummer and C. P. Ho, *J Electrochem Soc* 125, 339 (1978)
71. Y. Ota and S. R. Butler, *J Electrochem Soc* 121, 1107 (1974)
40. E. A. Irene and R. Ghez, *J Electrochem Soc* 124, 1757 (1977)

The analysis of these authors yielded systematically different values of B from those of other investigators (see Figure 3, particularly their values of B_{O_2} at 780 C and of $B_{\text{H}_2\text{O}}$ at 893 C). In addition, the dependence of their parabolic coefficients upon the crystallographic orientation of the Si substrate suggests a nonstandard definition of B , which is normally taken to involve pure bulk diffusion rather than interface effects. It may be noted that although Deal et al. (67) also report a large increase in B with the addition of trace amounts of H_2O based on data plotted in their Figure 3, a replotting of that figure with $(B_{\text{observed}} - B_{\text{O}_2})$ replacing B_{observed} as ordinate (plotted against volume % H_2O in O_2) shows this quantity to depend strictly linearly upon water concentration, as was found in this study. Figure 18 here shows their data plotted in such a manner, with the ordinate shown as percent of B in pure water vapor in order to compensate for the temperature dependence of $B_{\text{H}_2\text{O}}$. The linear dependence is evident.

Another example of the strong influence that water exerts on diffusion in SiO_2 occurs when silicon wafers are thermally oxidized in resistance-heated furnaces. The evolution of water from the walls of the silica diffusion tubes caused a great deal of variation in early results on thermal oxidation kinetics, as was noted by Revesz and Evans (62). These authors eliminated the wall contribution by rf heating their samples in a cool-walled furnace. Subsequent investigators, realizing the significance of this effect, employed various means to inhibit water vapor evolution. For example, Mayo and Evans (5) used polysilicon diffusion tubes: the film of SiO_2 which formed on the inner wall acted to getter any water vapor present in the atmosphere. The extent to which silica furnace walls contribute to atmospheric water vapor content can be seen from the work of Nakayama and Collins (69), who measured oxidation rates for silicon in dry argon corresponding to water vapor pressures of 0.22 torr at 850 C and 0.35 torr at 1000 C. The same effect can be seen from the values of $D^*_{\text{dry N}_2}$ observed in this study. These were consistently a factor of only 8 below those of $D^*_{\text{room air}}$ as mentioned in the Data Analysis, corresponding to water vapor pressures of about 1 torr. Backstreaming of room air through the open exhaust end of the diffusion tube may also have contributed to the large value of $D^*_{\text{dry N}_2}$. As no quantitative differences were drawn from that data, this possibility was not investigated further.

- 67. B. E. Deal, D. W. Hess, J. D. Plummer and C. P. Ho, *J Electrochem Soc* 125, 339 (1978)
- 68. A. G. Revesz and R. J. Evans, *J Phys Chem Solids*, 30, 551 (1969)
- 69. S. Mayo and W. H. Evans, "Development of Hydrogen and Hydroxyl Contamination in Thin Silicon Dioxide Films" NBSIR 78-1558 (NBS, March 1979)
- 70. T. Nakayama and F. C. Collins, *J Electrochem Soc* 113, 706 (1966)

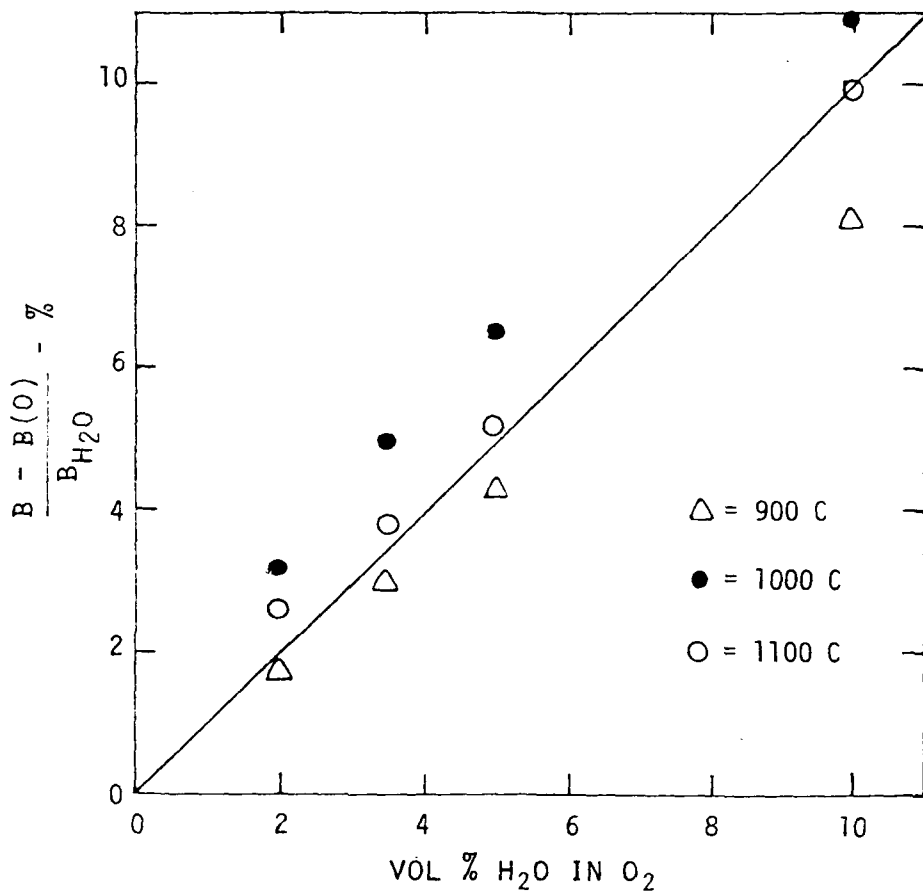


Figure 18. Increment in the parabolic rate constant upon addition of H_2O to oxygen atmosphere, as percent of B_{H_2O} in pure water vapor. All data points are from Deal et al. (67); values of B_{H_2O} in pure water vapor (used for normalization) are from Deal and Grove (56), adjusted to 100 vol % water vapor.

67. B. E. Deal, D. W. Hess, J. D. Plummer and C. P. Ho, *J Electrochem Soc* 125, 339 (1978)
 56. B. E. Deal and A. S. Grove, *J Appl Phys* 36, 3770 (1965)

An independent confirmation of the time variation in ^{18}O tracer diffusivity resulting from nonequilibrium permeation conditions has recently been provided by Rigo et al.(96). Using procedures similar to that of Rosencher et al.(50), they measured the permeation of ^{18}O into SiO_2 films upon thermal treatment in H_2^{18}O atmospheres. They found that the ^{18}O profiles were consistent with a time-varying D^* , especially for temperatures near those employed in this study.

94. E. Rosencher, A. Straboni, S. Rigo and G. Amsel, *Appl Phys Lett* 34 254 (1979)
95. S. Rigo, F. Rochet and A. Straboni, "An ^{18}O Study of the Oxygen Exchange in SiO_2 Films During Thermal Treatment in Water Vapor," Presentation, 1980 International Conference on the Physics of MOS Insulators, Raleigh, NC 17-20 June 1980.

CONCLUSIONS

The results of the 180 tracer diffusion measurements performed in this study clearly demonstrate that water diffusion in SiO_2 films proceeds by the transport of molecular water and that it is accompanied by a strong reversible reaction between molecular water and network oxygen. The observed linear dependence of tracer diffusivity upon partial pressure of atmospheric water vapor, for pressures ranging from 1 atm to as little as 0.06 torr, indicates that network oxygen is exchanged with molecular water. The activation energy of tracer diffusion remained about 16 kcal/mol, characteristic of water diffusion, over a range of temperatures from 1150 C to 260 C. Further, the magnitude of the tracer diffusivity was consistent with the presence of free exchange between network oxygen and diffusing water. The extent of tracer diffusion proved to be unaffected by the presence of atmospheric oxygen, indicating the absence of exchange with that species. The results obtained here agreed with corresponding results obtained by most other investigators using different means. They are in complete agreement with recently proposed models of oxygen and water diffusion in SiO_2 , in which the diffusion proceeds by transport of the molecular species through interstices in the network without any direct reaction between the molecular species and the SiO_2 . (The strong exchange reaction accompanying water diffusion is mediated by immobile OH groups which are dissociation products of the molecular water.)

The process employed for introducing tracer 180 into the network, that of ion implantation, was shown to produce a region within the oxide in which the 180 was fully incorporated in the network: no 180 diffusion was observed in high vacuum, even after 161 hrs at 815 C. The properties of the network remained otherwise unaltered, at least as far as diffusion was concerned. This was demonstrated both by the data's close match to theoretical predictions based on a dilute homogeneous medium as well as by the absence of any effect on diffusion of a high-temperature treatment which was sufficient to anneal out any implantation-induced damage. These findings indicate that the thermal treatments performed to induce 180 diffusion were themselves sufficient to anneal out any damage.

The technique of nuclear resonance profiling proved to be a convenient, nondestructive and sensitive method of measuring 180 diffusivities as low as $1(10)^{-17} \text{ cm}^2/\text{s}$ at temperatures as low as 260 C.

In addition to supporting the above conclusions concerning the mechanical water diffusion in SiO_2 , the measurements made in this study provided evidence indicating that chemical equilibrium between water dissolved in SiO_2 films and its reaction products often had not been attained over the time spans of the thermal treatments. The time variation of the reacted water concentration, leading to a time variation in 180 tracer diffusivity, suggests a series of 180 diffusion measurements which would form a natural follow-up to this study. Thermal oxide films could be grown on a set of silicon samples in dry oxygen, each of which would contain a thin layer enriched with 180 (formed either by a short oxidation in 180 or by a low-energy implant). Although the total thicknesses and the enriched-layer thicknesses would all be identical, the depth of the enriched layer would be different for different samples. After the set of samples received a thermal treatment in water vapor, the concentration profile of reacted water in the oxide could

be determined by measurement of D^* near each enriched layer by nuclear resonance profiling. Successive concentration profiles could be determined from a series of thermal treatments, providing a complete experimental determination of nonequilibrium water permeation kinetics.

Such a study could be of great benefit in the manufacture of future high-reliability integrated circuit devices. The absorption of moisture is known to seriously degrade the breakdown resistance of MOS gate oxides, leading to premature device failure. Detailed observations of permeation kinetics would be a valuable tool in the investigation of new methods to inhibit water permeation in oxide films.

ACKNOWLEDGMENTS

The author wishes to express sincere gratitude to Dr. S. Kronenberg and Mr. J. Kohn for their persistent encouragement and support, to Dr. G. Brucker and Mr. F. Kolondra of RCA Labs, Princeton for performing the ion implantation, to Mr. E. Ahlstrom for preparing the thermal oxides, and to Mr. A. Hager and Mr. J. Freeman for glass and thermocouple fabrication; particularly to his colleagues, Dr. H. Berkowitz, for his advice on theoretical physics and on programming, and Dr. R. Lux for his invaluable and generously provided cooperation both in the nuclear profiling and in many discussions of physical mechanisms.

APPENDIX A - Evolution of ^{18}O Distribution

Suppose an SiO_2 layer containing implanted ^{18}O is heated for a time t under conditions which produce a tracer diffusivity D^* which is independent of x and t , where x is depth in the layer. Then the distribution of excess ^{18}O in the oxide (i.e., in excess of the natural background level of 0.02% isotopic fraction) will change with time so as to satisfy the diffusion equation

$$\dot{\rho}(x,t) = D^* \frac{\partial^2 \rho(x,t)}{\partial x^2} \quad (\text{A1})$$

under boundary conditions appropriate for the experimental case. The general solution to this equation is

$$\rho(x,t) = A_0 + B_0 x + \sum_n e^{-\alpha_n^2 D^* t} [A_n \cos \alpha_n x + B_n \sin \alpha_n x]. \quad (\text{A2})$$

Remember that ^{18}O is transported only as a constituent of molecularly dissolved water. The boundary conditions are therefore determined by considering the behavior of this substance at the boundaries:

(a.) At the oxide surface, equilibrium between the outside atmosphere and water dissolved in the oxide occurs rapidly: surface absorption and reactions are not involved (1). This implies the condition $\rho(0,t) = 0$.

(b) At the oxide-silicon interface, the boundary condition is temperature dependent. This can be seen from the analysis of steady-state steam oxidation performed by Deal and Grove (2). (Steady-state means $\nabla \cdot J = 0$ within the oxide). According to their equations (6) and (7), the ratio of molecularly dissolved water concentration at the interface to that at the outer surface is given by

$$\frac{c_i}{c_o} = \frac{1}{1 + k x_o / D_{eff}} \quad (\text{A3})$$

where k , the interface rate constant, is determined through observations of the linear and parabolic rate constants A and B and the equilibrium solubility C^* (x_o is the layer thickness.) Deal and Grove give a value of

$$k = 1.8 (10)^3 \text{ um/hr}$$

at 1000 C with an activation energy of 45.3 kcal/mol. Using this in conjunction with Moulson & Roberts' (3) equation

$$D_{eff} = (10)^{-6} \exp (-18.3(\text{kcal/mol})/RT) \text{ (cm}^2/\text{sec}),$$

A-1. R. H. Doremus, Glass Science (Wiley, 1973), p. 128

A-2. B. E. Deal and A. S. Grove, J Appl Phys 36, 3770 (1965)

A-3. J. Moulson and J. P. Roberts, Trans Faraday Soc 57, 1208 (1961)

the temperature dependence of $\frac{C_i}{C_o}$ is seen to be the following:

T(C)	kx_o/D_{eff}	C_i/C_o
250	$3.1(10)^{-7}$	1
475	$7.7(10)^{-4}$	1
600	0.011	0.989
1000	1.4	0.417
1200	5.9	0.145 .

At the temperatures encountered in this work, the ratio $\frac{C_i}{C_o}$ is more than 98%. The no-flux boundary condition is therefore

$$\frac{\partial}{\partial x} \rho(x_o, t) = 0.$$

(c) For sufficiently long times all the excess $^{18}_0$ will eventually disappear, either through surface leakage or interface incorporation of diffusing molecular weight, implying the condition $\rho(x, \infty) = 0$.

(d) The initial distribution was taken to be that implantation profile given by Gibbons, et al (4) for the appropriate experimental conditions. This was an Edgeworth distribution (the product of a Gaussian and a polynomial); explicitly, it is

$$\rho(x, 0) = \frac{\text{Fluence}}{2\pi \sigma_{imp}} e^{-\frac{\xi^2}{2}} \left[1 + \frac{\sqrt{\beta_1}}{6} (\xi^3 - 3\xi) + \frac{5\beta_1}{72} (\xi^4 - 6\xi^2 + 3) + \frac{\sqrt{\beta_1}}{72} (\xi^6 - 15\xi^4 + 45\xi^2 - 15) \right] \quad (A4)$$

where

$$\xi = \frac{x - x_{imp}}{\sigma_{imp}}$$

$$x_{imp} = 0.0768 \text{ mm}$$

$$\sigma_{imp} = 0.0283 \text{ mm}$$

$$\sqrt{\beta_1} = -0.164 .$$

A-4. J. F. Gibbons, W. S. Johnson and S. W. Mylroie, Projected Range Statistics, 2nd Edn. (Academic, 1975)

Conditions (a), (b), and (c) imply

$$A_0 = B_0 = A_n = 0 \quad (\text{all } n)$$

$$B_n = 0 \quad (n \text{ even})$$

$$\alpha_n = \frac{n\pi}{2x_0}$$

The solution to the diffusion equation is then straightforward, being

$$\rho(x, t) = \sum_{n=1}^{\infty} B_{2n-1} e^{\left[-\left(\frac{2n-1}{2}\frac{\pi}{x_0}\right)^2 D*t\right]} \sin\left(\frac{2n-1}{2}\frac{\pi}{x_0} x\right) \quad (A5)$$

with

$$B_k = 2 \int_0^l dx \sin\left(\frac{k\pi}{2} x\right) \rho(x, 0) . \quad (A6)$$

The numerical evaluation of $\rho(x, t)$ was performed with an Interdata 832 Computer located at Fort Monmouth, N.J. The programs were straightforward. Representative results appear in Figure 13.

APPENDIX B - Evolution of Alpha Particle Yield

The yield of alpha particles from the $^{18}\text{O}(\text{p}, \alpha)^{15}\text{N}$ reaction is given by the integral equation

$$Y(E_b) = \int_0^{x_0} dx \rho(x, t) \int_0^{\infty} dE_i g(E_b, E_i) \int_0^{E_i} dE \frac{d\sigma}{dE}(E) f(E, E_i, x) \quad (\text{B1})$$

where

E_b is the mean energy of the incident proton beam,

E is the energy of reacting protons,

E_i is the actual energy of protons incident on the surface of the layer,

x_0 is the thickness of the oxide layer,

x is the depth at which the reaction occurs,

$\rho(x, t)$ is the ^{18}O concentration profile (i.e. atoms per unit volume at depth x at time t),

$\frac{d\sigma}{dE}$ is the differential cross section of the $^{18}\text{O}(\text{p}, \alpha)^{15}\text{N}$ reaction,

$g(E_b, E_i)dE_i$ is the fraction of protons in the beam which have an incident energy between E_i and $E_i + dE_i$,

$f(E, E_i, x)dE$ is the probability that a proton which has started with energy E_i and arrived at depth x will have an energy between E and $E + dE$.

This also appears in the Introduction as equation (14). Once the functions $\rho(x, t)$, $g(E_b, E_i)$, $f(E, E_i, x)$ and $\frac{d\sigma}{dE}(E)$ are established, then the yield is obtained by integration. A means of calculating ρ is given in Appendix A. For the remaining functions, we proceed as follows:

$g(E_b, E_i)$:

The distribution of energies in the incident beam was found experimentally through analysis of the thick-target $^{27}\text{Al}(\text{p}, \gamma)^{28}\text{Si}$ excitation curve (see Procedure). As the energy spread amounted to less than 1 keV, the details of its shape are relatively unimportant; for ease in calculation it can be taken to be a Gaussian with $\sigma_b \approx 1$ keV, i.e.,

$$g(E_b, E_i) = \frac{1}{\sqrt{2\pi}\sigma_b} e^{-\frac{(E_b-E_i)^2}{2\sigma_b^2}} \quad (\text{B2})$$

$f(E, E_i, x)$:

If the proton energy loss were strictly deterministic, then f would be given by $\delta(E - \{E_i - \int_0^x dx' \frac{dE}{dx'}\})$, where $\frac{dE}{dx'}$ is the specific energy loss of protons in SiO_2 . At an E_b of 629 keV the value of $\frac{dE}{dx'}$ is 61 keV/ μm (1). Since the layer is only 0.2 μm thick, the protons lose 12.2 keV in a complete traversal; throughout this region $\frac{dE}{dx'}$ is constant to within 1%. Thus

$$\int_0^x dx' \frac{dE}{dx'} \approx \langle \frac{dE}{dx'} \rangle x \equiv \epsilon x .$$

However, the random nature of the independent scattering events by which protons lose energy in materials implies that their energy at a given projected range is not uniquely determined by their initial energy. The effect of this energy straggling is to broaden the delta function to a distribution $f(x, \Delta)$, where x is the projected pathlength and $\Delta = E_i - E(x)$. Vavilov (2) found that this function may be closely approximated by one of three expressions, the choice depending on the magnitude of x . (A review of Vavilov's work appears in Appendix C.) Upon performing detailed calculations based on that work, it was found that for the particular conditions of this experiment, the distribution could be approximated by

$$f(x, \Delta) = \frac{1}{\sqrt{2\pi} k_s x} e^{-\left[\frac{(\Delta - \epsilon x)^2}{2k_s x}\right]} \quad (B3)$$

where $k_s = 17.75 \text{ (keV}^2 \text{ um}^{-1}\text{)}$

$\frac{d\sigma}{d\Omega}(E)$:

Highly accurate measurements of the differential cross section for the $^{18}\text{O}(p, \alpha)^{15}\text{N}$ reaction at $\theta_{\text{lab}} = 150^\circ$ have recently been performed by Amsel, Maurel and Nadai (3).

B-1 E. Bonderup and P. Hvelplund, Phys Rev A4, 562 (1971)

B-2 P. V. Vavilov, Soviet Phys JETP 5, 749 (1957)

B-3 J. W. Mayer and E. Rimini, Eds., Ion Beam Handbook for Materials Analysis (Academic, 1977) p 163

A very close fit to their data in the region of the 629 keV resonance has been found to be a sum of two interfering Lorentzians plus an exponential background. Explicitly, this was

$$\frac{d\sigma}{d\Omega}(E) = \frac{\frac{1}{4} \left(\frac{\sigma_{res}^2}{4} (12.78 - K) - (E - E_{res}) \right) e^{\frac{E-E_{res}}{4.7}}}{{(E-E_{res})^2 + \frac{\sigma_{res}^2}{4}}} + K e^{\frac{E-E_{res}}{58}} \text{ (mb/ste)} \quad (B4)$$

where

$$K = \begin{cases} 2 & (E < E_{res}) \\ 1.75 & (E \geq E_{res}) \end{cases}$$

$$\sigma_{res} = 1.9 \text{ keV}$$

$$E_{res} = 629 \text{ keV}$$

With all the constituents of the yield established, its evaluation was carried out numerically by first substituting equations (B2) and (B3) in equation (B1). Because of the strong damping of the exponential function $f(x, \Delta)$ in the range of x where $\rho(x, t)$ was appreciable, the limits on the E integral could be extended to $\pm\infty$ without significantly changing the result. Similarly, the strong damping of the exponential function $g(E_b, E_i)$ allowed the lower limit on the E_i integral to be extended to $-\infty$. The order of integration was then interchanged, enabling the yield to be written

$$Y(E_b) = \int_0^{x_0} dx \rho(x, t) \int_{-\infty}^{\infty} dE \frac{d\sigma}{d\Omega}(E) \int_{-\infty}^{\infty} dE_i \left[4\pi \sigma_b \sqrt{k_s x} \right]^{-1} \exp \left\{ - \left[\frac{(E_i - E_b)^2}{2\sigma_b^2} + \frac{(E_i - [E + Ex])^2}{2k_s x} \right] \right\}. \quad (B5)$$

The E_i integral could then be performed using the convolution identity

$$\int_{-\infty}^{\infty} dt e^{-\frac{t^2}{\sigma_1^2}} e^{-\frac{(s-t)^2}{\sigma_2^2}} = \sqrt{\frac{\sigma_1 \sigma_2 \sqrt{\pi}}{\sigma_1^2 + \sigma_2^2}} e^{-\frac{s^2}{\sigma_1^2 + \sigma_2^2}} \quad (B6)$$

with

$$t \equiv E_i - E_b, S = E - E_b + \epsilon x, c_1 = \sqrt{2} c_b, c_2 = \sqrt{2 k_s x}.$$

The yield is

$$Y(E_b) = \int_0^{x_0} dx \frac{\rho(x, t)}{\sqrt{2\pi(c_b^2 + k_s x)}} \int_{-\infty}^{\infty} dE \frac{dc}{d\Omega}(E) e^{-\frac{(E-E_b+\epsilon x)^2}{2(c_b^2 + k_s x)}}. \quad (B7)$$

Using the substitution $E' = \frac{E - (E_b - \epsilon x)}{\sqrt{2(c_b^2 + k_s x)}}$, this was rewritten as

$$Y(E_b) = \frac{1}{\sqrt{\pi}} \int_0^{x_0} dx \rho(x, t) \int_{-\infty}^{\infty} dE' e^{-E'^2} \frac{dc}{d\Omega}(E' \sqrt{2(c_b^2 + k_s x)} + E_b - \epsilon x). \quad (B8)$$

This was the appropriate form for evaluation by Hermite integration (4):

$$\int_{-\infty}^{+\infty} dE' e^{-E'^2} f(E') \approx \sum_{j=-J}^J w_j f(E'_j).$$

The evaluation of equation (B8) was performed using the weight factors and abscissas appropriate for a 20-point Hermite integration over E' with $\frac{dc}{d\Omega}$ given by equation (B4), and a 50-point Simpson integration over x , with $\rho(x, t)$ given by the sum of equation (A5) plus a constant background. A listing of the program appears on the next three pages; it was run on an Interdata 832 computer located at Fort Monmouth, N.J. Representative results appear in Figure 13.

```

1      BTEST
2      C EVOLUTION OF ALPHA YIELD FROM IMPLANTED D18
3      C NOTE: APPEND B IS THE DOD FOURIER COEFFICIENT ONLY
4      FOR SHULLIAN
5      C      IMPLANT WITH RIMPE=.0763, SIGIMPE=.0283, DM
6      C      REAL X=NT
7      C      DIMENSION DUMMYY(2),OUT(40)
8      C      COMMON /COM1/NN,PI,PMHS,RIMPE,SIGIMPE,FREQD,CTRAN,
9      C      II,DECK,EPRF,SIGEL,FF,RF,CIGFIT,
10     C      SIGBM,12,R,11,100,M,100,B,500
11     C      COMMON /COM2/IBAM,EBEAM,DT
12     C      WRITE(0,101)
13     C      CALL FREEFM(0,2,DUMMYY)
14     C      PBKD=DUMMYY(1),
15     C      SIGBM=DUMMYY(2)
16     C      IF (PBKD.LT.0.) GO TO 30
17     C      IBZ=SIGBM+SIGBM
18     C      10  WRITE(0,102)
19     C      CALL FREEFM(0,2,DUMMYY)
20     C      NT=DUMMYY(1)
21     C      DB=DUMMYY(2)
22     C      IF (INT.LT.1) GO TO 5
23     C      DT=(NT+NT-1)*SIGIMPE+SIGIMPE/2
24     C      WRITE(0,104)
25     C      DO 20 IBEAM=1,40
26     C      FREQ=.01*IBEAM+11.840
27     C      EBEAM=.4327*FREQ*FREQ
28     C      OUT(IBEAM)=CIMP(0,0.0001,PMHS,500)/DB
29     C      CONTINUE
30     C      WRITE(0,103) OUT
31     C      GO TO 10
32     101  FORMAT(1X,'ENTER PBKD, SIGBM')
33     102  FORMAT(1X,'ENTER N FOR T(N),NORM,FACTOR')
34     103  FORMAT(1X,5G12.4)
35     104  FORMAT(1X,'ALPHA YIELD FOR NMR FREQ = 11.850
36     C      THRU 12.240 MHZ')
37     30   END
38
39     BTEST
40     FUNCTION EYF(F)
41     C      COMMON /COM1/NN,PI,PMHS,RIMPE,SIGIMPE,FREQD,CTRAN,
42     C      II,DECK,EPRF,SIGEL,FF,RF,CIGFIT,
43     C      SIGBM,12,R,11,100,M,100,B,500
44     C      COMMON /COM2/IBAM,EBEAM,DT
45     C      F=0.
46     C      DO 10 N=1,15
47     C      HRS=(2*PI/11.850)*PI*PMHS
48     C      IF ((HRS*EPRF*II).LT.100.) GO TO 10
49     C      EYF=(CIMP(F,FREQ)+F*(DT+HRS*EPRF))/EYF+FF
50     10  CONTINUE
51     EYF=F+EYF*DT*CTRAN/2.50E-024

```

```

49      RETURN
50      END
51      *TEST
52      FUNCTION F(X)
53      REAL X
54      COMMON /COM1/ NN, PI, PMAX, PIMP, SIGIME, PRFD, CTRHS,
55      1  II, DEIX, EREC, GRES, KK, RR, SIGFIT,
56      1  SIGEM, DE, R, X(100), W(100), B(50)
57      COMMON /COM2/ CB, EBERM, DT
58      REAL INTJ
59      F=EEHM-DEIX+R-EREc
60      RR=DT*(2.*CB+CTRHS+RD)
61      INTJ=0.
62      DO 10 J=-II, II
63      IF(J.EQ.0) GO TO 10
64      XJ=X(IABS(J))
65      IF(XJ.LT.0) XJ=-XJ
66      DE=RR*XJ+CC
67      KK=2.
68      IF(DE.GT.0.) KK=1.75
69      XSEC=(RR*RR*(12.78-KK)-DE*R*EXP(DE*116))/(
70      1  (DE*DE+RR*RR)+KK*KK*EXP(DE*58))
71      INTJ=INTJ+IABS(J)*XSEC
72  10  CONTINUE
73      F=INTJ*12.74/13.26*1.77245385*EMF(X)
74      RETURN
75      END
76      *TEST
77      REAL FUNCTION SIMP(XMIN, XMAX, NFT)
78      N=NFT-1
79      D=(XMAX-XMIN)/2./N
80      X=XMIN
81      Y=F(X)
82      TEMF=Y
83      DO 100 I=1, N
84      DE MF=TEMF+Y+4.*F(XD+D)
85      DE MF=DE MF+2.*F(XD+2.*D)
86      DE MF=DE MF+2.*F(XD+3.*D)
87      DE MF=TEMF+Y
88      100 1 CONTINUE
89      RETURN
90      END
91      *TEST
92      REAL F, DEI
93      REAL KK
94      COMMON /COM1/ NN, PI, PMAX, PIMP, SIGIME, PRFD, CTRHS,
95      1  II, DEIX, EREc, GRES, KK, RR, SIGFIT,
96      1  SIGEM, DE, R, X(100), W(100), B(50)

```

DATA E

1 0.7453407083009, 0.733473705454, 1.2340769153953,
1 1.7485377121168, 2.2543240020893, 2.7880060584281,
1 3.34738545873312, 3.9447841401156, 4.6036824495107,
1 4.23748088900112

DATA M

1 4.68243669600E-1, 2.17675105348E-1, 1.080172001113E-1,
1 1.481174000240E-2, 3.744171341200E-3, 2.636170300734E-4,
1 1.016158420530E-5, 1.00061015320738E-7, 4.22340932111E-10,
1 1.000000000000E-13

DATA L

1 5.005004416400, 7.00000000000000, 0.791622388440,
1 1.576362001870, 1.034491001920, 0.170570121330,
1 0.171644117177, 0.1634630818824, 0.012498884477,
1 0.161644115154, 0.1618318451928, 0.016162990711,
1 0.161644115154, 0.1614718108677, 0.013929360528,
1 0.161644115154, 0.01670814145, 0.012201714002,
1 0.161644115154, 0.0111177483121, 0.010693587861,
1 0.161644115154, 0.1609502200394, 0.009532532789,
1 0.161644115154, 0.16000546853262, 0.009532532789,
1 0.161644115154, 0.007984152942, 0.009532532789,
1 0.161644115154, 0.0072881473745, 0.009532532789,
1 0.161644115154, 0.006880314085, 0.009532532789,
1 0.161644115154, 0.006180162367, 0.009532532789,
1 0.161644115154, 0.0057135000033, 0.009532532789,
1 0.161644115154, 0.0053050610113, 0.009532532789,
1 0.161644115154, 0.0050012814052, 0.009532532789,
1 0.161644115154, 0.0047271156162

CARD 1785, PI, 02, PMAX,

SIMP, SIGIMP, EPES, GRES, DEIMX,

IF, IR, RR, SIGFIT,

II, NH

17.75, 0.141598653, 1.414216562, 0.6,

0.02614, 0.0263, 828., 1.8, 61.0,

1., 4.7, 0.95, 4.5,

500.

APPENDIX C - Proton Energy Straggling Distribution

If a proton with initial energy E_i passes through a medium, its energy E decreases by an amount $\Delta = E_i - E(x)$ where x is the projected pathlength. Because of the random nature of the independent scattering events by which protons lose energy in materials, the proton energy at a given projected pathlength is not a unique function of E_i . Rather, the proton energy loss is characterized by a distribution $f(x, \Delta)$. $f(x, \Delta) d\Delta$ is the probability that a proton traversing a path of length x will suffer an energy loss between Δ and $\Delta + d\Delta$. This distribution was studied by Vavilov (1), who found that it is closely approximated by one of three expressions, the choice depending on the magnitude of x . (The equations given by Vavilov will be denoted herein by the prefix "V".)

For $x \geq 1 \text{ um}$, the expression for $f(x, \Delta)$ given in equation (V15) is equivalent to

$$f(x, \Delta) = \frac{1}{\sqrt{2\pi} k_s x} \exp \left[- \frac{(\Delta - Ex)^2}{2k_s x} \right] \quad (\text{C1})$$

with

$$k_s x = \Omega_B^2 = 4\pi z Z e^4 N x$$

where Ω_B = Bohr straggling parameter (Bohr (2) as quoted by Fano (3))

z = proton atomic number

Z = SiO_2 atomic number

e = charge of the electron

N = number density of SiO_2 atoms

For $1000 \text{ \AA} \leq x \leq 1 \text{ um}$, $f(x, \Delta)$ is given in equation (V13) as

$$f(x, \Delta) = \frac{1}{\tau \sqrt{\pi}} e^{(at - \frac{a^3}{3})} A(t) \cdot \quad (\text{C2})$$

This expression can be evaluated as follows:

According to the conventional notation of special relativity, the protons' velocity (relative to the speed of light) is

$$\beta^2 = \frac{2E}{Mc^2} \quad (\text{C3})$$

C-1. P. V. Vavilov, Soviet Phys JETP 5, 749 (1957)

C-2. N. Bohr, Mat. Fys. Medd. Dan. Vid. Selsk 18 (8) (1948)

C-3. U. Fano, Ann Rev Nucl Sci. 13, 1 (1963)

where M = proton mass and E = proton energy. From equation (V5) we have

$$\mathcal{E}_{\max} = \frac{2m_e c^2 \beta^2}{1 - \beta^2} \xrightarrow{\text{small } \beta} \frac{4m_e c^2}{M c^2} E = \frac{4}{1836} E \quad (C4)$$

where m_e = electron mass.

And also from equation (V5)

$$\xi = 0.300 \times \frac{m_e c^2}{\beta^2} \frac{z}{A} = 0.075 \times \frac{m_e c^2 M c^2}{E} \quad (C5)$$

where x = depth within layer, in g/cm^2 , and $z/A = 1/2$.

From between (V5) and (V6), and using equations (C4) and (C5), we have

$$\kappa = \frac{\xi}{\mathcal{E}_{\max}} = 34.43 \times \frac{m_e c^2 M c^2}{E^2} \quad (C6)$$

From equation (V12), and using equation (C6)

$$a = \left(1 - \frac{\beta^2}{2}\right) \left[\frac{2\kappa}{(1-2/3\beta^2)^2} \right]^{1/3} \xrightarrow{\text{small } \beta} [2\kappa]^{1/3} = 4.099 \left[\frac{x m_e c^2 M c^2}{E^2} \right]^{1/3}. \quad (C7)$$

Also from equation (V12), and using equations (C5) and (C7)

$$\eta = \xi \left[\frac{(1 - \frac{2}{3}\beta^2)}{(2\kappa)^2} \right]^{1/3} \xrightarrow{\text{small } \beta} \frac{\xi}{a^2} = 0.004464 \left[\frac{x m_e c^2 M c^2 E}{E^2} \right]^{1/3}. \quad (C8)$$

Expressing x in um, with $\rho = 2.27 \text{ g}/\text{cm}^3$ for SiO_2 (4) and approximating E by $E_{\text{res}} = 629 \text{ keV}$, we have

$$\xi = 0.01298 x \quad (\text{MeV}) \quad (C9)$$

$$\kappa = 9.472 x \quad (\text{dimensionless}) \quad (C10)$$

$$a = 2.666 x^{1/3} \quad (\text{dimensionless}) \quad (C11)$$

$$\text{and } \eta = 1.826 x^{1/3} \quad (\text{keV}) \quad (C12)$$

Using equations (C11) and (C12) and $\epsilon = 61 \text{ keV/um}$ (5) in equation (V12), we have

$$t = \frac{(\Delta - \epsilon x)}{\eta} + a^2 . \quad (C13)$$

The distribution given in equation (V13) can then be written as

$$f(x, \Delta) = \frac{0.309}{x^{1/3}} \exp(1.46\Delta - 96.43x) \text{Ai}\left(\frac{\Delta - 61}{1.826x^{1/3}} + 7.108x^{2/3}\right) \quad (C14)$$

where Ai is the Airy function (6).

The following give an excellent fit to all values of Ai(x) listed in Table 10.11 of Reference 6:

$$\text{Ai}(x) \cong \begin{cases} |x|^{-1/4} (0.3975 \cos \xi + 0.4003 \sin \xi), & (x \leq -2.5) \\ 0.35503 \left(1 + \frac{1}{6} x^3 + \frac{4}{720} x^6 + \frac{28}{362880} x^9\right) - \\ 0.25882 \left(x + \frac{2}{24} x^4 + \frac{10}{5040} x^7 + \frac{80}{3628800} x^{10}\right), & (-2.5 < x \leq 1) \\ \frac{1}{2} x^{1/4} e^{-\xi} \left[0.00481 \left(1.5 - \frac{1}{\xi}\right)^2 + 0.01756 \left(1.5 - \frac{1}{\xi}\right) + 0.52703\right], & (1 < x) \end{cases} \quad (C15)$$

where $\xi = \frac{2}{3} |x|^{3/2}$.

For $x \lesssim 1000 \text{ \AA}$, $f(x, \Delta)$ is given by equation (V16):

$$f(x, \Delta) = \frac{1}{\pi \xi} \kappa e^{\kappa(1+\beta^2 c)} \int_0^\infty dy e^{\kappa f_1} \cos(y \lambda_1 + \kappa f_2) \quad (C16)$$

C-5. E. Bonderup and P. Hvelplund, Phys Rev A4, 562 (1971)

C-6. A. Abramowitz and I. A. Stegun, Handbook of Mathematical Functions, 446 (US Government Printing Office, 1964)

where

$c = 0.577....$ (Euler's constant)

$$f_1 = \beta^2 [\ln y - Ci(y)] - \cos y - y Si(y)$$

$$f_2 = y [\ln y - Ci(y)] + \sin y + \beta^2 Si(y)$$

$$\lambda_1 = K\lambda + K \ln \kappa$$

$$\lambda = \frac{\Delta - EX}{\xi} - 1 - \beta^2 + c - \ln \kappa$$

and where Ci and Si are the cosine and sine integral functions respectively.

Although later calculations of $f(x, \Delta)$ exist (see, for example Bichsel and Saxon (7) and references cited therein), recent straggling experiments involving 0-2 MeV protons in thin films of silicon (8) have confirmed the validity of Vavilov's expressions.

C-7. H. Bichsel and P. Saxon, Phys Rev A11, 1286 (1975)

C-8. J. Baglin, private communication (1979)

APPENDIX D - Nonequilibrium Permeation Kinetics

To fully describe the evolution of the tracer ^{18}O distribution in the SiO_2 films, it must be realized that ^{18}O can be a constituent of either dissolved molecular water, reacted water or network oxide. Let the respective concentrations of the various species be denoted

$$\begin{cases} \rho_d(x,t) \equiv [\text{H}_2^{16}\text{O}] & \text{(dissolved water)} \\ \rho_d^*(x,t) \equiv [\text{H}_2^{18}\text{O}] \end{cases}$$

$$\begin{cases} \rho_r(x,t) \equiv [\text{Si}^{16}\text{OH}] & \text{(reacted water)} \\ \rho_r^*(x,t) \equiv [\text{Si}^{18}\text{OH}] \end{cases}$$

$$\begin{cases} \rho_n(x,t) \equiv [\text{Si}^{16}\text{O}_2] & \text{(network oxide)} \\ \rho_n^*(x,t) \equiv [\text{Si}^{18}\text{O}-^{16}\text{O}] . \end{cases}$$

(The stars indicate the presence of tracer ^{18}O .) We may assume that

- a. the amount of ^{18}O is everywhere small compared to the amount of ^{16}O , and thus neglect any terms involving $\rho^*\rho^*$.
- b. $\rho_n(x,t) = \rho_{\text{SiO}_2}$, independent of x and t , i.e. a uniform oxide.

Under these conditions the equations governing the tracer distributions are

$$\frac{\partial \rho_d^*}{\partial t} = \mathcal{D} \nabla^2 \rho_d^* - \frac{1}{\tau} (\rho_d^* - \frac{\rho_r \rho_r^*}{2K^2}) \quad (\text{D1})$$

$$\frac{\partial \rho_r^*}{\partial t} = \frac{1}{\tau} (\rho_d^* - \frac{\rho_r \rho_r^*}{K^2} + \frac{\rho_d \rho_n^*}{\rho_n}) \quad (\text{D2})$$

$$\frac{\partial \rho_n^*}{\partial t} = - \frac{1}{\tau} (\rho_d \frac{\rho_n^*}{\rho_n} - \frac{1}{2} \frac{\rho_r \rho_r^*}{K^2}) \quad (\text{D3})$$

$$\frac{\partial \rho_d}{\partial t} = \mathcal{D} \nabla^2 \rho_d - \frac{1}{\tau} (\rho_d - \frac{\rho_r^2}{K^2}) \quad (\text{D4})$$

$$\frac{\partial \rho_r}{\partial t} = \frac{2}{\tau} \left(\rho_d - \frac{\rho_r^2}{\kappa_2} \right). \quad (D5)$$

The first term in equations (D1) and (D4) describes the transport of dissolved molecular water; the quantity $\nabla \rho_d$ is the flux of that species. The other terms in the equations describe the formation and disappearance of the various species through the processes of recombination and dissociation; terms involving products of concentrations describe binary collisions. The quantity τ can be thought of as the lifetime of a dissolved water molecule, analogously to the charge carrier lifetime which appears in the equations describing electron and hole diffusion in solids (1). It should be noted that the quantity measured by means of nuclear resonance profiling is the total ^{18}O concentration, i.e. $\rho_{tot}^* = (\rho_d^* + \rho_r^* + \rho_n^*)$.

The problem of solving the full set of equations will not be addressed here. Instead, some approximations will be made which allow great simplification. The validity of the approximation may of course be questioned. First of all, it can be seen that by adding equations (D1) through (D3) we get

$$\frac{\partial \rho_{tot}^*}{\partial t} = D \nabla^2 \rho_d^*.$$

With the approximation

$$\frac{\rho_d^*}{\rho_d} \approx \frac{\rho_{tot}^*}{\rho_{tot}}$$

is made, then ρ_{tot}^* can be found by finding solutions to equations (D4) and (D5), which thus decouple from the first three.

These latter equations can be seen to revert to the equations generally taken to describe water permeation, which assume both that $\rho_r \gg \rho_d$

that equilibrium is established quickly between ρ_r and ρ_d . Under those conditions adding equations (D4) and (D5) results in

$$\frac{\partial}{\partial t} (\rho_r + \rho_d) = D \nabla^2 \rho_d + \frac{1}{\tau} \left(\rho_d - \frac{\rho_r^2}{\kappa_2} \right).$$

Applying the inequality as well as the equilibrium condition given as equation (6) in the text, this reduces to

$$\frac{\partial}{\partial t} \rho_r = \frac{D}{\kappa_2} \nabla^2 \rho_r^2 \quad (D6)$$

D-1. N. W. Ashcroft and N. D. Mermin, Solid State Physics (Holt Rinehart, 1976)
p 603

which is the equation that both Doremus (2) and Wagner (3) have.

An interesting case occurs in the limit that τ is so large that the mean free path between water dissociations is large compared to the SiO_2 film thickness. Under those conditions ρ_r approaches its saturation value while ρ_r is still negligible. The buildup of ρ_r can then be described by setting $P_d = P_{\text{H}_2\text{O}}(\text{sat})$ in equation (D5). That equation then decouples from equation (D4) as well; its solution is

$$\rho_r(t) = \rho_{\text{OH}}(\text{sat}) \tanh \frac{2P_{\text{H}_2\text{O}}(\text{sat})}{\rho_{\text{OH}}(\text{sat})} \frac{t}{\tau}$$

independent of x .

Since the exchange of an individual ^{18}O between the network and dissolved molecular water depends on the recombination of OH , the value of tracer diffusivity D^* at any time is proportional to the value of ρ_r^2 at that time. Under these conditions, the apparent value of D^*t at any time is related to its limiting value (i.e. when equilibrium has been established by the equation

$$[D^*t]_{\text{apparent}} = D_\infty^* \frac{\int_0^t dt' \rho_r^2(t')}{\rho_{\text{OH}}^2(\text{sat})}.$$

This equation can be integrated to give

$$1 - \frac{[D^*t]_{\text{apparent}}}{D_\infty^* t} = \frac{\tau}{2tR} \tanh \frac{2t}{\tau} R, \quad \text{where } R = \frac{P_{\text{H}_2\text{O}}(\text{sat})}{\rho_{\text{OH}}(\text{sat})}.$$

It can be seen that the quantity $[D^*t]_{\text{apparent}}$ is small for short times; it reaches half its asymptotic value at $t = \frac{\tau}{R}$. Using equation (8) in the text, this time is approximately 900τ at 600°C . The actual value of τ at any temperature can be determined through measurement of the time behavior of $[D^*t]_{\text{apparent}}$.

D-2. R. H. Doremus, J Phys Chem 80, 1773 (1976)

D-3. C. Wagner, J Chem Phys 18, 1229 (1950)

Bibliography

1. A. S. Grove, *Physics and Technology of Semiconductor Devices* (Wiley, 1967)
2. R. J. Zeto, C. G. Thornton, E. Hryckowian and C. D. Bosco, *J Electrochem Soc* 122, 1411 (1975)
3. L. E. Katz and B. F. Howells, *J Electrochem Soc* 126, 1822 (1979)
4. H. Agajanian, *Sol St Tech* 19, 36 (1977)
5. S. Mayo and W. H. Evans, "Development of Hydrogen and Hydroxyl Contamination in Thin Silicon Dioxide Films," NBSIR 78-1558 (NBS, March 1979)
6. W. H. Zachariasen, *J Am Chem Soc* 54 3841 (1932)
7. L. Mozzi and B. E. Warren, *J Appl Cryst* 2, 164 (1969)
8. R. L. Doremus, *Glass Science* (Wiley, 1973)
9. G. H. Konnert and J. Karle, *Acta Cryst A* 29, 702 (1973)
10. H. Marten, *J Chem Phys* 56, 1905 (1972)
11. R. J. Leadbetter and M. W. Stringfellow, "Neutron Inelastic Scattering," *Proc Grenoble Conf* (IAEA, Vienna, 1972) p. 501
12. T. Nagasima, *Japan J Appl Phys* 9, 879 (1970)
13. B. Brauer, G. Boden, A. Balogh and A. Andreeff, *Appl Phys* 16, 231 (1978)
14. P. H. Gaskell, D. W. Johnson, *J Noncryst Sol* 20, 171 (1976)
15. F. Shackelford and J. S. Masaryk, *J Noncryst Sol* 30, 127 (1978)
16. B. Brodsky, D. Cubicciotti, *J Am Chem Soc* 73, 3497 (1951)
17. R. L. Doremus, *J Phys Chem* 80, 1773 (1976)
18. E. P. EerNisse, *J Appl Phys* 45, 167 (1974)
19. L. N. Knopp and R. Stickler, *Electrochem Technology* 5, 37 (1967)
20. W. Mayer, L. Eriksson and J. A. Davies, *Ion Implantation in Semiconductors* (Academic, 1970)
21. J. R. Gibbons, *Proc IEEE* 60, 1062 (1972)
22. L. Primak, *J Appl Phys* 43, 2745 (1972)
23. J. E. Shelby, *J Appl Phys* 50, 3702 (1979)
24. C. B. Norris and E. P. EerNisse, *J Appl Phys* 45, 3876 (1974)
25. E. P. EerNisse and C. B. Norris, *J Appl Phys* 45, 5196 (1974)

26. W. Kratschmer, "Effects of Heavy Ion Radiation on Quartz Glass," Proc. Int. Conf. on Nucl. Photography and Track Detectors (Bucharest 1972) quoted in Antonini (1978)
27. A. Monfret and J. Bernard, "Chemical and Electrical Behavior of Ion Implanted SiO₂ Films" in Proc. 2nd Int. Conf. Ion Implantation in Semiconductors, I. Ruge and J. Graul, eds. (Springer-Verlag, 1971)
28. V. Antonini, A. Manara and P. Lensi, "Ion Irradiation and Stored Energy in Vitreous Silica," in Pantelides (1978), p. 316
29. J. B. Bates, R. W. Hendricks and L. B. Shaffer, *J Chem Phys* 61, 4163 (1974)
30. C. R. Fritzche and W. Rothermund, *J Electrochem Soc* 119, 1243 (1972)
31. G. W. Arnold, "Thermoluminescence in Ion-Implanted SiO₂," in Chernow et al. (1977)
32. R. P. Donovan and M. Simons, *J Appl Phys* 43, 2897 (1972)
33. N. M. Johnson, W. C. Johnson and M. A. Lampert, *J Appl Phys* 46, 1216 (1975)
34. D. J. DiMaria, D. R. Young, W. R. Hunter and C. M. Serrano, *IBM J Res Devel*, 22, 289 (1978)
35. G. W. Arnold, *IEEE Trans Nucl Sci* NS-20, 220 (1973)
36. G. W. Arnold, "Vibrational and Electronic Spectroscopy of Ion-Implantation-Induced Defects in Fused Silica and Crystalline Quartz," in Pantelides, p. 278 (1978)
37. G. H. Sigel, Jr., B. D. Evans, R. J. Ginther, E. J. Friebel, D. L. Griscom and J. Babiskin, *NRL Memo Rpt No. 2934* (NRL, 1974)
38. D. K. Brice, *Radiation Eff (GB)* 6, 77 (1970)
39. K. B. Winterbon, Ion Implantation Range and Energy Depositions, Vol 2 (Plenum, 1975)
40. E. A. Irene and R. Ghez, *J Electrochem Soc* 124, 1757 (1977)
41. S. Wang, T. Russell and B. S. H. Royce "Annealing Studies of Al+ Implanted SiO₂ Thin Films," *PSSL 300874* (Princeton U., 1974)
42. G. H. Sigel, private communication (1979)
43. W. Primak, Compacted States of Vitreous Silica (Gordon and Breach, 1975)
44. F. Seitz, *Disc Faraday Soc.* 5, 271 (1949)
45. J. F. Shackelford and J. S. Masaryk, *J Noncryst Sol* 21, 55 (1976)
46. R. H. Doremus, in Reactivity of Solids, Mitchell, de Vries, Roberts and Cannon, Eds., (Wiley, 1969) p. 667
47. O. L. Anderson and D. A. Stuart, *J Am Ceram Soc* 37, 573 (1964)

48. M. E. Milberg, "Diffusion in Glass," in Fast Ion Transport in Solids, W. Van Gool ed. (North Holland 1973) p. 378
49. F. J. Norton, Nature 191, 701 (1961)
50. E. Rosencher, A. Straboni, S. Rigo and G. Amsel, Appl Phys Lett 34, 254 (1979)
51. R. Haul and G. Dumbgen, Z Electrochem 66, 636 (1962)
52. E. W. Sucov, J Am Ceram Soc 46, 14 (1963)
53. E. L. Williams, J Am Ceram Soc 48, 190 (1965)
54. J. Moulson and J. P. Roberts, Trans Faraday Soc 57, 1208 (1961)
55. J. F. Shackelford, R. L. Studt and R. M. Fuhrath, J Appl Phys 43, 1619 (1972)
56. B. E. Deal and A. S. Grove, J Appl Phys 36, 3770 (1965)
57. . Blanc, Appl Phys Lett 33, 424 (1978)
58. E. M. Fowkes and F. H. Kielscher, Electrochem Soc Abstract #182, Spring Meeting, Seattle (21 May 1978)
59. A. Lora-Tamayo, E. Dominguez, E. Lora-Tamayo and J. Llabres, Appl Phys 17, 79 (1978)
60. R. J. Maier, "A Study of SiO₂ Growth Mechanism," AFWL-TR-76-228 (US Air Force, Kirtland AFB, NM, 1977)
61. . Ghez and Y. J. Van der Meulen, J Electrochem Soc 119, 1100 (1972)
62. A. G. Revesz and R. J. Evans, J Phys Chem Solids, 30, 551 (1969)
63. M. A. Hopper, R. A. Clarke and L. Young, J Electrochem Soc 122, 1216 (1975)
64. . A. Irene, J Electrochem Soc 121, 1613 (1974)
65. . A. Irene and Y. J. Van der Meulen, J Electrochem Soc 123, 1384 (1976)
66. B. E. Deal, J Electrochem Soc 125, 576 (1978)
67. B. E. Deal, D. W. Hess, J. D. Plummer and C. P. Ho, J Electrochem Soc 125, 339 (1978)
68. . Ehara, K. Sakuma and K. Ohwada, J Electrochem Soc 126, 2249 (1979)
69. T. Nakayama and F. C. Collins, J Electrochem Soc 113, 706 (1966)
70. W. A. Pliskin, IBM J Res Dev 10, 198 (1966)
71. Y. Ota and S. R. Butler, J Electrochem Soc 121, 1107 (1974)
72. J. P. Thomas and A. Cachard, Material Characterization Using Ion Beams (Plenum, 1978)
73. J. W. Mayer and E. Rimini, Eds., Ion Beam Handbook for Materials Analysis (Academic, 1977)

74. O. Meyer, G. Linker and F. Kappeler, *Ion Beam Surface Layer Analysis* (Plenum, 1976)
75. W. K. Chu, J. W. Mayer, and M. A. Nicolet, Backscattering Spectrometry (Academic, 1978)
76. K. L. Dunning & H. L. Hughes, *IEEE Trans Nucl Sci.* NS-19, 6, 243 (1972)
77. G. Amsel, J. P. Nadai, E. D'Artemaire, D. David, E. Girard and J. Moulin, *Nucl. Inst Meth* 92, 481 (1971)
78. K. L. Dunning, G. K. Hubler, J. Comas, W. H. Lucke and H. L. Hughes, *Thin Solid Films* 19, 145 (1973)
79. G. Amsel, G. Beranger, B. deGelas and P. Lacombe, *J Appl Phys* 39, 2246 (1968)
80. J. E. Gass, H. H. Muller, H. Schmied, L. Jorissen and G. Ziffermayer, *Nucl Inst Meth* 106, 109 (1973)
81. J. L. Whitton, I. V. Mitchell and K. B. Winterbon, *Can J Phys* 49, 1225 (1971)
82. J. M. Calvert, D. J. Derry and D. G. Lees, *J Phys D: Appl Phys* 7, 940 (1974)
83. D. J. Neila, P. J. Wise and D. G. Barnes, *J Phys D: Appl Phys* 5, 2292 (1972)
84. S. Rigo, S. Maurel, and G. Amsel, *Electrochem Soc Abstract* #102, Spring Meeting, Seattle (21 May 1978)
85. E. Ligeon and A. Bontemps, *J. Radioanal Chem* 12, 335 (1972)
86. G. Amsel and D. Samuel, *Anal Chem* 39, 1689 (1967)
87. D. David, G. Amsel, P. Boisot and G. Beranger, *J Electrochem Soc* 122, 388 (1975)
88. G. Amsel, G. Beranger, B. deGelas and P. Lacombe, *J Appl Phys* 39, 2246 (1968)
89. R. A. Oilerhead, E. Almqvist and J. Keuhner, *J Appl Phys* 37, 2440 (1966)
90. A. Choudhury, D. W. Palmer, G. Amsel, H. Curien and P. Baruch, *Sol St Comm*, 3, 119 (1965)
91. A. Turos, L. Kielinski, A. Barcz and J. Olenski, *J Radioanal Chem* 16, 627 (1973)
92. R. C. Weast, Handbook of Chemistry and Physics, 55th ed (CRC Press, 1974) p. D-159
93. W. Primak, *J. Appl Phys* 43, 2745 (1972)
94. R. L. Meek, *J Am Ceram Soc* 56, 342 (1973)
95. H. A. Schaeffer and K. Muehlenbachs, *J Matls Sci* 13, 1146 (1978)
96. S. Rigo, T. Rochet and A. Straboni, "An 180 Study of the Oxygen Exchange in SiO_2 Films During Thermal Treatment in Water Vapor," Presentation, 1980 International Conference on the Physics of MOS Insulators, Raleigh, NC 17-20 June 1980.

Literature Cited In Appendices

Appendix A

- A-1. R. H. Doremus, Glass Science (Wiley, 1973), p. 128
- A-2. S. E. Deal and A. S. Grove, J Appl Phys 36, 3770 (1965)
- A-3. J. Moulson and J. P. Roberts, Trans Faraday Soc 57, 1208 (1961)
- A-4. J. F. Gibbons, W. S. Johnson and S. W. Mylroie, Projected Range Statistics, 2nd Edn (Academic, 1975)

Appendix B

- B-1. Bonderup and P. Hvelplund, Phys Rev A4, 562 (1971)
- B-2. V. Vavilov, Soviet Phys JETP 5, 749 (1957)
- B-3. J. W. Mayer and E. Rimini, Eds., Ion Beam Handbook for Materials Analysis (Academic, 1977) p 163
- B-4. M. Abramowitz and I. A. Stegun, Handbook of Mathematical Functions, 924 (US Government Printing Office, 1964)

Appendix C

- C-1. V. Vavilov, Soviet Phys JETP 5, 749 (1957)
- C-2. N. Bohr, Mat. Fys. Medd. Dan. Vid. Selsk 18 (8) (1948)
- C-3. L. Fano, Ann Rev Nucl Sci. 13, 1 (1963)
- C-4. A. S. Grove, Physics and Technology of Semiconductor Devices (Wiley, 1967)
- C-5. T. Bonderup and P. Hvelplund, Phys Rev A4, 562 (1971)
- C-6. M. Abramowitz and I. A. Stegun, Handbook of Mathematical Functions, 446 (US Government Printing Office, 1964)
- C-7. H. Bichsel and P. Saxon, Phys Rev A11, 1286 (1975)
- C-8. D. Paolin, private communication (1979)

Appendix D

- D-1. N. W. Ashcroft and N. D. Mermin, Solid State Physics (Holt Rinehart, 1976) p 603
- D-2. R. H. Doremus, J Phys Chem 80, 1773 (1976)
- D-3. C. Wagner, J Chem Phys 18, 1229 (1950)

DAT
ILM